Freie Universität Berlin

Collective Effects in Strong-Field Ionization of Dense Media

im Fachbereich Physik der Freien Universität Berlin
eingereichte Dissertation

zur Erlangung des akademischen Grades
eines Doktors der Naturwissenschaften (Dr. rer. nat.)

vorgelegt von

Martin Wilke

Berlin
Oktober 2016

Gutachter:

1. *Prof. Dr. Emad F. Aziz (Betreuer)*
2. *Prof. Dr. Dr. h.c. mult. Ludger Wöste*

Tag der Disputation: 28.03.2017

Meiner Tochter
Sophia Wilke

Contents

1. Introduction

A deep fundamental understanding of light–matter interaction represents an important issue in the development of spectroscopic methods to study the electronic and nuclear dynamics of gases, liquids, and solids. A rigorous description of this interaction requires the application of quantum-mechanical methods to account for the properties of the studied quantum systems interacting with the electromagnetic field. Such a description becomes a challenging task when the applied field is strong. While the quantum-mechanical perturbation theory enables to study various systems interacting with weak or moderate fields, this approximation fails for photon sources of high intensities. A non-perturbative description of the light–matter interaction is, thus, required. It has been a hot research topic during the past decades and is still in development nowadays.

The elementary process of strong-field interaction of isolated atoms and molecules has been widely studied before. The most accurate method to describe this process in theory is to solve the time-dependent Schrödinger equation (TDSE) or its relativistic variants. However, such an approach is computationally demanding even for small systems and, hence, can not be applied to large multi-body systems. Additionally, the interpretation of results from the TDSE calculations appears rather complex due to its very fundamental description where decoupling of specific interactions is barely possible. Thus, the development of models and approximations represents an attractive possibility to gain a deeper understanding of strong-field processes.

The pioneering step for such a generalized but approximate description of strong-field–matter interactions represents the seminal work of the Russian solid-state physicist L.V. Keldysh[1] in 1965. He described the interaction in the dipole, single-active-electron (SAE) approximation, lying in the basis of the so-called strong-field approximation (SFA). In the frame of the SFA, the active electron is considered to be unperturbed by the laser field and, thus, it interacts only with the inner atomic or molecular potentials. After the ionization process, the electron is considered as a free particle propagating in the presence of the external electromagnetic field and its interaction with the residual atomic or molecular core is disregarded due to the dominance of the strong-field interaction. While the original Keldysh' work was based on a simple ansatz, the so-called Keldysh ansatz (KA), a more strict derivation of his analytical result was performed by Gribakin and Kuchiev[2] who applied the SFA to solve the TDSE for the case of above threshold detachment (ATD) in the long-wavelength limit. Independently two other approaches by Faisal[3] and Reiss[4] yielded similar results, which led to the alternative nomination of

the KA or the SFA as the Keldysh-Faisal-Reiss theory (KFR). However, till recently a controversy in the description of the external laser field accompanied this theory. Whereas a rigorous quantum-mechanical solution of the TDSE should be independent on the gauge used to describe the electromagnetic field, the SFA theories are inherently gauge variant. Reiss extended the theory to the relativistic regime by taking into account the higher orders of the multipole expansion and showed that the velocity (radiation) and not the length (Coulomb) gauge is the correct choice in the non-relativistic regime, especially for large photon energies and low numbers of absorbed photons in the multiphoton ionization process[5]. However, a number of publications[6, 7, 8, 9, 10] based on the experimental results by Kiyan and co-workers showed that the agreement of length gauge calculations is significantly better for both linearly and circularly polarized laser fields. Finally, comparison of the numerical solutions of the TDSE showed that the length gauge is (in contrast to the velocity gauge) in general able to reproduce the significant features of strong-field ionization[11]. This settles down the discussion on the choice of gauge. A number of review articles and books were published summarizing and discussing the strong-field interaction of atoms[12, 13, 14].

When the kinetic energy of the photoelectron is low, leading to a longer time that the outgoing electron spends in the vicinity of the parent core, its interaction with the residual atom or molecule needs to be considered. In this case the final-stage description in terms of the SFA is no longer valid, and the KA needs to be extended. This led to the recent development of new theories as the Coulomb-Volkov approximation (CVA) [15] and trajectory-based Coulomb-corrected strong-field approximation (TCSFA) [16]. These theories yielded a significant improvement in the description of above threshold ionization (ATI) of neutral atoms or positively charged ions, whereas ATD of negative ions is well described by the original SFA approach[7].

Models based on electron trajectory simulations represent another interesting and more enlightening approach to describe the ionization process. The trajectories are launched at time instances within the optical cycles of the field at which the ionization transition satisfies the saddle point condition that reflects the energy and momentum conservation rules in a quantum-mechanical representation (see Sec. 2.1.1). The initially developed semiclassical simple-man model (SMM) [17, 18] qualitatively describes many of the ionization features of the ATI and high-order ATI (HATI) processes in the low-frequency regime. However, the simulation of the ionization pathways in terms of the complex-time-and-space-based trajectories (allowing to include the sub-barrier movement during ionization) by the imaginary-time method (ITM) [19, 20] shows a significant improvement over the SMM in the high-frequency limit, whereas it also preserves the quantum features of the ionization process. The above-mentioned TCSFA represents such a method, where the Coulomb interaction are included to the ITM.

Apart from the ionization process, the interaction with laser fields can also result in high harmonic generation (HHG), which represents a competing channel of strong-field

interactions. In the HHG process, the active electron absorbs a number of photons and, instead of leaving the parent quantum system, it recombines with the residual ion during the laser pulse[21, 22]. Due to the inherent characteristics of emitted HHG light, this process plays an important role in the development of methods for ultrafast spectroscopy[23]. Moreover, the HHG process itself can be employed as direct spectroscopy with a sub-fs time resolution[24]. However, the present work is focused on strong-field ionization processes.

The above-mentioned methods were successfully applied to describe the ionization process in a strong laser field of single atoms and the SAE approximation is found to be sufficient to reproduce experimental results. However, the problem becomes already rather complicated in the case of molecules where the inclusion of more than one atom yields essential differences in the quantum-mechanical description of ATI [25] and HATI [26, 27, 28]. In the case of HATI, the presence of the molecular potential landscape leads to a breakdown of theories describing the angle-resolved electron emission. A simple consideration of a coherent superposition of single atoms ionized by strong fields is not sufficient to describe the molecular ATI emission[29, 30, 31]. Thus, there is a large uncertainty in the description of strong-field ionization of large quantum systems on the basis of quantum-mechanical consideration, which is especially a problem in the case of large molecules and clusters.

As an alternative approach to describe strong-field ionization of clusters, a number of semi-empirical and semiclassical models[32, 33, 34, 35] were developed by considering additional ionization channels as inner and outer ionization, the plasma formation and resonances, and the Coulomb explosion of irradiated clusters. A large complexity of experimental studies on strong-field–cluster interaction arises from the coupling of the nuclear and the electronic motion within the laser pulse duration due to the strong absorption and, thus, energy excess within the cluster yielding a strong nuclear response[36]. One possible consequence of the nuclear response represents the sudden matching of laser and plasma frequency during the Coulomb expansion, yielding a significant production of hot electrons with kinetic energies surpassing non-resonant ionization[37]. However, the development of modern few-cycle laser systems aims to reduce such coupling, which would enable to study the electron and nuclear response separately. Analogously to molecular ATI, the collective ionization of a cluster can not be explained by coherent superposition of ATI emission from a number of single atoms[38]. Therefore, collective ionization plays an important role in the strong-field–cluster interaction. Additional to the coupling of electron and nuclear motion, the geometry of the cluster and its interface to the vacuum influences the final emission[26, 39, 40]. These geometric effects are even more important for strong-field ionization from a solid surface[41].

The role of collective effects in strong-field ionization of dense media represents a general interesting question of fundamental importance. Clusters represent a particular case of dense media, where a large number of atomic or molecular particles is confined

within the cluster size. Therefore, the above-mentioned semi-empirical and semiclassical models are specific for the description of strong-field–cluster ionization. In the case of unconfined dense media, different approaches need to be developed to gain a deeper understanding of the transition from the single-atom ATI and HATI to collective ionization effects. One of such approaches was developed in the theoretical studies by Milošević and Čerkić, who applied full quantum-mechanical calculations as well as implemented semiclassical models to reveal for the first time the discrepancies as compared to single-atom ionization[42, 43, 44]. In these studies a significant enhancement of the strong-field ionization and high-harmonic generation yield in dense uniform media was predicted. Moreover, the fundamental laws for high-energy cut-off values were shown to be violated, and the extension to much higher kinetic energies (strong-field ionization) and shorter wavelength (high harmonic generation) was predicted.

Experimental access to the electron emission due to collective strong-field ionization of uniform dense media (gases) is rather sophisticated, since it requires the application of sufficiently large target densities and simultaneously maintenance of ultra-high vacuum conditions needed for photoelectron spectroscopy experiments. So far, mostly indirect studies of collective strong-field ionization were performed, such as the detection of photon emission by exciton recombination in liquid xenon[45] and the observations of transient absorption changes and detection of plasma fluorescence in liquid water[46, 47, 48]. Direct access to the electron emission affected by collective effects when applying ultrashort pulses, yielded rather insignificant results due the rather low target (gas) density[49]. Studies on water droplets and liquid microjets enabling ion[50, 51], photoelectron[52, 53], and high-harmonic spectroscopy[54, 55] showed fingerprints of liquid targets forming a plasma after illumination by a strong laser field, similar to the case of clusters.

Summarizing, the recent theoretical and experimental studies do not provide a complete and systematic description of the transition from single-atom ionization to collective ionization. Therefore, a general consideration of collective strong-field ionization needs to be developed. This issue represents the main subject of this work. To provide the insight to the role of collective effects, in this thesis an experiment enabling distinct measurements of non-collective and collective ionization yields as a function of the medium (gas) density was designed (see Sec. 3.3.4), the interface between diluted and dense targets was analyzed (see Sec. 5.2 and Sec. 5.4), and a generalized theory for strong-field ionization of diluted and dense systems was developed (see Sec. 5.3 and Sec. 5.5). After studying the diluted and dense target interface, where the collective ionization effects perturb the total emission, the transition from dense to condensed targets was examined, revealing the dominance of collective effects in the total ionization yield (see Sec. 6).

Additional to the main work on collective ionization a side project comprising the development of methods for evaluation of experimental results obtained by ultrafast photoelectron spectroscopy was realized. Its results are briefly discussed in Sec. 7.

2. Theoretical Description of Ionization Processes in a Laser Field

This chapter introduces the quantum-mechanical and semiclassical description of light-matter interactions. The character of such interactions can change significantly depending on the intensity of the applied external (laser) field. The laser-atom interaction can be estimated by the average energy, E, of an electron accelerated by an outer field with strength, F, or intensity, I, and with mean distance $\langle r \rangle$ to the atomic core of $1\,a_0$ (Bohr radius):

$$E = eF\langle r \rangle \tag{2.1}$$
$$\approx eFa_0 \tag{2.2}$$
$$= E_{\mathrm{H}}\sqrt{\frac{I}{I_{\mathrm{A}}}} \tag{2.3}$$

where e and m_{e} represent the charge and mass of an electron, respectively, $E_{\mathrm{H}} = \hbar^2 m_{\mathrm{e}}^{-1} a_0^{-2}$ is the Hartree energy and I_{A} represents the intensity corresponding to a field with the same strength, F_{A}, as the Coulomb field within the hydrogen atom:

$$I_{\mathrm{A}} = \frac{c}{8\pi}F_{\mathrm{A}} \tag{2.4}$$
$$= \frac{ce}{8\pi a_0^2} \quad . \tag{2.5}$$

If the energy E is comparable to or larger than the binding energy of the electron, the outer field is considered strong, leading to the weak-field condition:

$$I \ll I_{\mathrm{A}}$$
$$F \ll F_{\mathrm{A}} \tag{2.6}$$

Given above-mentioned relations, it is obvious that a change of the unit system from SI units to atomic units is convenient to describe the atom-laser interactions and, thus, atomic units will be used throughout this work if not specified otherwise.

In Sec. 2.1 ionization of an atom or ion in a strong laser field, where the weak-field condition is violated, will be discussed. This interaction requires a non-perturbative approach to describe the quantum-mechanical properties of the regarded system. Discussion of the results presented in Sec. 5 and Sec. 6 are based on this non-perturbative description.

Sec. 2.2 briefly summarizes ionization in weak laser fields. Weak-field ionization plays an important role in the single-photon ionization employed in photoelectron spectroscopy and, thus, represents the basis of Sec. 6.3.2 and Sec. 7.

In Sec. 2.3 scattering of electrons on potentials with and without application of outer fields is considered. Such effects become dominant in interactions of light with dense media but were only scarcely examined so far. To provide a deeper comprehension of these interactions in combination with ionization of a strong laser field represent the main goal of this work.

2.1. Theories based on strong-field aproximation

2.1.1. Above threshold detachment and ionization

2.1.1.1. The Keldysh Ansatz

The time-dependent Schrödinger equation (TDSE) of a quantum system interacting with a strong-field can be represented in the following form:

$$i\frac{\partial|\boldsymbol{\Psi}(t)\rangle}{\partial t} = \left(\hat{H}_{\mathrm{A}} + \hat{V}_{\mathrm{int}}\right)|\boldsymbol{\Psi}(t)\rangle \tag{2.7}$$

where $\hat{H}_{\mathrm{A}}$ represents the field-free electron Hamiltonian and $\hat{V}_{\mathrm{int}}$ is the time-dependent superimposed potential due the strong laser pulse. In general the interaction term $\hat{V}_{\mathrm{int}}$ is not weak to be treated in a perturbative way. $|\boldsymbol{\Psi}(t)\rangle$ can be expressed in terms of the eigenstates $|\boldsymbol{\psi}_i(t)\rangle$ of the total Hamiltonian $\hat{H}_{\mathrm{A}} + \hat{V}_{\mathrm{int}}$

$$|\boldsymbol{\Psi}(t)\rangle = |\boldsymbol{\psi}_0(t)\rangle + \sum_{\boldsymbol{p}} \alpha_{\boldsymbol{p}}(t)\,|\boldsymbol{\psi}_{\boldsymbol{p}}(t)\rangle \tag{2.8}$$

where $|\boldsymbol{\psi}_0(t)\rangle$ denotes the initial bound state, $|\boldsymbol{\psi}_{\boldsymbol{p}}(t)\rangle$ are ionized states and $\alpha_i(t)$ represents the population of each eigenstate. The initial state is considered to be undisturbed by the interaction potential. Undisturbed eigenstates fulfill the stationary Schrödinger equation $\hat{H}_{\mathrm{A}}\,|\boldsymbol{\phi}_0\rangle = E\,|\boldsymbol{\phi}_0\rangle$ and, thus:

$$|\boldsymbol{\psi}_0(t)\rangle = \exp\left(-iE_0t\right)|\boldsymbol{\phi}_0\rangle \tag{2.9}$$

The initial condition, $\lim_{t\to-\infty}\alpha_i(t) = \delta_{i,0}$, means that the initial wave function is disturbed adiabatically by the interaction potential $\hat{V}_{\mathrm{int}}$ for $t > -\infty$. The transition rate from $|\boldsymbol{\psi}_0(t)\rangle$ to $|\boldsymbol{\psi}_{\boldsymbol{p}}(t)\rangle$ is given by $\mathrm{d}|\alpha_{\boldsymbol{p}}(t)|^2/\mathrm{d}t$. Substituting Eq. (2.8) into the TDSE

yields:

$$0 = -i\frac{\partial|\mathbf{\Psi}(t)\rangle}{\partial t} + \left(\hat{H}_\mathrm{A} + \hat{V}_\mathrm{int}\right)|\mathbf{\Psi}(t)\rangle \tag{2.10}$$

$$= -i\left(\frac{\partial|\boldsymbol{\psi}_0(t)\rangle}{\partial t} + \sum_{\boldsymbol{p}}\alpha_{\boldsymbol{p}}(t)\frac{\partial|\boldsymbol{\psi}_{\boldsymbol{p}}(t)\rangle}{\partial t} + \sum_{\boldsymbol{p}}\frac{\mathrm{d}\alpha_{\boldsymbol{p}}(t)}{\mathrm{d}t}|\boldsymbol{\psi}_{\boldsymbol{p}}(t)\rangle\right)$$
$$+ \left(\hat{H}_\mathrm{A} + \hat{V}_\mathrm{int}\right)\left(|\boldsymbol{\psi}_0(t)\rangle + \sum_{\boldsymbol{p}}\alpha_{\boldsymbol{p}}(t)|\boldsymbol{\psi}_{\boldsymbol{p}}(t)\rangle\right) \tag{2.11}$$

$$= \hat{V}_\mathrm{int}|\boldsymbol{\psi}_0(t)\rangle - i\sum_{\boldsymbol{p}}\frac{\mathrm{d}\alpha_{\boldsymbol{p}}(t)}{\mathrm{d}t}|\boldsymbol{\psi}_{\boldsymbol{p}}(t)\rangle \tag{2.12}$$

Using the orthonormality ($\langle\boldsymbol{\psi}_{\boldsymbol{p}}(t)|\,|\boldsymbol{\psi}_{\boldsymbol{p}'(t)}(t)\rangle] = \delta_{\boldsymbol{p},\boldsymbol{p}'(t)}$) of the $\boldsymbol{p}$-states, the projection of Eq. (2.12) on $\langle\boldsymbol{\psi}_{\boldsymbol{p}}(t)|$ leads to the system of differential equations:

$$\frac{\mathrm{d}\alpha_{\boldsymbol{p}}(t)}{\mathrm{d}t} = -i\langle\boldsymbol{\psi}_{\boldsymbol{p}}(t)|\,\hat{V}_\mathrm{int}|\boldsymbol{\psi}_0(t)\rangle \tag{2.13}$$

A reasonable approach to solve these equations is to assume a periodic behavior of $\hat{V}_\mathrm{int}$, implying a continuous wave (cw) condition:

$$\hat{V}_\mathrm{int}[t] = \hat{V}_\mathrm{int}[t+\tau] \tag{2.14}$$

The periodicity of $\hat{V}_\mathrm{int}$ allows to apply the Floquet theorem: Each eigenstate $|\boldsymbol{\psi}(t)\rangle$ can be represented by a periodic quasienergy wave function of the form $|\boldsymbol{\xi}_i(t)\rangle = |\boldsymbol{\psi}_i(t)\rangle\exp(-iE_it)$ with quasienergy E_i satisfying the periodic Schrödinger equation

$$i\frac{\partial|\boldsymbol{\xi}_i(t)\rangle}{\partial t} = \left(\hat{H}_\mathrm{A} + \hat{V}_\mathrm{int} - E_i\right)|\boldsymbol{\xi}_i(t)\rangle\ . \tag{2.15}$$

Eq. (2.13) can, thus, be represented as

$$\frac{\mathrm{d}\alpha_{\boldsymbol{p}}(t)}{\mathrm{d}t} = -i\exp\left(i(E_{\boldsymbol{p}} - E_0)t\right)\langle\boldsymbol{\xi}_{\boldsymbol{p}}(t)|\,\hat{V}_\mathrm{int}|\boldsymbol{\xi}_0(t)\rangle \tag{2.16}$$

$$= -i\sum_n \exp\left(i(E_{\boldsymbol{p}} - E_0 - n\omega)t\right)A_{\boldsymbol{p},n} \tag{2.17}$$

where the matrix element $\langle\boldsymbol{\xi}_{\boldsymbol{p}}(t)|\,\hat{V}_\mathrm{int}|\boldsymbol{\xi}_0(t)\rangle$ includes the time-independent Fourier transform $A_{\boldsymbol{p},n}$ with

$$A_{\boldsymbol{p},n} = \frac{1}{\tau}\int_0^\tau \mathrm{d}t\langle\boldsymbol{\xi}_{\boldsymbol{p}}(t)|\,\hat{V}_\mathrm{int}|\boldsymbol{\xi}_0(t)\rangle\exp(in\omega t) \tag{2.18}$$

Eq. (2.17) needs to be integrated from $-\infty$ to t. To avoid a singularity when $(E_{\boldsymbol{p}} - E_0 - n\omega) \neq 0$, an infinitesimal small real value ηt is introduced to the argument of

the exponential function in Eq. (2.17), yielding:

$$\alpha_{\boldsymbol{p}}(t) = -\lim_{\eta\to 0}\sum_n \frac{\exp\left(i(E_{\boldsymbol{p}} - E_0 - n\omega - i\eta)t\right)}{E_{\boldsymbol{p}} - E_0 - n\omega - i\eta} A_{\boldsymbol{p},n} \tag{2.19}$$

The population probability $|\alpha_{\boldsymbol{p}}(t)|^2$ is, thus:

$$|\alpha_{\boldsymbol{p}}(t)|^2 = \lim_{\eta\to 0}\left(\sum_n \frac{\exp\left(2\eta t\right)}{\left(E_{\boldsymbol{p}} - E_0 - n\omega\right)^2 + \eta^2}|A_{\boldsymbol{p},n}|^2 + \sum_{\substack{n,m\\ n\neq m}} \frac{\exp\left(i(m-n)\omega t + 2\eta t\right)}{(E_{\boldsymbol{p}} - E_0 - n\omega - i\eta)(E_{\boldsymbol{p}} - E_0 - m\omega + i\eta)} A_{\boldsymbol{p},n}A^*_{\boldsymbol{p},m}\right) \tag{2.20}$$

where the second term is oscillating with the fundamental frequency ω and its harmonics and, thus, yields no contribution to the time-averaged population $\langle|\alpha_{\boldsymbol{p}}(t)|^2\rangle_t$. As a result, we have

$$\langle|\alpha_{\boldsymbol{p}}(t)|^2\rangle_t = \lim_{\eta\to 0}\sum_n \frac{\exp\left(2\eta t\right)}{\left(E_{\boldsymbol{p}} - E_0 - n\omega\right)^2 + \eta^2}|A_{\boldsymbol{p},n}|^2 \tag{2.21}$$

Accordingly, the transition rate $\Gamma_{0\to\boldsymbol{p}}$ is given as the time-derivative

$$\Gamma_{0\to\boldsymbol{p}} = \frac{\mathrm{d}\langle|\alpha_{\boldsymbol{p}}(t)|^2\rangle_t}{\mathrm{d}t} \tag{2.22}$$

$$= \lim_{\eta\to 0}\sum_n \frac{2\eta\exp\left(\eta t\right)}{\left(E_{\boldsymbol{p}} - E_0 - n\omega\right)^2 + \eta^2}|A_{\boldsymbol{p},n}|^2 \tag{2.23}$$

$$= 2\pi\lim_{\eta\to 0}\sum_n \exp\left(2\eta t\right)|A_{\boldsymbol{p},n}|^2\delta(E_{\boldsymbol{p}} - E_0 - n\omega) \tag{2.24}$$

$$= 2\pi\sum_n |A_{\boldsymbol{p},n}|^2\,\delta\left(E_{\boldsymbol{p}} - E_0 - n\omega\right) \tag{2.25}$$

where $\pi^{-1}2\eta(x^2+\eta^2)^{-1} = \delta(x)$ is a nascent representation of the delta-function at $\eta\to 0$. Due to the energy conservation implied by the delta-function, the matrix element $A_{\boldsymbol{p},n}$ can as well be given in terms of the original Hamiltonian eigenstates $|\boldsymbol{\psi}_i(t)\rangle$:

$$A_{\boldsymbol{p},n} = \frac{1}{\tau}\int_0^\tau \mathrm{d}t\langle\boldsymbol{\psi}_{\boldsymbol{p}}(t)|\,\hat{V}_{\mathrm{int}}\,|\boldsymbol{\psi}_0(t)\rangle \tag{2.26}$$

It is remarkable that Eq. (2.25) predicts a discrete spectrum of final states $\boldsymbol{p}$ with equidistant energies. These so-called ATI peaks are therefore a result of the periodic interaction and not a property of a quantization of light in the form of photons. Consequently a break-down of the ATI peak structure is expected in the short pulse regime[58]. A sequence of ATI peaks is depicted in Fig. 2.1.

According to the Keldysh ansatz (KA), the transition probability $A_{\boldsymbol{p},n}$ can be approxi-

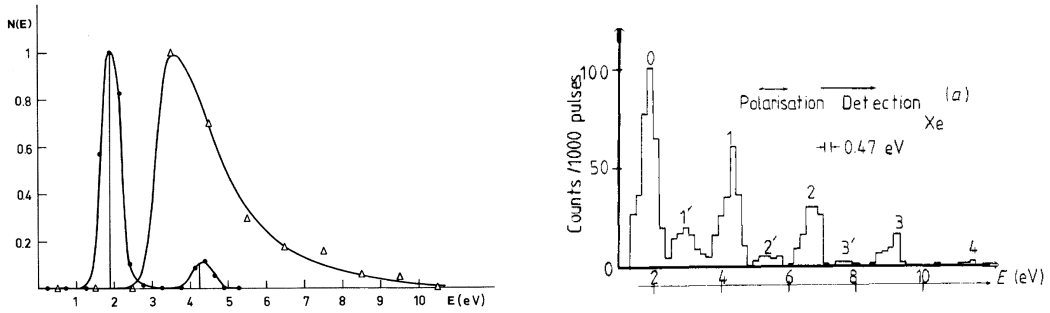

Figure 2.1.: ATI peak structure due to the ionization of Xe. Left: First ATI peaks recorded for a photon energy of 2.34 eV(circles) and broad ATI emission for 1.17 eV(triangles) at intensities of $8 \times 10^{12}\,\mathrm{W\,cm^{-2}}$ and $4 \times 10^{13}\,\mathrm{W\,cm^{-2}}$, respectively.Reprinted figure with permission from [Agostini et al.[56], Physical Review Letters, 42, 1127 (1797)] Copyright (1979) by the American Physical Society. Right[57]: Multi-peak structure above the ionization threshold up to the fourth order with photon energy of 2.34 eV and intensities up to $1 \times 10^{11}\,\mathrm{W\,cm^{-2}}$. Peaks of different total angular momentum in the initial state are marked by primes.

mated by

$$A_{\boldsymbol{p},n} \approx \int_{-\infty}^{\infty} \mathrm{d}t \langle \boldsymbol{\Psi}_{\boldsymbol{p}}(t)| \hat{V}_{\mathrm{int}} |\boldsymbol{\psi}_0(t)\rangle \tag{2.27}$$

where $\boldsymbol{\Psi}_{\boldsymbol{p}}(t)$ is the Volkov function[59] of a quasi-free electron with momentum $\boldsymbol{p}$(t), and $|\boldsymbol{\psi}_0(t)\rangle$ describes the initial unperturbed bound state wave function with binding energy (ionization potential) E_{B}. The Volkov wave function is the solution of the Hamiltonian of a charged particle in an intense laser field and is considered here in the non-relativistic limit and in the length gauge. Thus, this strong field approach - also refererred as strong-field approximation (SFA) - describes the ionization process by making use of two approximations: the initial state of the active electron is considered to be unperturbed by the laser field and, thus, is described by the original atomic/molecular wave functions; in the final state the electron is considered to propagate in the laser field and not affected by the parent atomic potential. Obviously the accuracy of the KA relies on neglecting of the interaction of bound electrons with the laser field prior to the ionization transition, neglecting of the perturbation of the quasi-free electron Hamiltonian by the parent potential (e.g. the Coulomb interaction) in the final state, and electron correlations. The parent potential after the ionization process, thus, has to be of short-range character.

The Keldysh theory is inherently not gauge-invariant (neither the Volkov function nor the interaction potential $\hat{V}_{\mathrm{int}}$, the only exception is the case of ionization from a zero-range potential[2]) which led to a discussion on the choice of gauge for the description of photoemission spectra. As the Hamiltonian is gauge invariant, the KA was developed further to overcome this obstacle. However, to the present day no satisfactory solution was found[60]. In the mean-time, several studies[7, 61, 2, 11] were performed favoring

the length gauge as used in the original KA and, thus, discarding the velocity-gauge[62] for a larger range of applications.

We consider here the laser field to be monochromatic and linearly polarized, satisfying the periodic boundary condition in Eq. (2.14):

$$\boldsymbol{F}(t) = -\dot{\boldsymbol{A}}(t) \tag{2.28}$$

$$= eF\cos\omega t\hat{\boldsymbol{\epsilon}_{\mathrm{L}}} \tag{2.29}$$

where F_0 represents the strength amplitude of the laser field of frequency ω (period $\tau = 2\pi\omega^{-1}$) and polarization $\hat{\boldsymbol{\epsilon}_{\mathrm{L}}}$.

The Volkov function in the length gauge has the form:

$$\boldsymbol{\Psi}_{\boldsymbol{p}}(t) = \exp\left(i\boldsymbol{v}(t)\cdot\boldsymbol{r}(t) - \frac{i}{2}\int_{-\infty}^{t}\mathrm{d}t'\boldsymbol{v}^2(t')\right) \tag{2.30}$$

with

$$\dot{\boldsymbol{r}}(t) = \boldsymbol{v}(t) = \boldsymbol{p}(t) + \int_{-\infty}^{t}\mathrm{d}t'\boldsymbol{F}(t') \tag{2.31}$$

$$= \boldsymbol{p}(t) - e\boldsymbol{A}(t) \tag{2.32}$$

and quasienergy

$$E_{\boldsymbol{p}(t)} = \frac{\boldsymbol{p}(t)^2}{2} + \mathrm{U_P} \quad , \tag{2.33}$$

where $\mathrm{U_P} = F^2(2\omega)^{-2}$ denotes the quiver energy due to the time-dependent linearly polarized electric field and the integrals in Eq. (2.30) and Eq. (2.31) are calculated adiabatically in the limit $t \to \infty$ due to the oscillatory behavior of the integrands. The interaction potential in the dipole approximation reads:

$$\hat{V}_{\mathrm{int}} = -q\boldsymbol{r}(t)\cdot\boldsymbol{F}(t)\,. \tag{2.34}$$

Substituting Eq. (2.30) into Eq. (2.27) yields the amplitude[2]

$$A_{\boldsymbol{p},n} = \frac{1}{\tau}\int_0^{\tau}\mathrm{d}t\left(E_0 - \frac{\boldsymbol{v}(t)^2}{2}\right)\widetilde{\boldsymbol{\Phi}}_0(t)\exp\left(\frac{i}{2}\int_0^{\tau}\mathrm{d}t'\boldsymbol{v}^2(t) - iE_0t\right) \tag{2.35}$$

with

$$\widetilde{\boldsymbol{\Phi}}_0(t) = \int\mathrm{d}\boldsymbol{r}(t)\boldsymbol{\Phi}_0(t)\exp\left(-i\boldsymbol{v}(t)\cdot\boldsymbol{r}(t)\right) \quad , \tag{2.36}$$

where $\boldsymbol{\Phi}_0$(t) represents the non-correlated single-electron wave function obtained from factorization of the N-electron total wave function in the asymptotic limit $r \gg 1$ into the $(N-1)$-electron wave function of the residual core and $\boldsymbol{\Phi}_0$(t):

$$|\boldsymbol{\Psi}_{1,\ldots,N-1,N}(t)\rangle \approx |\boldsymbol{\Psi}_{1,\ldots,N-1}(t)\rangle\,|\boldsymbol{\Phi}_0(t)\rangle \tag{2.37}$$

This approximation, however, implies that the ionization transition occurs at a large distance from the core. This condition requires that if the Keldysh adiabaticity parameter $\gamma = \sqrt{E_0(2\mathrm{U_P})^{-1}} = \omega\kappa F^{-1}$ is small (i.e. in the strong-field regime, also called tunneling regime) the laser field F needs to be considerably weaker than the atomic field F_A [2].

2.1.1.2. Saddle-point method

The exponential part in the second term of Eq. (2.35) can be interpreted as action $S_0(t)$ with

$$S_0(t) = \frac{1}{2}\int_{-\infty}^{t} \mathrm{d}t' \boldsymbol{v}^2(t) - iE_0 t\,. \tag{2.38}$$

As $\exp(iS(t))$ represents a fast oscillating function, the method of steepest descent, or saddle-point method, for multiple non-degenerate saddle points can be applied. However, this method is limited to the adiabatic condition $\omega \ll E_0$. The saddle points are given by:

$$\frac{\partial S_0(t_s)}{\partial t} = 0 \tag{2.39}$$

$$\boldsymbol{v}^2(t_s) - 2E_0 = 0 \tag{2.40}$$

$$(\boldsymbol{p}(t_s) - e\boldsymbol{A}(t_s))^2 + \kappa^2 = 0 \tag{2.41}$$

where $\kappa = \sqrt{-2E_0}$. The saddle-points represent the energy conservation at the moment of transition from the initial bound state to the final quasi-free state, in good agreement with the adiabatic theory[2]. The complex ionization time t_s can be retrieved from:

$$\left(\boldsymbol{p}(t) + \frac{eF}{\omega}\sin\omega t_s \hat{\boldsymbol{\epsilon}_\mathrm{L}}\right)^2 + \kappa^2 = 0 \tag{2.42}$$

where only complex solutions in the upper complex hemisphere ($\mathrm{Im}\, t_s > 0$) and within the first period ($0 \leq \mathrm{Re}\, t_s < 2\pi$) are considered. The saddle-point method allows to find simple energy conservation rules using the adiabatic theory and provide semiclassical insights into the quantum-mechanical ionization process.

The saddle points t_s are given by the quadratic equation of $\sin\omega t_s \equiv \alpha_\mu$

$$0 = \alpha_\mu^2 - 2q_0\cos\theta\alpha_\mu + q_0^2 - \gamma^2 \tag{2.43}$$

$$\alpha_\mu = q_0\cos\theta \pm i\sqrt{q_0^2\sin^2\theta + \gamma^2} \quad , \tag{2.44}$$

where

$$q_0 = -\frac{p\omega}{eF} = -\frac{1}{e}\sqrt{\frac{T}{2\mathrm{U_P}}} \quad , \tag{2.45}$$

resulting in two saddle points given by

$$t_\mu = \frac{1}{2\omega}\arccos\sqrt{\left(q_0^2+\gamma^2-1\right)^2+4\left(\gamma^2+q_0^2\sin^2\theta\right)}-q_0^2-\gamma^2 \tag{2.46}$$

$$\tau_\mu = \frac{1}{2\omega}\operatorname{arccosh}\sqrt{\left(q_0^2+\gamma^2-1\right)^2+4\left(\gamma^2+q_0^2\sin^2\theta\right)}+q_0^2+\gamma^2 \tag{2.47}$$

$$t_s = \left(t_\mu-\frac{\pi}{2}\right)\mu+\frac{\pi}{2}+i\tau_\mu \quad \text{with } \mu=\pm 1 \tag{2.48}$$

In the tunneling limit ($\gamma \ll 1$), the imaginary part of the saddle point can be considered as tunneling time (also known as *Keldysh tunneling time*) of the electron through the potential barrier composed by a superposition of the external and atomic fields. The value of a finite tunneling time was intensively discussed[63, 64, 65] within the last decades and recently experimentally investigated, driven by the development of attoscience[66, 67, 68].

While the KA provides sufficient details to describe the ionization process, a number of additional effects need to be considered to correctly describe the ATI emission. These will be discussed in Sec. 2.1.1.5.1 – Sec. 2.1.1.6

2.1.1.3. Detachment rate from a short-range potential

Using the above introduced SFA, which is a common name of Keldysh-like theories, the differential n-th photon detachment rate (see Eq. (2.35)) can be represented for a short-range atomic potential[2] as

$$\begin{aligned}\frac{\mathrm{d}w_n(p,\theta)}{\mathrm{d}\Omega} &= p\cdot B_{l,|m|}(\kappa,\omega)\\ &\times\left|P_l^{|m|}\left(\sqrt{1+\left(\frac{p}{\kappa}\right)^2\sin^2\theta}\right)\right|^2\\ &\times\left|\sum_\mu(-1)^{l+m}\frac{(\beta_\mu+i\alpha_\mu)^n}{\sqrt{2\pi(-iS''_\mu)^{\nu+1}}}\exp\left(-i\beta_\mu(4zq_0+\alpha_\mu)\right)\right|^2\end{aligned} \tag{2.49}$$

with

$$B_{l,|m|}(\kappa,\omega) = \frac{A^2}{4\pi}\left(\frac{\sqrt{2}\kappa}{\omega}\right)^{2\nu}\Gamma^2\left(1+\frac{\nu}{2}\right)(2l+1)\frac{(l-|m|)!}{(l-|m|)!} \tag{2.50}$$

and

$$\nu = \frac{Z}{\kappa} \tag{2.51}$$

$$z = \frac{\mathrm{U_P}}{\omega} \tag{2.52}$$

$$\beta_\mu = \cos\omega t_s = (-1)^\mu\sqrt{1-\alpha_\mu^2} \tag{2.53}$$

$$S''_\mu = 4z\beta_\mu(q_0+\alpha_\mu) \tag{2.54}$$

where $Z=0$ in the case of above threshold detachment (ATD) from a short-range potential, and $P_l^{|m|}$ is the associated Legendre polynomial. Note that the value $Z=1$

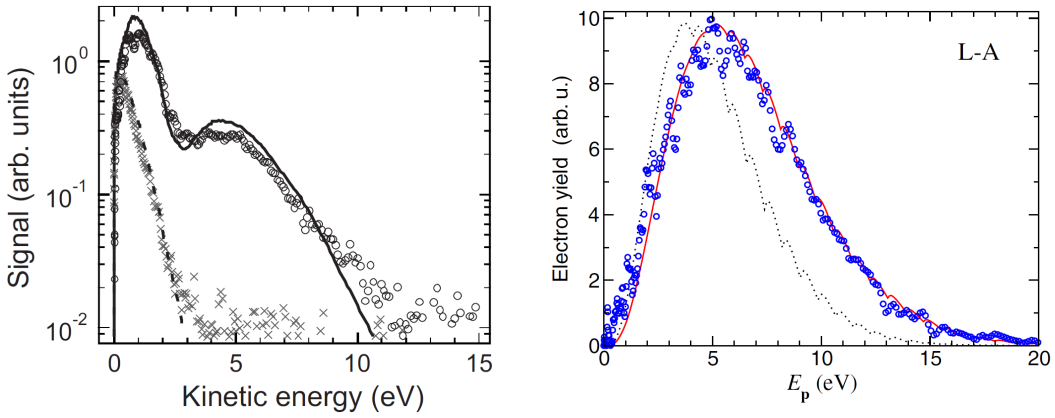

Figure 2.2.: Comparisons of the detachment of F^- in a strong laser field in experiment and calculations provided by the KA using the saddle point approximation as in Eq. (2.49). Left: Circles (crosses) represent experimental data in parallel (perpendicular) to the laser polarization axis. Solid and dashed lines represent respective theoretical calculations. Reprinted figure with permission from [Bergues et al.[7], Physical Review A, 75, 063415 (2007)] Copyright (2007) by the American Physical Society. Right: Blue dots represent data from Ref.[6] the red solid line the prediction of ATD with a central wavelength of 1510 nm and a peak intensity of $3.8 \times 10^{13}\,\mathrm{W\,cm^{-2}}$. Reprinted from "Gauge dependence of the strong-field approximation: Theory vs. experiment for photodetachment of F-"[69], 275, Gazibegović-Busuladžić et al., Optics Communications, 116, Copyright (2007), with permission from Elsevier.

should be used in the case of ATI [2]. Additionally, the measured photoelectron momentum is given by Eq. (2.33) and Eq. (2.25):

$$p = \sqrt{2\left(n\omega - \frac{\kappa^2}{2} - \mathrm{U_P}\right)}\,. \tag{2.55}$$

The general validity of the SFA approach has been proven in numerous publications[8, 58, 7, 69, 70]. Especially in the case of ATD, representing detachment from negative ions, the predictions appear precise. A comparison of theory and experiment can be found in Fig. 2.2. As the short-range potential is applicable to describe the interaction with a neutral core, the SFA describes well the ATD process but is inherently inaccurate for ATI and, thus, requires an extension towards inclusion of a long-range (Coulomb) potential in the final Volkov state. This approach, called Coulomb-Volkov approximation (CVA), will be discussed in Sec. 2.1.1.6.2.

The quasi-static ionization rate ($\omega \to 0$) integrated over all ionization channels (3D momentum space) can be written as:

$$w_n \propto \left(\frac{2F_\mathrm{A}}{F}\right)^{2\nu-|m|-1} \exp\left(-\frac{2F_\mathrm{A}}{3F}\right) \quad , \tag{2.56}$$

which is in agreement with the results obtained from a purely quantum-mechanical derivation[71].

2.1.1.4. semiclassical trajectories

The action $S_0(t)$ in Eq. (2.38) can as well be interpreted and evaluated in a semiclassical way. According to the classical mechanics the trajectory of a particle is described by

$$\boldsymbol{r}_\mu(t) = \frac{\partial S_0(t)}{\partial \boldsymbol{p}(t)} \tag{2.57}$$

$$= \int_{t_s}^{t} \mathrm{d}t' \boldsymbol{v}(t) \tag{2.58}$$

with the initial boundary conditions for the position and velocity regarding the ionization instant t_s and detection time t_D. The trajectories are calculated in the SFA and, thus, the atomic field in the first approximation ignored while the ionization process itself is only partially considered. The simplicity of this approach allows to easily extend the modeling to more complex systems where the quantum-mechanical approach via TDSE in general or in Keldysh-based theories by evaluating Eq. (2.27) is computationally too expensive. One can separate the real-time-based simple-man model (SMM) and complex-time based imaginary-time method (ITM). Both evaluate Eq. (2.57) but differ with regard to the initial conditions.

2.1.1.4.1. Simple-man model The SMM describes the electron classically oscillating in the laser field $\boldsymbol{F}$(t), in the tunneling limit ($\gamma \ll 1$), and disregards the Coulomb interaction between the parent core and the ionized electron. The electron trajectory can be described by[72, 18]:

$$\ddot{\boldsymbol{r}}(t) = e\boldsymbol{F}(t)\,, \quad \dot{\boldsymbol{r}}(t_\mu) = 0\,, \quad \boldsymbol{r}(t_\mu) = \boldsymbol{b} \tag{2.59}$$

where $\boldsymbol{b}$ describes the tunnel exit (i.e. the location of the electron after the tunnel ionization)[1]:

$$\boldsymbol{b} = -\frac{E_\mathrm{B}}{\|\boldsymbol{F}(t_\mu)\|^2}\boldsymbol{F}(t_\mu) = \frac{\kappa^2}{2F\cos\omega t_\mu}\hat{\boldsymbol{\epsilon}}_\mathrm{L} \tag{2.60}$$

yielding the trajectory

$$\boldsymbol{r}(t) = \left(\frac{eF\sin\omega t_\mu}{\omega}(t-t_\mu) - \frac{eF}{\omega^2}(\cos\omega t - \cos\omega t_\mu) - \frac{\kappa^2}{2F\cos\omega t_\mu}\right)\hat{\boldsymbol{\epsilon}}_\mathrm{L} \tag{2.61}$$

and kinetic energy $T = 1/2\,\langle \boldsymbol{p}(t)^2\rangle_t$:

$$T = \frac{1}{2\tau}\int_0^\tau \mathrm{d}t(\boldsymbol{v}(t) + e\boldsymbol{A}(t))^2 \tag{2.62}$$

$$= 2\mathrm{U_P}\cos^2\omega t_\mu \tag{2.63}$$

It is obvious that the kinetic energy is restricted to $0 \leq T \leq 2\mathrm{U_P}$, leading to a sharp high-energy cut-off in the electron kinetic energy spectrum. Its distribution can be calculated by integrating each trajectory weighted by the corresponding tunneling probability in the quasi-statical limit:

$$\frac{\mathrm{d}w(T,\theta)}{\mathrm{d}\Omega} = \int_0^{\tau} \mathrm{d}t_\mu \delta(T - 2\mathrm{U_P}\cos^2\omega t_\mu) \frac{4}{\|\boldsymbol{F}(t_\mu)\|} \exp\left(-\frac{2}{3\|\boldsymbol{F}(t_\mu)\|}\right) \tag{2.64}$$

$$= \int_0^{2\mathrm{U_P}} \mathrm{d}T' \delta(T - T') \frac{4}{\|\boldsymbol{F}(t(T'))\|} \exp\left(-\frac{2}{3\|\boldsymbol{F}(t(T'))\|}\right) \times \frac{\sqrt{2}\omega}{\pi\sqrt{T(\|\boldsymbol{F}(t(T'))\|^2 - 2T\omega^2}} \tag{2.65}$$

with

$$\boldsymbol{F}(t(T')) = F\sqrt{1 - \frac{2T\omega^2}{F^2}} \tag{2.66}$$

resulting in

$$\frac{\mathrm{d}w(T,\theta)}{\mathrm{d}\Omega} = \frac{2\sqrt{2}}{\pi\omega\sqrt{T}} \frac{\exp\left(-\frac{2^{-\frac{1}{3}}}{\omega}(2\mathrm{U_P} - T)^{-\frac{1}{3}}\right)}{T - 2\mathrm{U_P}} \tag{2.67}$$

The SMM in its simplest form allows to describe the strong-field ionization in the strict tunneling limit ($\gamma \ll 1$) where the electron kinetic energy after the tunneling event can be neglected and where the tunneling time is instantaneous as compared to the laser oscillation period. It predicts emission only along the laser polarization, with the energy cutoff value of $2\mathrm{U_P}$. This value also characterizes the extension of the energy distribution in the quantum-mechanical KA as the dimensionless momentum q_0 in Eq. (2.45) becomes one and yields, thus, saddle points on the unity circle $\exp(i\theta)$. However, $2\,\mathrm{U_P}$ is not a strict cut-off is in the KA. A comparison between SMM and the quantum-mechanical description of Sec. 2.1.1.2 for different values of γ can be found in Fig. 2.3.

To extend the SMM for larger values of γ, one needs to account for the initial conditions of the ionization process. This can be done by using approaches based on the complex-timed ITM consideration (which will be discussed in Sec. 2.1.1.4.2), where the initial

[1] In the most simple form of the SMM the exact tunnel exit can be chosen arbitrarily and is sometimes assumed to be 0[18] as it does not contribute to $\dot{\boldsymbol{r}}(t)$ and, thus, not to the final kinetic energy either. However, extension of the model towards including the Coulomb correction for ATI and rescattering for high-order above threshold ioniztation requires the correct value[72]. One can see that $\boldsymbol{b}$ is 0 in the strict tunneling regime for $\gamma \to 0$

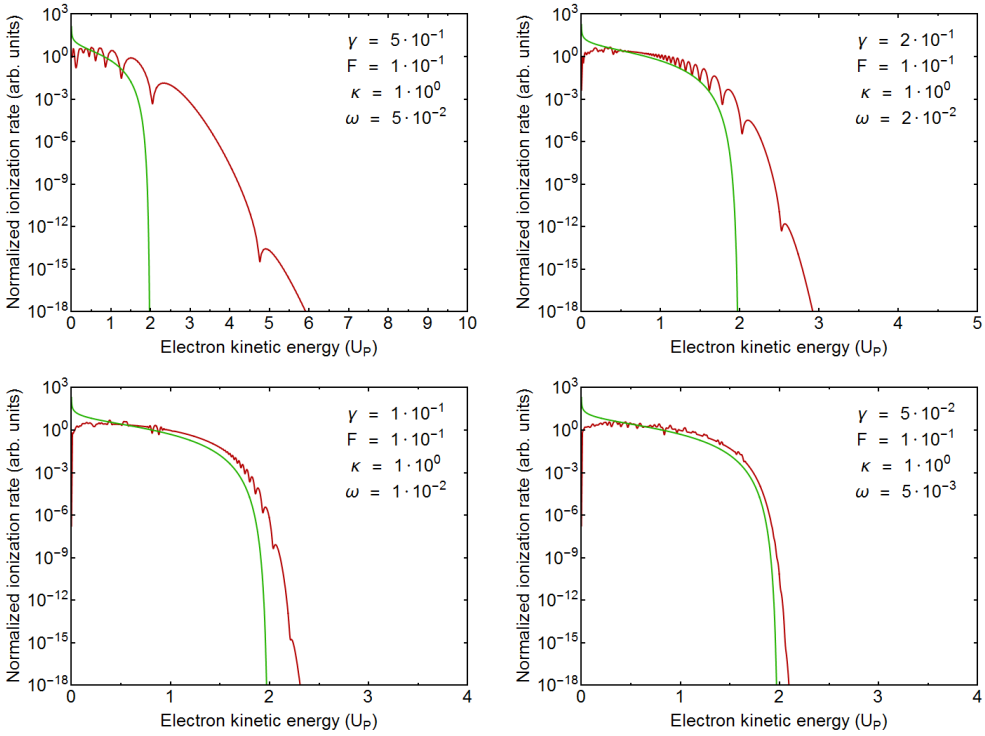

Figure 2.3.: Comparisons of the SMM (green) and the quantum-mechanical model (red) presented in Sec. 2.1.1.2 for different values of γ. The SMM yields quantitatively correct results in the limit of $\gamma \ll 1$. However, the SMM becomes less precise at larger γ, and deviates already at moderate values of $\gamma \simeq 0.1$. Quantum-mechanical properties as interference and the extension of kinetic energies above the cut-off of $2U_P$ are not observable in the classical approach.

conditions are given by[60]:

$$\dot{\boldsymbol{r}}(t_\mu) = v_\perp - \frac{F}{\omega}\cos\omega t_\mu(\cosh\omega\tau_\mu - 1) \tag{2.68}$$

$$\boldsymbol{r}(t_\mu) = -\frac{F}{\omega^2}\sin\omega t_\mu(\cosh\omega\tau_\mu - 1) \tag{2.69}$$

This means that the ionization in complex time undergoes a direct motion $(t_\mu, \tau_\mu) \rightarrow (t_\mu, 0)$ along the imaginary axis and, thus, the electron trajectory becomes real in real time at the given boundary condition for $\boldsymbol{r}(t_\mu\ )$.

2.1.1.4.2. Imaginary time method The semiclassical action can also be extended to the complex time t_c, giving rise to so-called *complex classical trajectories* (sometimes also referred as *quantum orbits*[73]). The ITM enables to describe the movement of the electron through the tunnel barrier[74] and, thus, naturally includes the ionization process, which needs to be added artificially to the SMM by weighting trajectories with the static ionization rate. Additionally, it is applicable for all values of γ.

The integration in Eq. (2.57) needs to be evaluated in the complex plane and, thus, the trajectory becomes complex as well:

$$\boldsymbol{r}_\mu(t_\mathrm{c}) = \frac{\partial S_0(t_\mathrm{c})}{\partial \boldsymbol{p}(t_\mathrm{c})} \tag{2.70}$$

$$= \int_{t_s}^{t_\mathrm{c}} \mathrm{d}t'_\mathrm{c} \boldsymbol{v}(t'_\mathrm{c}) \tag{2.71}$$

with initial velocity $\boldsymbol{v}(t_s)^2 = (\boldsymbol{p}(t_s) - e\boldsymbol{A}(t_s))^2 = -\kappa$ and position $\boldsymbol{r}(t_s) = 0$ at the complex time of ionization $t_s = t_\mu + i\tau_\mu$. The trajectories follow the Newton's law of motion $\ddot{\boldsymbol{r}}(t_\mathrm{c}) = e\boldsymbol{F}(t_\mathrm{c})$. One can find that the complex trajectory in the complex time plane $t_\mathrm{c} = t + i\tau$ has the form:

$$\begin{aligned}\boldsymbol{r}_\mu(t_\mathrm{c}) = \boldsymbol{p}(t_\mathrm{c})(t - t_\mu) - \frac{eF}{\omega^2}\left(\cos\omega t \cosh\omega\tau - \cos\omega t_\mu \cosh\omega\tau_\mu\right) \\ + i\left(\boldsymbol{p}(t_\mathrm{c})(\tau - \tau_\mu) + \frac{eF}{\omega^2}\left(\sin\omega t \sinh\omega\tau - \sin\omega t_\mu \sinh\omega\tau_\mu\right)\right)\end{aligned} \tag{2.72}$$

The second (imaginary) part in Eq. (2.72) needs to be small to yield significant contributions to the integral in Eq. (2.35). In the tunneling ionization regime in linear polarized laser fields, this condition predicts that the ionization rate is maximal at zero momentum. The ionization amplitude M has the form[60, 75, 76]:

$$M(\boldsymbol{p}, t_\mathrm{D}) \approx \sum_\mu P(\boldsymbol{p}(t_\mathrm{c}), t_s) \exp\left(i(W_0(\boldsymbol{r}_\mu(t_\mathrm{c}), t_\mathrm{D}) + F_0(\boldsymbol{r}_\mu(t_\mathrm{c}), t_\mathrm{D})\right) \tag{2.73}$$

with

$$W_0(\boldsymbol{r}_\mu, t_\mathrm{D}) = -E_\mathrm{B}(t_\mathrm{D} - t_s) + \int_{t_s}^{t_\mathrm{D}} \mathrm{d}t'_\mathrm{c} \frac{1}{2}\boldsymbol{v}^2(t'_\mathrm{c}) + e\boldsymbol{F}(t'_\mathrm{c}) \cdot \boldsymbol{r}(t'_\mathrm{c}) \tag{2.74}$$

$$F_0(\boldsymbol{r}_\mu, t_\mathrm{D}) = -\boldsymbol{r}_\mu(t_\mathrm{D}) \cdot \boldsymbol{p}(t_\mathrm{D}) \tag{2.75}$$

$$P(\boldsymbol{p}, t_s) = 2C_{\kappa,l}\sqrt{\frac{i\kappa}{S''_\mu}}\,\mathrm{Y}_{l,m}\left(\frac{\boldsymbol{v}(t_s)}{\kappa}\right) \tag{2.76}$$

$$C_{\kappa,l} = \frac{2^{2\nu-2}}{\nu\Gamma(\nu + l + 1)\Gamma(\nu - l)} \quad , \tag{2.77}$$

where $\Gamma(x)$ represents the gamma function.

The application of semiclassical trajectories leads to a comprehensive description and, furthermore, allows to extend the quantum-mechanical interaction in terms of perturbation theory to more complicated systems.

2.1.1.5. Secondary effects in above-threshold ionization

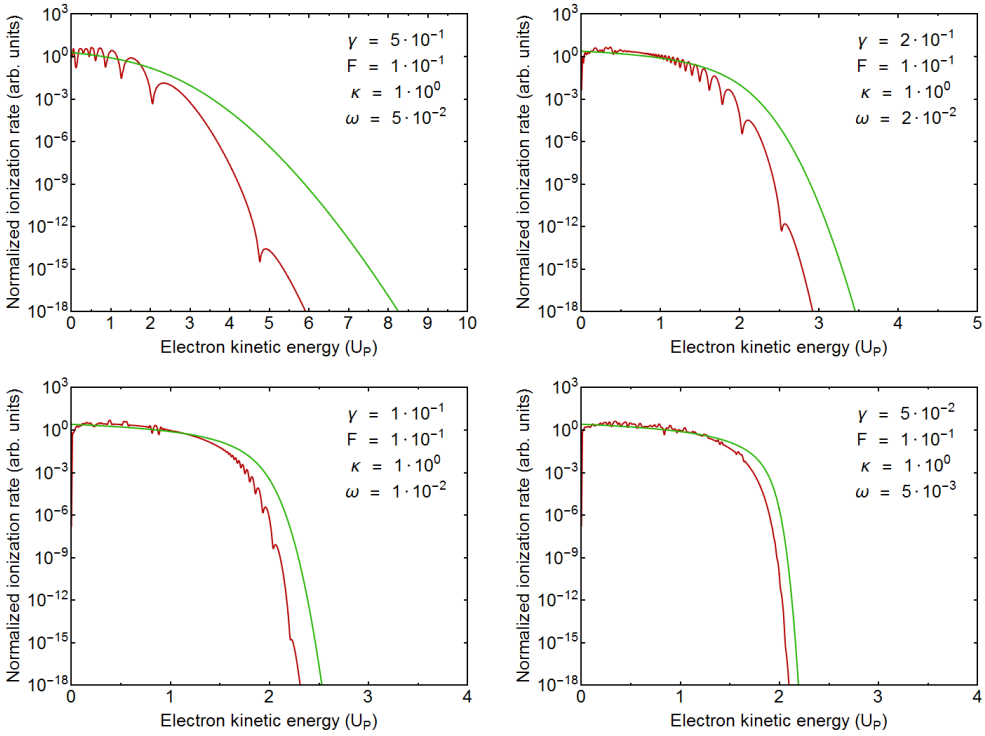

Figure 2.4.: Comparisons of the ITM (green) and the quantum-mechanical model (red) presented in Sec. 2.1.1.2 for different values of γ. In contrast to the SMM (see Fig. 2.3), the ITM yields a qualitatively correct result for large γ.

2.1.1.5.1. Channel closing in strong-laser fields The energy conservation (Eq. (2.55)) leads to the intensity dependence in the final electron momentum. For $F\omega^{-1} \gg \kappa$ the shift induced by the AC Stark effect leads to a closing of the s-th channel if

$$(n_{\min} + s)\omega < \frac{\kappa^2}{2} + \mathrm{U_P} \quad , \tag{2.78}$$

with the lowest-order ionization channel is defined by

$$n_{\min} = \left\lceil \frac{\kappa^2}{2\omega} \right\rceil \quad . \tag{2.79}$$

Here $\lceil x \rceil$ denotes the integral part of x. Thus, the increase of the intensity of the laser field closes the lower ionization channels[77].

2.1.1.5.2. Ponderomotive shift and broadening The oscillating laser field introduces an additional non-static potential experienced by the free electron. Due to the spatial inhomogeneity of the laser field (the Gaussian intensity distribution in the laser focus) the electron will be accelerated in this potential while it propagates out of the interaction volume, as described in Ref.[78, 79] and shown experimentally in Ref.[80, 81]. The energy

gain ΔE is:

$$\Delta E = +\frac{F^2}{4\omega^2} = \mathrm{U_P} \quad , \tag{2.80}$$

compensating the negative shift in the kinetic energy caused by the laser potential in the final electron energy (Eq. (2.55)). If the laser pulse is sufficiently long so that the electron moves out of the laser focus in the presence of the external field the kinetic energy is:

$$E'_f = \frac{\boldsymbol{p}'(t)^2}{2} = \frac{\boldsymbol{p}(t)^2}{2} + \mathrm{U_P} \tag{2.81}$$

$$= n\omega - \frac{\kappa^2}{2} \tag{2.82}$$

The ponderomotive energy shift and gain was the reason why the Keldysh-like theories led to incorrect predictions of the final electron energy spectrum. This matter was finally revealed by the application of ultrashort (picosecond to sub-picosecond) pulses by *Freeman*[80] and *Agostini*[82]. In a short pulse, the electron cannot escape the interaction volume while the ponderomotive acceleration potential is present and, thus, cannot gain additional energy. The electron distribution in a short laser pulse, therefore, carries records the electron momenta arising at the moment of ionization[80]. The influence of the ponderomotive shift on the final electron kinetic energy spectrum for different pulse durations and intensities can be seen in Fig. 2.5. As the short-pulse condition with regard to ponderomotive shift is dependent on the energy, intensity, and intensity gradient (local field) a broadening of the spectrum can be observed. Electron energies in strong-field experiments are typically of the order of tens of eV up to several keV, whereas a laser beam is typically focused to a spot of a few µm size. The short-pulse condition can be represented by:

$$\tau \ll b\sqrt{\frac{m_\mathrm{e}}{2E}} \tag{2.83}$$

It implies that the electron with a kinetic energy E does not leave the laser pulse of duration τ and beam waist (FWHM) b. Considering an ionized electron of 1 keV kinetic energy moving out of the laser focus of 10 µm size the short-pulse condition is:

$$\tau \ll 10\,\mu\mathrm{m}\sqrt{\frac{m_\mathrm{e}}{2 \cdot 1\,\mathrm{keV}}} \tag{2.84}$$

$$\ll 0.5\,\mathrm{ps} \tag{2.85}$$

To further reduce the influences of the ponderomotive shift and broadening, flat-top pulses of short duration ($\ll 1$ ps) with large foci and Rayleigh length can be employed.

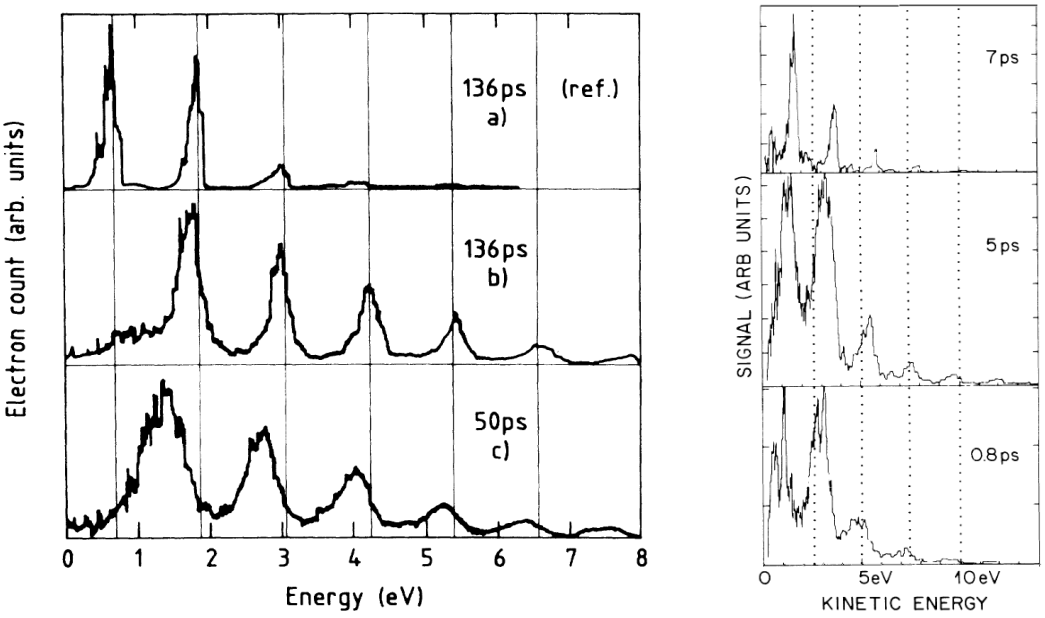

Figure 2.5.: Kinetic energy spectra in the short and long pulse regimes. Shown are ATI emission spectra of xenon recorded at different pulse durations ranging from the long-pulse-regime to the short-pulse-regime. The pulse durations are indicated in the panels. Left: Emission recorded at the laser peak intensities of $2.2 \times 10^{12}\,\mathrm{W\,cm^{-2}}$ (a) and $7.5 \times 10^{12}\,\mathrm{W\,cm^{-2}}$ (b and c) and with a central wavelength of 532 nm. Reprinted figure with permission from [Agostini et al.[82], Physical Review A, 36, 4111 (1987)] Copyright (1987) by the American Physical Society. Right: Emission recorded with pulse energies of 0.5 mJ (a) and $7.5 \times 10^{12}\,\mathrm{W\,cm^{-2}}$ (b and c) and with a central photon energy of 2.01 eV. The broadening and shift of the ATI energy peaks are evident in the figure. Reprinted figure with permission from [Freeman et al.[80], Physical Review Letters, 59, 1092 (1987)] Copyright (1987) by the American Physical Society.

2.1.1.5.3. Freeman resonances The low-energy part of the ATI spectrum in the short-pulse regime (as in the right panel of Fig. 2.5) reveals additional very sharp features originating from resonant multiphoton ionization[80, 83, 84]. Their appearance in the short-pulse regime can be explained by the induced energy shift due to the AC Stark effect. The large AC Stark shift in ultrashort pulses leads to a sudden energy match with energetically narrow long-lived Rydberg states, increasing the multiphoton transition rate of specific ionization channels. As a certain intensity is required for the AC Stark shift to induce these so-called Freeman resonances, they are only observable for certain ionization instants within the pulse and, thus, the final electron kinetic energy of the resonant-enhanced ionization is recorded at a specific local intensity. Intensity dependent shifts according to Eq. (2.55) are, thus, not observable, as U_P is fixed for each resonance[85]. Freeman resonances create a series of sharp peaks above the threshold as the non-resonant ionization channel can be used to directly map high-energetic bound states into the

continuum. Such a series can be observed for each ATI-peak. However, their appearance is more remarkable for lower kinetic energies[80, 83]. As the dipole transition moment from an atomic ground state to highly excited states is considerably low and requires large photon energies, lying in the extreme ultraviolett (XUV) range multiphoton resonant excitation plays an important role for populating and studying the Rydberg states.

2.1.1.5.4. Focal averaging The intensity profile $I(\rho, z, t)$ of the applied pulse in strong-field experiments is typically of a Gaussian shape in time and space:

$$I(\rho, z, t) = I_0 \left(\frac{w_0}{w(z)}\right)^2 \exp\left(-2\left(\frac{\rho}{w(z)}\right)^2\right) \exp\left(-\left(\frac{t - z/c}{\tau}\right)^2\right) \quad , \tag{2.86}$$

where I_0 is the peak intensity of the beam ($I_0 = F^2$ for a linear polarized beam), ρ defines the radial distance to the beam propagation axis,

$$w(z) = w_0 \sqrt{1 + \left(\frac{z}{z_0}\right)^2} \tag{2.87}$$

is the beam waist at the position z along the beam, w_0 is the minimal beam waist at $z = 0$ (also denoted as focus size), τ is the duration of the pulse, and

$$z_0 = \frac{\pi w_0^2}{\lambda} \tag{2.88}$$

is the Rayleigh range of the beam with a wavelength $\lambda = c\tau$.

Simulation of the electron emission ionized by a Gaussian beam requires integration over all electron trajectory calculated at a local intensity, weighted by the probability to find such an intensity within the intensity profile. The focal averaged yield w', thus, can be represented as:

$$w'(I_0) = \int_0^\tau \mathrm{d}t \int_{-\infty}^{\infty} \mathrm{d}z \int_0^\infty \mathrm{d}\rho w(I(\rho, z, t)) \tag{2.89}$$

However, electron detection often is limited in beam propagation direction within the Rayleigh range and an effective position, $\bar{z}$, with $|z| \leq \bar{z} \ll z_0$ and, accordingly, $w(z) \approx w(\bar{z}) = w_0$ so that a change of variable yields[77]

$$w'(I_0) \propto \int_0^{I_0} \mathrm{d}I w(I) \frac{1}{I} \sqrt{\ln\left(\frac{I_0}{I}\right)} \quad , \tag{2.90}$$

where $w(I)$ is the intensity-dependent ionization rate.

2.1.1.6. Coulomb correction

As discussed above, the KA is inherently imprecise because of the negligence of the parent potential in the final ionized state. The usage of the Volkov final state Eq. (2.27) reduces its application to zero- or short-range potentials (e.g. in the case of ATD) were it yields

excellent agreement in the long-wavelength limit[86]. However, in the case of ATI the parent potential (e.g. the Coulomb potential) affects the electron motion even at larger distances, resulting in strong variations of the yield described by Eq. (2.49) especially for higher residual charge states and low electron kinetic energies[87, 88]. Treating the Coulomb field in a non-perturbative way is not straightforward[60]. However, there are some approaches that will be discussed below.

2.1.1.6.1. Static ionization rate The total ionization rate in the static limit including the Coulomb interaction scales linearly with the non-Coulomb ionization rate[89, 90]:

$$w_{\mathrm{ATI}} = Q_{\mathrm{C}} w_{\mathrm{ATD}} \tag{2.91}$$

where $Q_{\mathrm{C}} = \exp\left(-2\,\mathrm{Im}\,W_1\right)$ is the Coulomb factor and W_1 is the perturbation correction to the reduced non-Coulombic action W_0. The Coulomb factor can be approximated by the Coulomb-corrected ITM approach, the so-called trajectory-based Coulomb-corrected strong-field approximation (TCSFA). More details are presented in Sec. 2.1.1.6.4. One can show that the Coulomb factor[60]

$$Q_{\mathrm{C}} = \left(\frac{2\kappa^3}{F}\right)^{2\nu} \left(\frac{1}{2\gamma}\right)^{2\nu} \tag{2.92}$$

is numerically large for all values of γ. The ionization enhancement was shown in several experiments[91, 92] to become increasingly important for higher residual charge states where the non-Coulombic KA fails to describe the experimental results.

2.1.1.6.2. The Coulomb-Volkov approximation The CVA extends the SFA approach by taking the final state Coulomb potential of the charged parent core due to the ionization process (ATI) into account. The Volkov function in Eq. (2.27) will then transform into the Coulomb-Volkov wave function[93, 94]:

$$A_{\boldsymbol{p},n} \approx \langle {\boldsymbol{\Psi}^{\mathrm{CV}}}_{\boldsymbol{p}}(t)|\, \hat{V}_{\mathrm{int}}\, |\boldsymbol{\psi}_0(t)\rangle \tag{2.93}$$

$$\begin{aligned} {\boldsymbol{\Psi}^{\mathrm{CV}}}_{\boldsymbol{p}}(t) = {} & \frac{1}{(2\pi)^{\frac{3}{2}}} \exp\left(\frac{\pi}{2p}\right) \Gamma\left(1+\frac{i}{p}\right) \exp\left(i\boldsymbol{p}(t)\cdot\boldsymbol{r}(t)\right) \\ & \times {}_1\mathrm{F}_1\left(-\frac{i}{p}, 1, -i(pr + \boldsymbol{p}(t)\cdot\boldsymbol{r}(t))\right) \\ & \times \exp\left(i\boldsymbol{A}(t)\cdot\boldsymbol{r}(t) - \frac{i}{2}\int_{-\infty}^{t} \mathrm{d}t' \boldsymbol{v}^2(t')\right) \end{aligned} \tag{2.94}$$

where ${}_1\mathrm{F}_1(x)$ denotes the hypergeometric function. This description, however, implies a numerical integration over the highly oscillating Volkov function as there is so far no closed-form expression as Eq. (2.49) for the non-Coulombic (ATD) case. The CVA was shown to improve the qualitative agreement with TDSE calculations for $\gamma \geq 1$ especially

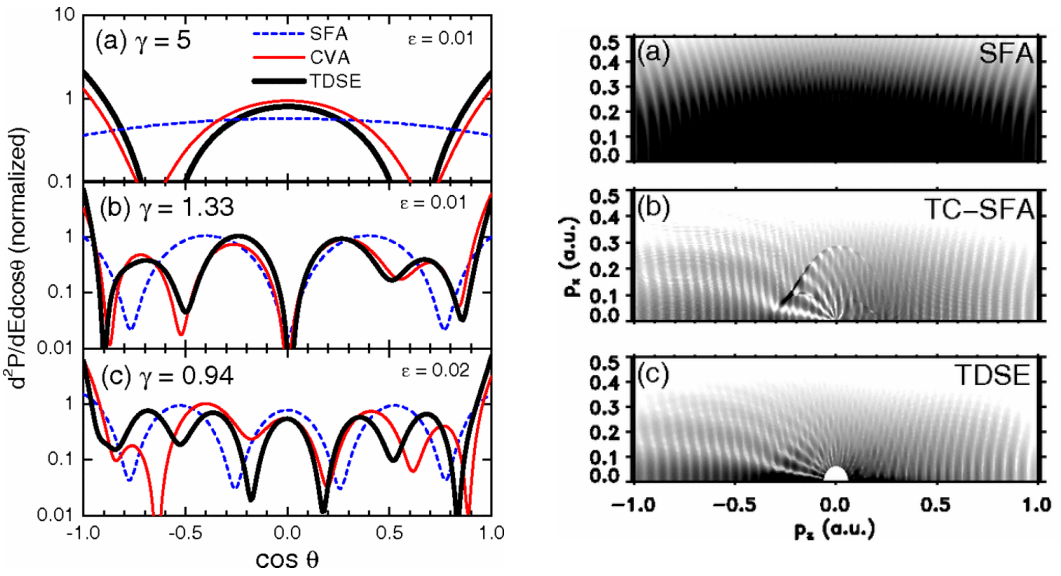

Figure 2.6.: Comparison of two methods to include the Coulomb correction of the KA. The results are shown together with the original SFA and TDSE calculations. Left: CVA approach; The final state includes the Coulomb distortion due to the parent ion. Reprinted figure with permission from [Arbó et al.[15], Physical Review A, 77, 013401 (2008)] Copyright (2008) by the American Physical Society. Right: TCSFA approach; The transition amplitude is corrected on the basis of complex trajectory and "sub-barrier motion" considerations. Reprinted figure with permission from [Yan et al.[16], Physical Review Letters, 105, 253002 (2010)] Copyright (2010) by the American Physical Society.

for low electron momenta[15]. Additionally, the Coulomb correction showed a symmetry breakdown from fourfold to twofold symmetry in elliptically polarized laser fields[95, 96] as reported in experiments[97, 98, 99] and contradicting the SFA without Coulomb correction. A comparison of SFA and CVA with TDSE calculations is shown in Fig. 2.6.

2.1.1.6.3. Coulomb-corrected simple-man model Extension of the SMM is straightforward due to its simplistic nature and is done by adjusting Eq. (2.59) by adding the Coulomb potential term:

$$\ddot{\boldsymbol{r}}(t) \rightarrow \ddot{\boldsymbol{r}}_{\mathrm{CC}}(t) = e\boldsymbol{F}(t) + \frac{eZ\boldsymbol{r}_{\mathrm{CC}}(t)}{\|\boldsymbol{r}_{\mathrm{CC}}(t)\|^3} \quad . \tag{2.95}$$

However, the extension of the SMM for larger γ within the Coulomb correction is not possible as the chosen barrier exit $\boldsymbol{b}$ affects the final electron momentum spectrum which contradicts the missing ionization path-dependence of the ITM within the complex-time plane.[60]

2.1.1.6.4. Trajectory-based Coulomb-corrected strong-field approximation The ITM can be as well extended towards inclusion of the parental Coulomb field by application of the perturbation theory if the perturbing electric field is small (final charge of the parent needs to be small, and distance to the parental ion large):

$$\boldsymbol{r}'_\mu(t_\mathrm{c}) \to \boldsymbol{r}_\mu(t_\mathrm{c}) + \boldsymbol{r}_{\mu_1}(t_\mathrm{c}) + \dots \tag{2.96}$$

$$W' \to W_0 + W_1 + \dots \tag{2.97}$$

where $\boldsymbol{r}(\mathrm{t})$ and W_0 are defined in Sec. 2.1.1.4.2 and $\boldsymbol{r}_{\mu_1}(t_\mathrm{c})$ and W_1 denote corresponding corrections due to the Coulomb interaction. The complexity of this approach is a consequence of the singularity of the potential near the parent ion that needs to be handled by regularization[100, 60] where otherwise the perturbation would be significant. A detailed description of the TCSFA approach is summarized elsewhere[100, 101, 102]. The TCSFA approach shows well agreement with TDSE calculations and shows important features of the Coulomb correction the symmetry breakdown in elliptical fields[100] and low-energy structures not observable in the pure SFA approach.

2.1.2. High-order above threshold ionization

After the ionization step the electron can oscillate in the vicinity of the parent and scatter on its potential. Due to momentum conservation a free electron can not absorb additional photons and the final electron momentum, thus, is only defined by the initial phase of the field (see Eq. (2.48)) during the ionization instant. However, during the rescattering on the parent potential the electron can gain or loose energy. This process called high-order above threshold ionization (high-order ATI (HATI)) can significantly increase the final electron kinetic energy and yields a plateau in the final electron emission spectrum[103].

2.1.2.1. Transition amplitude

The transition amplitude can be calculated by extension of Eq. (2.27) by the HATI amplitude (first described by Refs.[104, 22] and in more detail e.g. in Refs.[77, 105]:

$$\begin{aligned} A_{\boldsymbol{p},n} \approx & \int_{-\infty}^{\infty} \mathrm{d}t \langle \boldsymbol{\Psi}_{\boldsymbol{p}}(t)| \hat{V}_\mathrm{int} |\boldsymbol{\psi}_0(t)\rangle \\ & + \int_{-\infty}^{\infty} \mathrm{d}t_\mu \int_{t_\mu}^{\infty} \mathrm{d}t \langle \boldsymbol{\Psi}_{\boldsymbol{p}}(t)| \hat{V}_\mathrm{A} U_\mathrm{L}(t_1, t_\mu) \hat{V}_\mathrm{int}[t_\mu] |\boldsymbol{\psi}_0(t_\mu)\rangle \end{aligned} \tag{2.98}$$

or for an harmonic laser field with period τ

$$A_{\boldsymbol{p},n} \approx \frac{1}{\tau}\int_0^\tau \mathrm{d}t\langle \boldsymbol{\Psi}_{\boldsymbol{p}}(t)|\,\hat{V}_{\mathrm{int}}\,|\boldsymbol{\psi}_0(t)\rangle \tag{2.99}$$

$$+\frac{1}{\tau}\int_0^\tau \mathrm{d}t_\mu \int_{t_\mu}^\infty \mathrm{d}t\langle \boldsymbol{\Psi}_{\boldsymbol{p}}(t)|\,\hat{V}_{\mathrm{A}}U_{\mathrm{L}}(t_1,t_\mu)\hat{V}_{\mathrm{int}}[t_\mu]\,|\boldsymbol{\psi}_0(t_\mu)\rangle \tag{2.100}$$

where $\hat{V}_{\mathrm{A}}$ is the atomic potential of the parent, $U_{\mathrm{L}}(t_1,t_\mu)$ is the propagator of the volkov hamiltonian, t_μ and t_1 define the instant of ionization and revisit, respectively.

One can directly interpret the integral on the right hand side as three-step model: First the electron is ionized at instant t_μ , then propagates in the laser field until at instant t_1 the quasi-free electron scatters on its parent's atomic potential. This process, sometimes also referred as rescattering, is used to quantitatively describe the ionization yield for large final electron kinetic energies, where the pure ATI formalism significantly (e.g. by 40 orders of magnitude[106]) disagrees. One can as well directly see that interference effects between ATI and HATI can be observed in the region where the the ATI and HATI contributions to the total ionization rate are of similar magnitude (i.e. in the region around the ATI cut-off).

2.1.2.2. Saddle-point method

In the same sense as in Sec. 2.1.1.2 the integral can be interpreted in terms of the saddle-point method[12, 105] with a large semiclassical action $S_0(t)$ in the exponential function leading to three rescattering conditions where the action is stationary with respect to the intermediate electron momentum $\boldsymbol{p}_i$(t) and its time-derivative zero[107]:

$$\begin{aligned}
\mathrm{I}: [\boldsymbol{p}_i(t)+\boldsymbol{A}(t_\mu)]^2 &= -\kappa^2 \\
\mathrm{II}: \ \boldsymbol{p}_i(t)=\boldsymbol{p}_{\mathrm{S}}(t) \quad &= -\frac{1}{t_1-t_\mu}\int_{t_\mu}^{t_1}\mathrm{d}t'\boldsymbol{A}(t') \\
\mathrm{III}: [\boldsymbol{p}_{\mathrm{S}}(t)+\boldsymbol{A}(t_1)]^2 &= [\boldsymbol{p}(t)+\boldsymbol{A}(t_1)]^2
\end{aligned} \tag{2.101}$$

The first term describes the condition of the direct ionization process (ATI) (first step of the three-step model) which is essentially the same as Eq. (2.41). The second condition describes the requirement for the electron to revisit its parent with intermediate momentum $\boldsymbol{p}_{\mathrm{S}}$(t) and, thus, restricts the amount of allowed trajectories contributing to the HATI yield (second step). The third condition, finally, describes the energy conservation rule during the revisit that leads to the final electron kinetic energy (third step).

2.1.2.3. Semiclassical trajectories

The description by the saddle-point method allows to interpret the HATI process with semiclassical models analogous to the semiclassical interpretation of the ATI process in Sec. 2.1.1.4. Additionally, to the acceleration by the external laser field the implementation of semiclassical trajectories has to fulfill Eq. (2.101).

2.1.2.3.1. Simple-man model In the SMM the electron emitted at the tunnel exit $\boldsymbol{b}$ has to revisit the parent during instant t_1 satisfying condition II. This condition can be reformulated by the existence of solutions for the scattering phase $\Phi_1 = \omega t_1$ of the transcendental equation:

$$\boldsymbol{r}(t_1) = 0 \tag{2.102}$$

$$\cos\Phi_1 - \cos\Phi_\mu = +\frac{\gamma^2}{e\cos 2\Phi_\mu} - (\Phi_1 - \Phi_\mu)\omega\sin\Phi_\mu\,, \tag{2.103}$$

where $\Phi_\mu = \omega t_0$ represents the laser phase during the ionization. One can see that only a part of the launched electron trajectories can revisit their parent (see Fig. 2.1.2.3.1a) for solutions of Eq. (2.103)).

During the scattering process the electron can absorb photons satisfying III. This process is treated in the SMM by an elastic scattering process[18] transferring a part of the electron velocity from the parallel velocity component $v_\parallel$ towards the perpendicular component $v_\perp$ under the scattering angle θ_S:

$$v_\parallel = \frac{eF}{\omega}\left(\cos\theta_\mathrm{S}\left(\sin\Phi_1 - \sin\Phi_\mu\right) + \sin\omega t - \sin\Phi_1\right) \tag{2.104}$$

$$v_\perp = \frac{eF}{\omega}\left(\sin\theta_\mathrm{S}\left(\sin\Phi_1 - \sin\Phi_\mu\right)\right) \tag{2.105}$$

and yields the final kinetic energy $T = 1/2\,\langle \boldsymbol{p}(t)^2\rangle_t$:

$$T = \frac{1}{2\tau}\int_0^\tau \mathrm{d}t(\boldsymbol{v}(t) + e\boldsymbol{A}(t))^2 \tag{2.106}$$

$$= 2\mathrm{U_P}\left(\sin^2\theta_\mathrm{S}\left(\sin\Phi_\mu - \sin\Phi_1\right)^2 + \left(\cos\theta_\mathrm{S}\left(\sin\Phi_\mu - \sin\Phi_1\right) + \sin\Phi_1\right)^2\right) \tag{2.107}$$

where the final emission angle with respect to the laser polarization axis is given by[18]:

$$\cot\theta = \cot\theta_\mathrm{S} - \frac{\cos\Phi_1}{(\cos\Phi_1 - \cos\Phi_\mu)\sin\theta_\mathrm{S}} \tag{2.108}$$

Effectively, the scattering process allows to adjust the relative phase of the oscillatory electron motion in laser polarization direction with respect to the laser phase which leads to a further acceleration of the electron after the scattering process. The highest kinetic energy during the revisit but before the scattering is denoted by $\approx$3.17 $\mathrm{U_P}$ and represents a limit in the production of up-converted photons via high harmonic generation (HHG). The cutoff-energy for the kinetic energy of electrons after the scattering disregarding II is 18 $\mathrm{U_P}$. However, restriction due to II leads to exclusion of some trajectories and, thus,

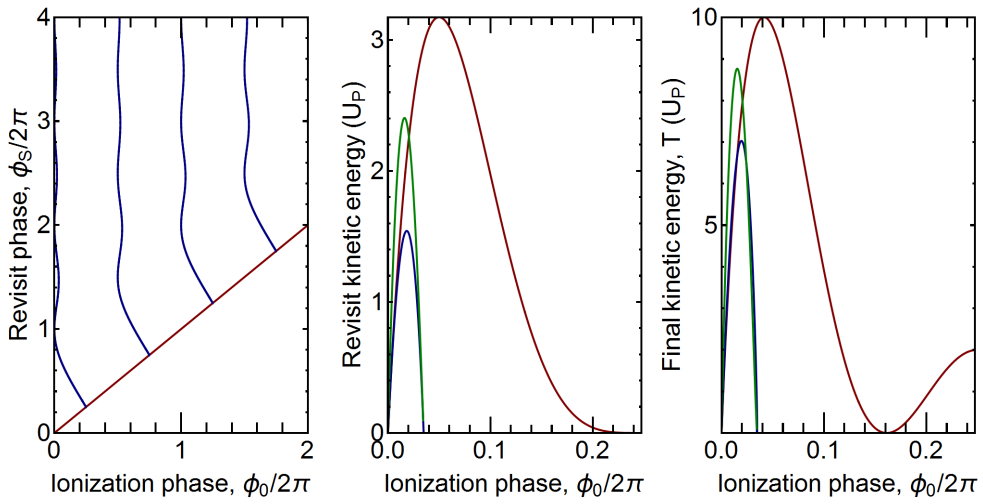

Figure 2.7.: Trajectory characteristics for electrons undergoing HATI (for $\gamma \to 0$): a) Classical solutions of the revisit condition II (Eq. (2.101)). Ionization occurs along the red line while revisiting takes place along the blue line. Only a part of the launched trajectories can undergo scattering. However, electrons can scatter on the parent core at different revisits phases. b) Electron kinetic energy during the revisit but before the scattering. Different colors represent consecutive revisits satisfying II (red, blue, and green denote the first, second, and third revisit, respectively). With increasing the time interval between the ionization and the scattering events, the maximal intermediate kinetic energy is reduced. For the first visit, the cut-off lies at $\approx 3.17\,U_P$. c) Time-averaged final kinetic energy, T, after scattering under angle $\theta_S = \pi$. The high-energy cut-off is given by $\approx 10\,U_P$.

yields the numerical maximum $10.0076\,U_P$ for $\Phi_\mu \approx 0.261$ and $\Phi_1 \approx 4.567$. Significantly increased kinetic energies with respect to the ATI process only occur for backward scattering ($\theta_S = \pi$). For forward scattering ($\theta_S = 0$) the high-energy cut-off remains unchanged at $2\,U_P$.

2.1.2.3.2. Semiclassical scattering cross-section The scattering cross-section weights trajectories connected by the initial (ATI) and final (HATI) kinetic energy distribution through Eq. (2.101). The full quantum-mechanical description Eq. (2.100) already includes the influence of the atomic potential which is, however, lacking in the semiclassical approach presented above. One possibility is to consider the HATI process as a laser-assisted scattering process (as discussed in Sec. 2.3). The laser-assisted scattering cross-section can be obtained employing scattering descriptions given by Bunkin and Federov[108] in the first Born approximation and by Kroll and Watson[109] in the soft-photon approximation. The details will be discussed later and just the result from the Kroll-Watson approximation (KWA) will be shown here under the assumption that II is satisfied:

$$\frac{\mathrm{d}w_{n_{\mathrm{HATI}}}(p,\theta)}{\mathrm{d}\Omega} = \frac{p}{p_\mathrm{i}}\,\mathrm{J}^2_{n_{\mathrm{HATI}}}\left(\hat{\boldsymbol{\epsilon}_\mathrm{L}}\cdot(p_\mathrm{i}-p)\frac{F}{\omega^2}\right)\frac{\mathrm{d}w_{n_{\mathrm{ATI}}}(p_\mathrm{i},\theta_\mathrm{i})}{\mathrm{d}\Omega} \tag{2.109}$$

with final electron momentum:

$$p = \sqrt{2\left((n_{\mathrm{ATI}}+n_{\mathrm{HATI}})\omega - \frac{\kappa^2}{2} - \mathrm{U_P}\right)} \tag{2.110}$$

where n_{ATI} (n_{HATI}) is the amount of absorbed photons for the ATI (HATI) process, p_i describes the intermediate momentum before the scattering process, θ_i and θ describe the intermediate and final emission angle, respectively, and $\frac{\mathrm{d}w_{n_{\mathrm{ATI}}}}{\mathrm{d}\Omega}(p_\mathrm{i},\theta_\mathrm{i})$ denotes the ATI ionization cross-section.

2.2. Ionization in weak or moderate electromagnetic fields

In this section photoexcitation and photoionization by weak laser fields is considered. If the contribution of the interaction potential $\hat{V}_{\mathrm{int}}$ to the total Hamiltonian $\hat{H}$ is small in comparison to the atomic Hamiltonian $\hat{H}_\mathrm{A}$, the description of the quantum-mechanical ionization process can be obtained by application of the perturbation theory. The initial state $|\boldsymbol{i}\rangle$, possible intermediate states $|\boldsymbol{m}\rangle$, the final ionized state $|\boldsymbol{f}\rangle$ are considered to be exact solutions of the atomic Hamiltonian and connected by the interaction $\hat{V}_{\mathrm{int}}$ [110]:

$$\hat{H}_\mathrm{A}\,|\boldsymbol{i}\rangle = E_i\,|\boldsymbol{i}\rangle \tag{2.111}$$

$$\hat{H}_\mathrm{A}\,|\boldsymbol{m}\rangle = E_m\,|\boldsymbol{m}\rangle \tag{2.112}$$

$$\hat{H}_\mathrm{A}\,|\boldsymbol{f}\rangle = E_f\,|\boldsymbol{f}\rangle \tag{2.113}$$

$$|\boldsymbol{i}\rangle \xrightarrow{\hat{V}_{\mathrm{int}}} |\boldsymbol{m}\rangle \xrightarrow{\hat{V}_{\mathrm{int}}} \cdots \xrightarrow{\hat{V}_{\mathrm{int}}} |\boldsymbol{f}\rangle \tag{2.114}$$

where all allowed intermediate states need to be considered. A careful analysis of the considered initial and measured final state, therefore, enables the possibility to study the intermediate states or the transition itself. This technique is employed in time-resolved photo-excitation techniques (see Sec. 7).

For such light matter interactions conservation rules of energy and momentum need to be considered. Assuming monochromatic light the energy conservation law can be written as:

$$E_i + n\omega = E_f + n'\omega \tag{2.115}$$

where E_i and E_f denotes the ground and final state energy of the corresponding state (as defined above) in the presence of n and n' photons of energy ω, respectively. One often separates into distinct cases of photon interaction (i.e. $n > n'$ denotes photon absorption, $n < n'$ photon emission, $n = n'$ elastic photon scattering). The energy conservation rule

should be applied to all transitions during the ionization process but can be less strict within a short-time interval because of the Heisenberg uncertainty limit.

In the case of photon absorption or emission the energy and momentum conservation rules restrict transitions resulting in the so-called selection rules. Depending on the approximation these are further qualified as dipole-, quadrupol, or higher multipole selection rules (see Sec. 2.2.2).

2.2.1. Perturbation ansatz

In the first order perturbation theory (the light perturbs the atomic Hamiltonian $\hat{H}_\mathrm{A}$ as $\hat{V}_\mathrm{int}$), Fermi's Golden Rule expresses the transition probability from the ground state to the final state as:

$$\Gamma_{i\to f} \propto \left|\langle \boldsymbol{f}|\, \hat{V}_\mathrm{int}\, |\boldsymbol{i}\rangle\right|^2 \delta\left(E_i - E_f \pm \omega\right) \tag{2.116}$$

where the argument of the δ-function represents the single-photon energy conservation law as discussed above. It is noteworthy that the time-dependence of the interaction vanishes for sufficiently weak fields yielding a constant transition rate and, thus, the exponential decay known from the solution of the Pauli Master Equation (PME) which is discussed in more detail in Sec. 7.2.

2.2.2. Electric dipole approximation

$\hat{V}_\mathrm{int}$ can be simplified in terms of the electron momentum $\boldsymbol{p}$ and the photon field component $\boldsymbol{A}$ using the Coulomb gauge ($\boldsymbol{\nabla}\cdot\boldsymbol{A}=0$) in the case of a weak electromagnetic field ($\boldsymbol{A}^2 \ll \boldsymbol{A}\cdot\boldsymbol{p}$) to:

$$\hat{V}_\mathrm{int} \propto \boldsymbol{A}\cdot\boldsymbol{p} \tag{2.117}$$

The plane-wave form of the electromagnetic field $\boldsymbol{A}$ can than be expressed in terms of $\exp\left(-i\boldsymbol{k}\cdot\boldsymbol{r}\right)$ resulting in the matrix element:

$$\left|\langle \boldsymbol{f}|\, \hat{V}_\mathrm{int}\, |\boldsymbol{i}\rangle\right|^2 \propto \left|\langle \boldsymbol{f}|\exp\left(-i\boldsymbol{k}\cdot\boldsymbol{r}\right)\hat{\boldsymbol{\epsilon}_\mathrm{L}}\cdot\boldsymbol{p}\,|\boldsymbol{i}\rangle\right|^2 \tag{2.118}$$

However, this expression can be expanded in terms of $i\boldsymbol{k}\cdot\boldsymbol{r}$ as:

$$\left|\langle \boldsymbol{f}|\exp\left(-i\boldsymbol{k}\cdot\boldsymbol{r}\right)\hat{\boldsymbol{\epsilon}_\mathrm{L}}\cdot\boldsymbol{p}\,|\boldsymbol{i}\rangle\right|^2 = \left|\langle \boldsymbol{f}|\left(1+O(-i\boldsymbol{k}\cdot\boldsymbol{r})\right)\hat{\boldsymbol{\epsilon}_\mathrm{L}}\cdot\boldsymbol{p}\,|\boldsymbol{i}\rangle\right|^2 \tag{2.119}$$

Ignoring all higher order terms $O(-i\boldsymbol{k}\cdot\boldsymbol{r})$ is known as the dipole approximation. Calculating possible transitions $\left|\langle \boldsymbol{f}|\,\hat{\boldsymbol{\epsilon}_\mathrm{L}}\cdot\boldsymbol{p}\,|\boldsymbol{i}\rangle\right|^2$ leads to the so-called dipole selection rules. Assuming (weak) LS-coupling in a multi-electron system these read:

$$\Delta J = 0, \pm 1 (0 \not\leftrightarrow 0) \tag{2.120}$$

$$\Delta M_J = 0, \pm 1 \tag{2.121}$$

$$\Delta S = 0 \quad , \tag{2.122}$$

where ΔJ, ΔM_J and ΔS describe the change in the total momentum, magnetic and spin quantum numbers between initial state $|\boldsymbol{i}\rangle$ and final state $|\boldsymbol{f}\rangle$, respectively. Consequently

the expression $\hat{\boldsymbol{\epsilon}}_{\mathrm{L}} \cdot \boldsymbol{p}$ is called electric dipole operator $\hat{\boldsymbol{\mu}}$.

2.2.3. Frozen core approximation

The analytic solution of the Schrödinger equation of a multi-body system is not possible and, thus, numerical approaches or approximations are required to describe such systems. In the atomic or molecular light-matter interaction electronic transitions can be described in the frozen core approximation regarding only a selected portion of electrons and consider all remaining electrons as inactive or "frozen". The inactive electrons are included in the Schrödinger equation and statically screen the Coulomb potential of the core. Other electron correlations between frozen and active electrons are disregarded. An approximation of a single active electron in an atom with frozen core electrons leads to a screened hydrogen-like potential (one electron system) which can be described analytically. This most simplified description represents the so-called single-active-electron (SAE) approximation.

2.2.4. Born-Oppenheimer approximation and Franck-Condon principle

For molecular systems not only the electronic wave function needs to be considered but as well nuclear vibrational and rotational wave functions. The Born-Oppenheimer approximation leads to a factorization of nuclear (ψ_n) and electronic (ψ_e) wave functions. Considering an initial state $|\boldsymbol{i}\rangle = |\psi_e, \psi_n\rangle$ and a final state $|\boldsymbol{f}\rangle = |\psi'_e, \psi'_n\rangle$ the Born-Oppenheimer approximation reads:

$$|\boldsymbol{i}\rangle \approx |\psi_e\rangle \times |\psi_n\rangle \tag{2.123}$$

$$|\boldsymbol{f}\rangle \approx |\psi'_e\rangle \times |\psi'_n\rangle \tag{2.124}$$

If $\hat{A}$ is an interaction operator that can be separated into electronic ($\hat{A}_e$) and nuclear ($\hat{A}_n$) parts and the transition probability $\langle \boldsymbol{f}| \hat{A} |\boldsymbol{i}\rangle$ can be simplified by application of the Born-Oppenheimer approximation and reads:

$$\langle \boldsymbol{f}| \hat{A} |\boldsymbol{i}\rangle = \langle \boldsymbol{f}| \hat{A}_e + \hat{A}_n |\boldsymbol{i}\rangle \tag{2.125}$$

$$\approx (\langle \psi'_e| \times \langle \psi'_n|)\hat{A}_e(|\psi_e\rangle \times |\psi_n\rangle) + (\langle \psi'_e| \times \langle \psi'_n|)\hat{A}_n(|\psi_e\rangle \times |\psi_n\rangle) \tag{2.126}$$

$$= \langle \psi'_n | \psi_n\rangle \times \langle \psi'_e| \hat{A}_e |\psi_e\rangle + \langle \psi'_e | \psi_e\rangle \times \langle \psi'_n| \hat{A}_n |\psi_n\rangle \quad . \tag{2.127}$$

One important application of the Born-Oppenheimer approximation represents the Franck-Condon principle. In the case of light-matter interaction of molecules the application of the electric dipole approximation requires the calculation of the electric dipole

transition probability

$$\langle \boldsymbol{f} | \, \hat{\boldsymbol{\mu}} \, | \boldsymbol{i} \rangle = \langle \psi_n' \, | \, \psi_n \rangle \times \langle \psi_e' | \, \hat{\boldsymbol{\mu}}_\mathrm{e} \, | \psi_e \rangle + \cancelto{0}{\langle \psi_e' | \, \psi_e \rangle} \times \langle \psi_n' | \, \hat{\boldsymbol{\mu}}_\mathrm{n} \, | \psi_n \rangle \tag{2.128}$$

$$= \langle \psi_n' \, | \, \psi_n \rangle \times \langle \psi_e' | \, \hat{\boldsymbol{\mu}}_\mathrm{e} \, | \psi_e \rangle \quad . \tag{2.129}$$

as electronic wave functions $|\psi_e\rangle$ are orthogonal and, thus, the integral $\langle \psi_e' \, | \, \psi_e \rangle$ is only non-zero for the trivial case $\psi_e' = \psi_e$.

Eq. (2.129) shows that the molecular transition probability can be calculated as the electronic transition probability multiplied with the nuclear wave function overlap simplifying the calculation significantly. The electronic wave function $|\psi_e\rangle$ and nuclear wave function $|\psi_n\rangle$ can further be separated into terms representing the spin, virbational, and rotational state of the system.

2.2.5. Sudden ionization

The ionization process itself can be considered as the transition of an electron from a bound state to a free (continuum) state. The energy conservation rule can be written as:

$$E_\mathrm{kin} = \omega - \Delta E \tag{2.130}$$

where ΔE describes the energy loss due to the ionization process and ω is the energy of the driving laser photon. In the SAE approximation ΔE represents the binding energy E_B and, thus, the energy threshold (ionization potential) for this ionization channel. The kinetic energy distribution then provides all necessary information to extract the binding energy E_B of the regarded orbital. As the orbital is defined by the atomic or molecular structure recording E_B can lead to identifications of different samples and their dynamics.

However, the SAE approximation might be violated and, thus, ΔE can not be interpreted in a direct way as binding energy. If more than one electron can be excited by the laser field the energy loss ΔE increases with the number of excitation channels ($\Delta E = (E_B + ...)$) resulting in a lower final energy of the electron. This so-called shake-up process, thus, increases the number of ionization channels. The opposing shake-down process is only observable for excited systems.

Even in the SAE approximation with a single electronic ionization channel vibronic transitions need to be considered. The overlap of initial and final electron wave-functions according to the Franck-Condon principle will result in a series of ionization channels energetically separated by the (an-)harmonic oscillator frequency. Such emission bands are often modeled by Gaussian functions (see Sec. 6.3.2 and Sec. 7.4.2). If rotational and vibrational excitation can be neglected (e.g. photoionization of atoms) the shape is solely defined by the transition moment and follows a Lorentzian (or more general a Fano) line-shape.

2.3. Electron scattering on atomic potentials

2.3.1. Elastic scattering

The scattering of an electron in the presence of the finite range potential can be described perturbatively by the S-Matrix formalism leading to the Born series for the perturbed final state, $|\mathbf{\Psi}_i(t)\rangle$, determined by the scattering potential $\hat{V}_\mathrm{A}$, the initial state $|\mathbf{\Psi}_i(t)\rangle$ and the Green function, G:

$$|\mathbf{\Psi}_f(t)\rangle = |\mathbf{\Psi}_i(t)\rangle + G(t,t')\hat{V}_\mathrm{A}\,|\mathbf{\Psi}_i(t)\rangle + G(t,t')\hat{V}_\mathrm{A}G\hat{V}_\mathrm{A}\,|\mathbf{\Psi}_i(t)\rangle + \ldots\,^{2} \tag{2.131}$$

which represents a solution of the Lippman-Schwinger equation for quantum-mechanical scattering:

$$|\mathbf{\Psi}_f(t)\rangle = |\mathbf{\Psi}_i(t)\rangle + G(t,t')\hat{V}_\mathrm{A}\,|\mathbf{\Psi}_f(t)\rangle \tag{2.132}$$

If the scattering potential is weak and, thus, multiple scattering negligible only the first two terms on the r.h.s. of Eq. (2.131) are considered. This approximation is denoted as (first) Born approximation. The integral $|\langle\mathbf{\Psi}_f(t)|\,\hat{V}_\mathrm{A}\,|\mathbf{\Psi}_i(t)\rangle|^2$ in the plane wave limit can then be simplified and the elastic scattering cross section, σ_el, expressed as:

$$\frac{\mathrm{d}\sigma_\mathrm{el}}{\mathrm{d}\Omega} \approx \left|\frac{1}{2\pi}\int \mathrm{d}\boldsymbol{r}\exp\left(-i\boldsymbol{q}\cdot\boldsymbol{r}\right)V_\mathrm{A}(\boldsymbol{r})\right|^2 \tag{2.133}$$

$$= \left|\frac{1}{2\pi}\widetilde{V}_\mathrm{A}(\boldsymbol{q})\right|^2 \tag{2.134}$$

where $\widetilde{V}_\mathrm{A}(\boldsymbol{q})$ represents the Fourier transformed atomic potential evaluated at the scattering momentum vector, $\boldsymbol{q}$, where

$$\boldsymbol{q} = \boldsymbol{k}_f - \boldsymbol{k}_i \tag{2.135}$$

With other words the elastic scattering cross-section only depends on the momentum space representation of the atomic potential.

2.3.2. Laser-assisted electron scattering on a potential

2.3.2.1. quantum-mechanical description

The process of an electron scattering on a short-range (atomic) potential, $\hat{V}_x$ in the presence of the laser field can as well be described in terms of the S-matrix formalism,

[2] Here the number of terms in the expansion minus one denotes the order of the nth Born approximation.

where the S-matrix can be represented in terms of the Green function, G [105]:

$$S_{fi} = i \lim_{t' \to \infty} \lim_{t \to -\infty} \langle \boldsymbol{\Psi}_f(t) | \, G(t,t') \, | \boldsymbol{\Psi}_i(t) \rangle \tag{2.136}$$

where $G(t,t')$ satisfies the Lippmann-Schwinger equation

$$G(t,t') = G_x(t,t') + \int \mathrm{d}t'' G(t,t'') \hat{V}_x G_x(t'',t') \tag{2.137}$$

and furthermore $G(t,t')$ corresponds to the total Hamiltonian, H, and $G_x(t,t')$ to the reduced Hamitonian, $\hat{H}_x$, without atomic potential but including the laser interaction, $\hat{V}_{\mathrm{int}}$, respectively:

$$\hat{H} = \hat{H}_x + \hat{V}_x \tag{2.138}$$

$$\hat{H}_x = \boldsymbol{k}^2(t)/2 + \hat{V}_{\mathrm{int}} \tag{2.139}$$

and the initial and final states($|\boldsymbol{\Psi}_i(t)\rangle$ and $|\boldsymbol{\Psi}_f(t)\rangle$, respectively) represent solutions to the reduced Hamiltonian i.e. Volkov states. Substituting the length-gauge representation of the Volkov states and $\hat{H}_x$ (see Sec. 2.1.1.1) leads to the Born expansion[111]:

$$\begin{aligned} S_{fi} = & -i \int_{-\infty}^{\infty} \mathrm{d}t \langle \boldsymbol{\Psi}_f(t) | \, \hat{V}_{\mathrm{A}} \, | \boldsymbol{\Psi}_i(t) \rangle \\ & - i \int_{-\infty}^{\infty} \mathrm{d}t \int_{t}^{\infty} \mathrm{d}t' \langle \boldsymbol{\Psi}_f(t) | \, \hat{V}_{\mathrm{A}} G_x(t,t') \hat{V}_{\mathrm{A}} \, | \boldsymbol{\Psi}_i(t) \rangle \\ & + \ldots \end{aligned} \tag{2.140}$$

Obviously the similarity of Eq. (2.140) with Eq. (2.98) is remarkable but not coincidental as the interaction described in this section has a large similarity to the ionization process in terms of intermediate and final states and the interaction with the laser field and atomic potential. Only the initial state differs as here initially quasi-free electrons are discussed. After transition $t' \to t + \Delta t$ one can obtain:

$$\begin{aligned} S_{fi} = & -i \int_{-\infty}^{\infty} \mathrm{d}t \langle \boldsymbol{\Psi}_f(t) | \, \hat{V}_{\mathrm{A}} \, | \boldsymbol{\Psi}_i(t) \rangle \\ & - i \int_{-\infty}^{\infty} \mathrm{d}t \int_{0}^{\infty} \mathrm{d}\Delta t \int \mathrm{d}\boldsymbol{q} \langle \boldsymbol{\Psi}_f(t+\Delta t) | \, \hat{V}_{\mathrm{A}} \, | \boldsymbol{\Psi}_m(t+\Delta t) \rangle \, \langle \boldsymbol{\Psi}_m(t) | \, \hat{V}_{\mathrm{A}} \, | \boldsymbol{\Psi}_i(t) \rangle \\ & + \ldots \end{aligned} \tag{2.141}$$

The first part on the r.h.s. represents the scattering process of an electron on a potential and simultaneous interaction with the laser field, while the second part (and all further parts) represents rescattering, a process where the electron state transfers into one or several intermediate states, $|\boldsymbol{\Psi}_m(t)\rangle$, in-between two scattering events on the regarded potential. This rescattering effect is discussed elsewhere[44] but will be disregarded in the present work.

2.3.3. Inverse Bremsstrahlung in a strong electromagnetic field

The first part of the r.h.s. (i.e. the first order Born approximation of the scattering process) in Eq. (2.141) leads to the *Bunkin* and *Federov* description[108] of the inelastic scattering cross-section[112] in a harmonic laser field:

$$S_{fi}{}^{(1)} = -i \int_{-\infty}^{\infty} \mathrm{d}t \langle \boldsymbol{\Psi}_f(t)| \, \hat{V}_{\mathrm{int}} \, |\boldsymbol{\Psi}_i(t)\rangle \tag{2.142}$$

$$= \sum M_n \tag{2.143}$$

with

$$M_n \propto \widetilde{V}_{\mathrm{A}}(\boldsymbol{q}_n) \, \mathrm{J}_n \left(\frac{F}{\omega^2} \boldsymbol{q}_n \cdot \hat{\boldsymbol{\epsilon}}_{\mathrm{L}} \right) \delta \left(E_f - E_i - n\omega \right) \tag{2.144}$$

where again $\boldsymbol{q}_n = \boldsymbol{k}_f - \boldsymbol{k}_i$ is the connecting scattering vector, $\mathrm{J}_n(x)$ denotes the Bessel function of first kind and $\widetilde{V}_{\mathrm{A}}(\boldsymbol{q}_n)$ denotes the fourier-transformed atomic potential. Due to the harmonic-field approximation the final state spectrum is discrete with corresponding energies separated by the laser frequency ω. However, in contrast to ATI not only absorption ($n > 0$, also in this context referred to as *inverse Bremsstrahlung*[113]) but also emission ($n < 0$) of photons by the active electron upon scattering can occur. Here it is noteworthy that $\mathrm{J}_n^2(x) = \mathrm{J}_{-n}^2(x)$ and, thus, for $n \to 0$ absorption and emission yield essentially the same cross-section $|M_n|^2$. However, it was shown that for slow electrons the mean energy gain per scatter event is in average as large as $2\,\mathrm{U_P}$ and, thus, absorption dominates induced emission yielding an efficient heating of the electron cloud[114].

Kroll and *Watson*[109] further evaluated Eq. (2.144) in the soft-photon approximation ($\omega \ll 1$) and for higher orders of the Born approximation. Essentially it was shown that the inelastic scattering cross-section σ_n can be represented in terms of the elastic scattering cross-section σ in the absence of the laser field:

$$\frac{\mathrm{d}\sigma_n}{\mathrm{d}\Omega} = \frac{k_f}{k_i} \, \mathrm{J}_n^2 \left(\frac{F}{\omega^2} \boldsymbol{q}_n \cdot \hat{\boldsymbol{\epsilon}}_{\mathrm{L}} \right) \frac{\mathrm{d}\sigma_{\mathrm{el}}}{\mathrm{d}\Omega} \tag{2.145}$$

2.3.3.1. Saddle-point method

The integral in Eq. (2.141) can be evaluated after inserting Volkov states in the length gauge as initial and final states by using the saddle-point method. As such a scattering event is included of the HATI description (see Sec. 2.1.2) but does not include the ionization process and revisit conditions I and II (of Eq. (2.101)) the laser-assisted electron scattering (LAES) condition represents a simplified HATI condition. The saddle-point method requires that the time-derivative of a stationary saddle-point in the instant of scattering, t_1, has to be zero. This leads to the LAES energy conservation[111, 115, 116]:

$$[\boldsymbol{k}_i + \boldsymbol{A}(t_1)]^2 = [\boldsymbol{k}_f + \boldsymbol{A}(t_1)]^2 \tag{2.146}$$

2.3.3.2. Semiclassical trajectories

The saddle-point condition Eq. (2.146) can be evaluated by terms of semiclassical trajectory considerations. In contrast to the ATI and HATI saddle points Eq. (2.146) has real solutions for real times t_1. Indeed the treatment by complex trajectories is not necessary and real-time and real-orbit based theories (as in the SMM) can be used to qualitatively describe LAES [116].

2.3.3.2.1. Simple-man model In the harmonic field approximation ($\boldsymbol{A}(t) = A\cos\omega t\hat{\boldsymbol{\epsilon}_{\mathrm{L}}}$) the saddle-point equation yields a quadratic equation for the final momentum, $\boldsymbol{k}_f$:

$$\boldsymbol{k}_f = A\left(-\alpha \pm \sqrt{\alpha^2 + \gamma_i^2 + 2\beta\gamma_i}\right) \tag{2.147}$$

where

$$\alpha = \cos\omega t\cos\theta_f \tag{2.148}$$

$$\beta = \cos\omega t\cos\theta_i \tag{2.149}$$

$$\gamma_i = \frac{\boldsymbol{k}_i}{A} \tag{2.150}$$

resulting in the energy gain ΔT and final kinetic energy T:

$$\Delta T = n_{\mathrm{LAES}}\omega = 4\mathrm{U_P}\left(\alpha^2 + \beta\gamma_i \pm \alpha\sqrt{\alpha^2 + 2\beta\gamma_i + \gamma_i^2}\right) \tag{2.151}$$

$$T = \boldsymbol{k}_f^2/2 = 4\mathrm{U_P}\left(\alpha^2 + \beta\gamma_i + \frac{\gamma_i^2}{2} \pm \alpha\sqrt{\alpha^2 + 2\beta\gamma_i + \gamma_i^2}\right) \tag{2.152}$$

Thus, the final yield w_f is:

$$w_f(\boldsymbol{k}_f, \theta_f) \propto \int_0^{2\pi} \mathrm{d}\omega t \int_0^{\infty} \mathrm{d}\boldsymbol{k}_i \delta\left(\frac{\boldsymbol{k}_f^2}{2} - T(\alpha, \beta, \gamma_i)\right) w_i(\boldsymbol{k}_i, \theta_i) \frac{\mathrm{d}\sigma_n(\boldsymbol{k}_i, \theta_i, \boldsymbol{k}_f, \theta_f)}{\mathrm{d}\Omega} \tag{2.153}$$

where w_i represents the initial electron momentum distribution and typically $w_i \to 0$ for large $\boldsymbol{k}_i$ and θ_i.

(2.154)

2.3.4. Incoherent scattering in the process of strong-field ionization

The first theoretical in-depth analysis of scattering events during the strong-field ionization of a dense atomic gas were performed by *Milošević* and *Čerkić* in 2006[42] extending the work on laser-assisted scattering[111, 115, 116] excluding the ionization process as it was discussed above. During the laser pulse an earlier released electron (e.g. by ATI) can revisit the parent atom and scatter coherently leading to coherent HATI or it can visit a neighboring atom and, thus, scatter incoherently leading to incoherent HATI (iHATI). The process is incoherent as the revisit condition (Eq. (2.101)II) is weakened in a dense Maxwell-distributed gas due to the non-uniquely defined the scattering time, t_1. It was

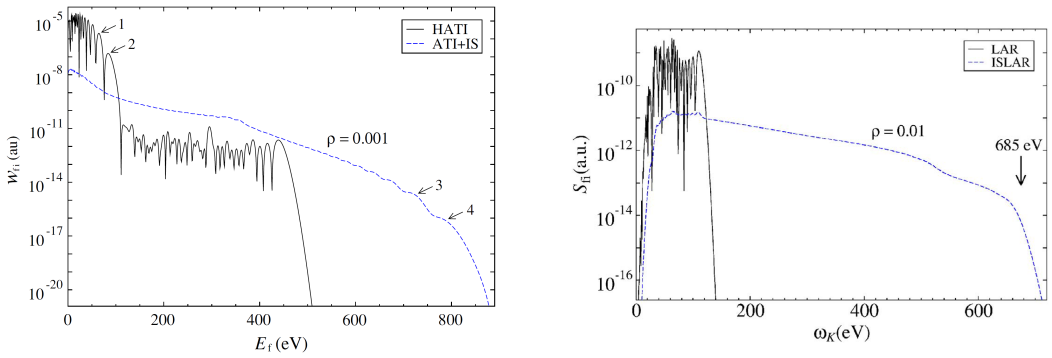

Figure 2.8.: Influence of electron scattering during the laser pulse. Left[42]: Contribution of incoherent HATI to the strong-field ionization yield in dense hydrogen gas. A clear violation of the semiclassical cut-off laws for the final kinetic energy is observable. Electrons with kinetic energies up to 20 U_P are produced and form a plateau-like structure. © IOP Publishing. Reproduced with permission. All rights reserved. Right[117]: Extension of the HHG cutoff limit above the semiclassical limit. Incoherent photoemission with significantly increased photon energy is observable. Reprinted figure with permission from [A. Čerkić and D. B. Milošević, Physical Review A, 75,013412 (2007)] Copyright (2007) by the American Physical Society.

shown (see Fig. 2.8) that the removal of the revisit condition yields a significant change in the final emission spectrum manifesting in an extension of the energy spectrum towards larger kinetic energies as well as larger emission angles. Additionally, a significant increase in photon emission induced by incoherent laser-assisted recombination (incoherent HHG) above the high-harmonic cutoff energy with respect to the coherent HHG emission was observed. Thus, incoherent scattering plays an important role in increasing final electron and photon energies above the semiclassical cut-off laws predicted by the SMM for HATI and HHG.

The iHATI emission can be interpreted in terms of the SMM by including the initial condition of the semiclassical ATI emission ($\gamma_i \leq 1$). The final kinetic energy of electrons emitted along the laser polarization axis ($\alpha = \cos\omega t$) is maximized for $\cos\omega t \to 1$ and initial emission along the laser polarization axis ($\cos\theta_i \to 1$):

$$T = 4U_P \left(\alpha^2 + \beta\gamma_i + \frac{\gamma_i^2}{2} \pm \alpha\sqrt{\alpha^2 + 2\beta\gamma_i + \gamma_i^2} \right) \tag{2.155}$$

$$\leq 4U_P \left(\frac{5}{2} \pm 2 \right) \tag{2.156}$$

$$\leq 18U_P \tag{2.157}$$

For an ordered target sample the revisit condition, however, can yield well-defined revisit times leading to coherent scattering. This consideration can be used to explain

coherent HATI emission in stretched molecules[26] where the same semiclassical cutoff value of $18\,U_P$ was observed. Thus, coherent HHG generation in structured materials as molecules, solids or clusters by laser-assisted recombination on neighboring scatter centers appears as a promising candidate for XUV emission above the semiclassical HHG cutoff.

3. Experimental Setup and Methods

3.1. Sources of laser radiation

3.1.1. Femtosecond Ti:Sapphire laser system

To study interaction of matter with strong external fields with laser peak intensities of the order of the atomic field ($I_0 \approx I_A$) need to be supplied. A monochromatic (continuous wave) light source would, thus, consume 1 PW in order to provide such experimental conditions. This issue is resolved by applying short laser pulses with moderate repetition rates and, thus, low average power and high peak intensities typically of the order of 10^{13} to $10^{16}\,\mathrm{W\,cm^{-2}}$. Another advantage of the application of ultrashort pulses is the disentanglement of electron and nuclear responses on the laser pulse which then enables the use of the Born-Oppenheimer approximation.

In this work such pulses are obtained from a multistage Titanium-Sapphire (Ti:Sa) laser system. In the oscillator[118] pulses with a central wavelength of 800 nm and pulse duration of typically below 25 fs are produced by mode-locked lasing in a titanium-doped sapphire crystal which provides a large emission bandwidth. Due to the non-linear response of the crystal in the laser cavity Kerr-lensing emphasis production of the broadband ultrashort laser pulses with a repetition rate of 80 MHz. A detailed explanation of the mode-locking and other techniques to produce ultrashort pulses can be found elsewhere[119].

In the second stage these pulses (seed) are amplified by chirped-pulse amplification (CPA). To avoid damaging of the optics in the amplifier the pulses are deliberately stretched and each frequency component amplified in another set of titanium-doped sapphire crystals which are pumped by a Q-Switched Neodymium-doped yttrium lithium fluoride laser[120]. The amplification is split into two parts - a multi-pass pre-amplification and a final single-pass amplification where the crystals are regeneratively pumped by the green pump laser representing a regenerative amplification process[121]. Due to the absorption and emission profile of these crystals frequency shaping before amplification is required to optimize the pulse shape in the frequency domain (Gaussian shape) after the amplification. Typically the central emission band of the seed pulse is, thus, damped to avoid overemphasis and, consequently, gain narrowing[122]. After passing the amplification stages the stretched pulse is compressed by a set of gratings producing pulses close to the Fourier limit. The amplifier produces pulses with pulse energy of

approximately 2.5 mJ with a pulse duration of 25 fs at a repetition rate of 5 kHz.

The Ti:Sa system is used to pump two additional stages to produce laser light of the desired wavelength: The optical parametric amplifier (OPA) is used to produce pulses with central wavelength in the near-infrared light (NIR) range and a high-harmonic setup is used to obtain extreme ultraviolett (XUV) light.

3.1.2. Optical parametric amplifier

Optical parametric amplification is a process where a fundamental beam (pump) is split into two wave components (signal and idler) while being overlapped in a non-linear crystal with a seeding beam (determining the wavelength of signal and idler) if the phase matching condition is met.

3.1.2.1. Optical parametric amplification

Considering a superposition of two waves of frequency $\omega_{1,2}$ the plane wave expression of the electric field component follows as:

$$E_i(\omega_i) = E_i \exp(-i\omega_i t) + E_i^* \exp(-i\omega_i t) \tag{3.1}$$

and the response of the polarizability in the medium is up to the second order:

$$P(E) = \epsilon_0 \left(\chi^{(1)} E + \chi^{(2)} E^2 + \dots\right) \tag{3.2}$$

$$= P^{(1)}(E) + P^{(2)}(E) + \dots \tag{3.3}$$

where $\chi^{(1)}$ and $\chi^{(2)}$ represent the linear and (second order) nonlinear susceptibility, respectively. The superimposed electric field follows as:

$$E(\omega_1 + \omega_2) = E_1(\omega_1) + E_2(\omega_2) \tag{3.4}$$

and, thus, the second order response of the polarizability reads:

$$\begin{aligned} P^{(2)}(E) = \epsilon_0 \Big[& \left(E_1^2 \exp(-i(2\omega_1)t) + E_1^{*2} \exp(-i(2\omega_1)t)\right) + \\ & \left(E_2^2 \exp(-i(2\omega_2)t) + E_2^{*2} \exp(-i(2\omega_2)t)\right) + \\ & (2E_1E_2 \exp(-i(\omega_1+\omega_2)t) + E_1^*E_2^* \exp(-i(\omega_1+\omega_2)t)) + \\ & (2E_1E_2^* \exp(-i(\omega_1-\omega_2)t) + E_1^*E_2 \exp(-i(\omega_1-\omega_2)t)) + \\ & E_1E_1^* + E_2E_2^* \Big] \end{aligned} \tag{3.5}$$

here the first two lines represent second harmonic generation of each incoming pulse, the third and forth line denote sum and difference frequency generation (DFG), respectively. For the OPA the DFG process is of main importance.

The efficiency of this process is highly determined by the energy and momentum

conservation (phase matching) with respect to the idler frequency ω_3:

$$\omega_3 = \omega_1 - \omega_2 \tag{3.6}$$

$$0 = \boldsymbol{k}_1 - \boldsymbol{k}_2 - \boldsymbol{k}_3 \tag{3.7}$$

In the case of a one-dimensional (collinear) beam layout this equation can be expressed in terms of the modulus of the wave vector. Rewriting this expression using the dispersion relation one reads:

$$0 = (n(\omega_1)\omega_1 - n(\omega_2)\omega_2 - n(\omega_3)\omega_3)/c \tag{3.8}$$

which is practically never satisfied in ordinary materials due to the linear frequency of the refractive index $n(\omega)$.

(3.9)

To satisfy the phase matching conditions birefringent materials are used to increase the efficiency of the DFG process which, additionally, affects the polarization of the outgoing beams. In the used OPA system[123] beta barium borate (BBO) is used for the amplification. To enable phase matching in a birefringent crystal the orientation of the crystal axis needs to be adjusted with respect to the incoming beam polarization.

3.1.2.2. White light generation

The OPA process, however, additionally needs to be seeded with the selected signal wavelength. To provide a large range of available output (signal or idler) wavelengths a continuous (polychromatic) light source is favorable. In the present setup the seed is obtained from a white light generation (WLG) process. A more in-depth discussion about WLG can be found elsewhere (e.g. [124, 119]). In general an isotropic medium (e.g. Sapphire) is used to omit second-order effects as shown in Eq. (3.5) and illuminated with sufficient intense laser pulses to increase the efficiency of third-order effects. In this case the non-linear refractive index becomes linearly dependent on the laser intensity. After illuminating the crystal with a pulse of a transverse non-constant intensity profile the beam gets focused (self-focusing) until compensating effects stabilize the beam profile (self-trapping). The high intensity of the trapped pulse induces self-phase modulation where the phase of the plane wave laser beam is non-linearly affected by the (time-dependent) intensity profile. Accordingly, a frequency shift proportional to the time-derivative of the refractive index[125] induces a symmetric blue(red)-shift in the trailing (leading) edge of the pulse. These are often referred to as anti-Stokes (Stokes) shifts and lead to a broadening of the spectral width. The anti-Stokes shift generally produces a broader plateau structure which can be explained by self-steepening of the pulse while the light travels through the medium.[124]

In the present setup the Stokes shifted part of the white light spectrum is used to seed the DFG of the OPA process. Due to the phase matching condition only a small part of

the white light spectrum is, however, amplified and can generally be adjusted by rotating the OPA crystal.

3.1.3. High-harmonic generation

The high harmonic generation (HHG) is typically defined as a process where photon up-conversion is realized in the non-perturbative high-intensity regime to produce wavelengths in the XUV to soft X-ray range. High-harmonic generation in noble gas targets is a competing effect to the high-order above threshold ionization (ATI) (HATI) process as discussed in Sec. 2.1.2 and follows a similar semiclassical description[126]: The target atom is initially neutral and the only active electron bound in the short-range potential due to Coulomb interaction with the nucleus. The outer electric field component of the laser pulse then perturbs the atomic potential in a way that an electron can tunnel through the resulting potential barrier into continuum states. The laser field then accelerates the electron, which can return to the parent atom when the revisit condition is fulfilled (see Sec. 2.1.2). During the revisit the electron can either scatter on the parental potential (HATI) or recombine with the parental ion releasing its excess energy by photonemission. Due to the odd (isotropic) symmetry of the target gas and energy as well as momentum conservation of the process only odd harmonics of the fundamental frequency will be efficiently produced.

High-harmonic generation is one of a few possibilities to generate XUV or soft X-ray light (others are synchrotron radiation, free electron laser sources, gas-discharge lamps and plasma emission), however, provides so far technically the best temporal resolution for single and multi-pulse experiments.

A more in-depth discussion of the HHG setup and its performance was discussed elsewhere[23].

3.1.4. Beam propagation

After generation both laser types (NIR and XUV) need to be transferred to the experiment. While the HHG beam needs to propagate through vacuum and refocused into the experimental chamber the OPA beam was further manipulated: For two-color pump-probe experiments additionally an adjustable delay between both pulses is implemented by the use of movable mirrors on a long-range translation stage (30 cm$\hat{=}$1 ns). For polarization dependent single color experiments wave plates (quarter and half wave retardation) where used to adjust laser polarization axis and ellipticity of the beam. In both cases laser attenuation was controlled by a set of half-wave plate and a polychromatic polarizer (Glan prism). Long-term laser intensity fluctuations and average power where recorded by beam reflections on a photo-diode after the attenuation. After preparation of the OPA beam the laser was focused by a spherical lens into the experimental chamber. The alignment of the focus inside the chamber was controlled via positioning of the lens

which was mounted on a motorized 3D translation stage. The width of the laser focus in front of the spectrometer was of the order of 20 µm to 40 µm.

3.2. Electron detection

3.2.1. Electron time of flight spectroscopy

Typically two approaches are employed to acquire free electron kinetic energies. Either one records the deflected trajectory in an a priori known electromagnetic field configuration (e.g. hemispherical analyzer, velocity map imaging, electron retardation) or the flight time over a known travel distance (time of flight spectroscopy). A more in-depth discussion on photoelectron spectroscopy can be found elsewhere[127, 128]. In both cases the electron kinetic energy is affecting the results of the measurement and, thus, a reconstruction of the original spectrum can be achieved. Each spectrometer type has its own advantages and disadvantages, however, electron time-of-flight spectroscopy appears optimal under given conditions and satisfies the requirements of a large range of recordable kinetic energies combined with a sufficiently small energy resolution, and, in combination with a weak electromagnetic deflection field, shows a sufficient large detection efficiency. In modern strong-field experiments velocity map imaging is often used[129, 130, 131] as it allows to detect electrons and ions (even in coincidence) with a very large detection efficiency (up to 100 %)[132]. However, this method is often restricted in the dynamic energy range due to its strong resolution dependency on the electron momentum and typically requires better vacuum conditions than a time-of-flight spectrometer due to the small spectrometer size and strong electrostatic fields[133]. For liquid samples as examined in this work a time-of-flight (TOF) spectrometer is preferred.

Considering an electron TOF spectrometer, the electron kinetic T can be derived from the electron arrival and departure instant, t and t_0, and travel distance, s:

$$T = m_\mathrm{e} c^2 (\gamma(v) - 1) \tag{3.10}$$

where $\gamma(v)$ represents the Lorentz-factor:

$$\gamma(v) = \left(1 - \frac{s}{(t - t_0)c}\right)^{-\frac{1}{2}} \tag{3.11}$$

and m_e and c represent the electron mass and vacuum speed of light, respectively. In the non-relativistic regime ($\gamma(v) \to 1$) this expression simplifies to:

$$T_{nr} = \frac{1}{2}\left(\frac{s}{(t - t_0)}\right)^2 \tag{3.12}$$

and the corresponding errors can be retrieved as:

$$\Delta T = c^3 m_e s \sqrt{\frac{(s^2\left((\Delta t)^2 + (\Delta t_0)^2\right) + (\Delta s)^2 (t-t_0)^2)}{(c(t-t_0)+s)^3 (c(t-t_0)-s)^3}} \tag{3.13}$$

$$\Delta T_{nr} = \frac{m_e s \sqrt{s^2\left((\Delta t)^2 + (\Delta t_0)^2\right) + (\Delta s)^2 (t-t_0)^2}}{(t-t_0)^3} \tag{3.14}$$

though typically $\Delta t \ll \Delta t_0$ for technical reasons (as discussed in Sec. 3.2.3).

(3.15)

In a normal drift tube configuration the energy resolution is mostly defined by the length of the spectrometer and the time resolution of the detection. For a drift length of 1 m and a time resolution of 0.3 ns for the arrival and 3 ns departure time as in the current experiment the relative energy resolution, $\Delta T/T$, is below 10 % up to electron kinetic energies of 1 keV. At the same time relativistic corrections as described above are insignificant. The uncertainty in travel distance, Δs, only yields significant contributions to Eq. (3.14) for low kinetic energies below 1 eV. Drift tube operation, however, has a large drawback due to the very small detection efficiency (in the present case of about 10^{-4}[134]). This loss of electron signal can be compensated by applying static electromagnetic fields as discussed in two examples below which will be referred as spectrometer 1 (S1) and spectrometer 2 (S2).

The detected photoemission signal is, however, as well strongly correlated to the photon energy due to the energy dependent partial photoionization cross section and asymmetry parameter[135, 136, 137] hampering comparison of photoemission spectra obtained with different photon sources. Knowledge of these values, however, allows to reconstruct the unaffected emission spectrum (as performed in [134]). Measuring in the so-called magic angle configuration allows to diminish photoionization asymmetry effects[127].

3.2.1.1. Magnetic-bottle time-of-flight spectrometer (S1)

In the magnetic-bottle TOF spectrometer an inhomogeneous magnetic field with rotational symmetry and strong gradient in the interaction region is employed. Initially undisturbed movement across magnetic field lines will lead to a spiral motion of electrons around those due to the Lorentz force[138]. By bending the magnetic field lines into the spectrometer and increasing the local magnetic field in the interaction region electrons with low momentum can be efficiently captured. The result of this kind of operation is discussed in detail elsewhere[139, 140, 134]. Summarizing, the electron kinetic energy as calculated in Eq. (3.12) remains approximately the same, however, due to the increase in acceptance of trajectories up to 30° the uncertainty in travel distance increases significantly as long as the kinetic energy is sufficiently large (large spiral radius) and the electron is still captured (see also Fig. 3.1). This reduction of energy resolution is dominating in the range of 20 eV to 100 eV with an increase of relative energy resolution, $\Delta T/T$, to approximately

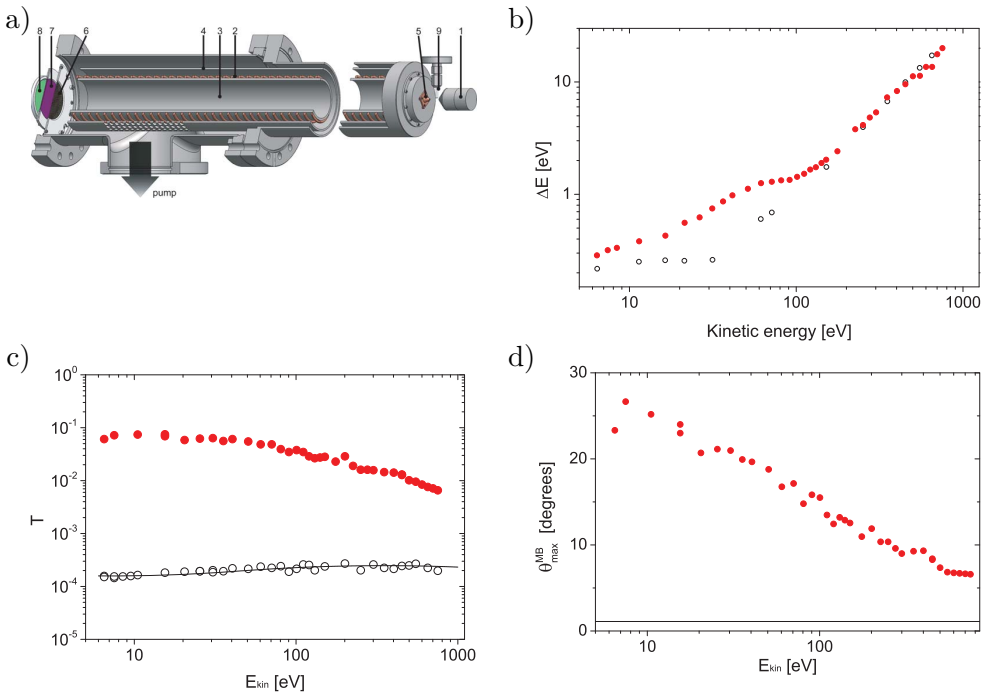

Figure 3.1.: Magnetic-bottle time-of-flight spectrometer: a) Design. The spectrometer consists of a drift tube (3) embraced by a long solenoid (2) and μ-metal shielding (4). Electrons in the interaction region will be bend into the spectrometer entrance (5) by a strong permanent magnet (1). Sample will be pushed into the interaction region by the use of the liquid microjet technique injecting a liquid filament through a nozzle (9) into the vacuum (as described in Sec. 3.3.1). The detector consists of a number of (biased) meshes (6), a stack of MCP's for signal amplification (7) and a phosphor screen (8) for electronic decoupling and visualization. b) Energy resolution as a function of kinetic energy. Open circles denote the field-free configuration while filled circles denote the change due to the superimposed magnetic field. For low kinetic energies the energy resolution is limited by the initial energy bandwidth of the electron and the uncertainty in travel distance. For larger values the flight time uncertainty becomes dominating. One can see that the magnetic bottle spectrometer decreases the overall energy resolution slightly. c) Detection efficiency (transmission) as a function of kinetic energy. Color scale is the same as in b). The strong increase in detection efficiency is observable. Mostly slow electrons can be bend by the magnetic field. d) Acceptance angle as a function of kinetic energy. A strong increase from approximately 1° to 30° for small kinetic energies is observable. Reprinted from Kothe et al.[134], with the permission of AIP Publishing.

5 %. However, the electron detection was shown to be improved up to 10^{-1} and, thus, by three orders of magnitude.

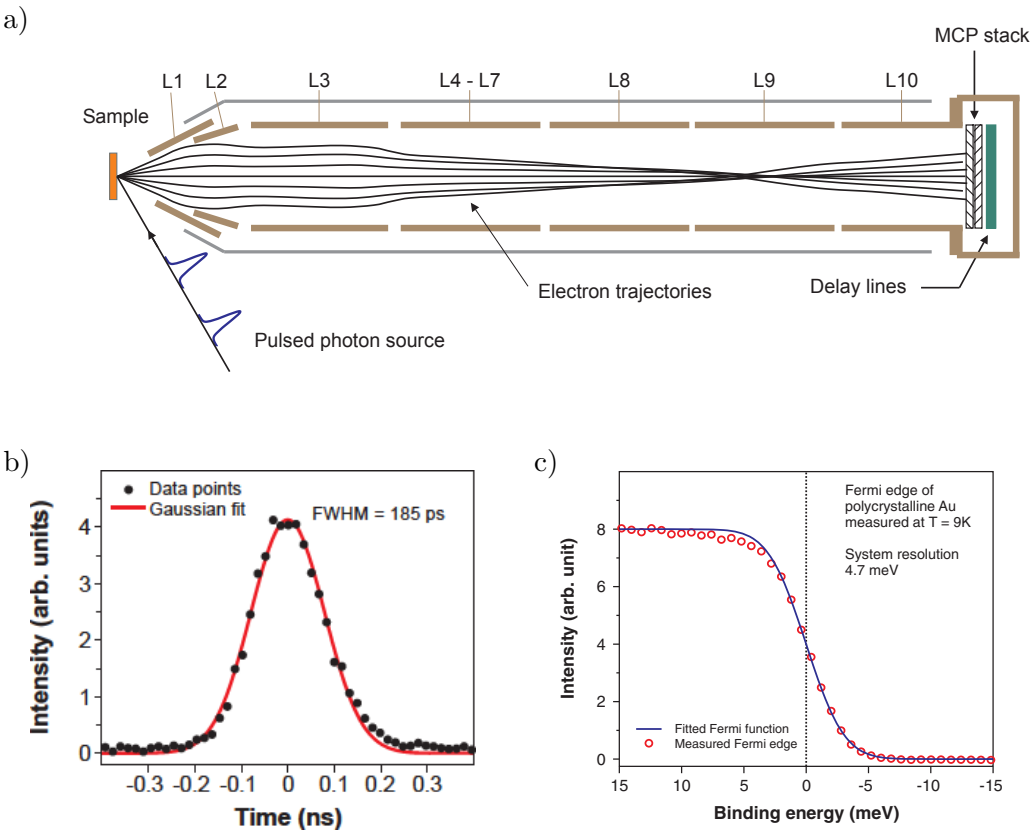

Figure 3.2.: Spectrometer Themis 1000 (similar to S2). a) Design of the drift tube including electric lenses (L1-L10) and typical electron trajectories of a monoenergetic electron cloud with deviating emission angle. By changing the potential of the lenses the focus can be adjusted. After amplification by a stack of MCPs the positioning and flight time are recorded by a delay line detector. b) Measured time resolution of the whole acquisition apparatus including broadening effects of the MCP, delay line detection and electronic amplification. c) Achievable energy resolution of the spectrometer. As the energy resolution is defined by the photon energy and adjustment of electric lenses the resolution can strongly vary in other experiments. Reprinted from Berntsen et al.[141], with the permission of AIP Publishing.

3.2.1.2. Time of flight spectrometer with electric lens configuration (S2)

Another possibility to increase the detection efficiency represents the superposition of static electric fields in an electric lens configuration. Such a device was recently developed[142] and is now commercially available[143]. A more in-depth analysis of the spectrometer and its performance can be found elsewhere[141] while here only a brief summary is provided.

A set of conducting flat surfaces with pair-wise opposing bias in the vacuum produces an electric field which forms an electric lens similar to a simple chromatic optical lens. A number of such lenses then produces an electron microscope which can be used to

retrieve electron origin and momentum by measuring the distance of the detected electron from the spectrometer symmetry axis and its flight time. In the case of spectroscopy the electric lenses are adjusted such that electrons will be focused within the spectrometer close to the detector and afterward defocused and mapped onto a stack of MCPs for amplification and further digital processing. As the focal point of an electric lens is depending on the electron momentum only a certain range of kinetic energies can be focused and, hence, correctly measured. Therefore, the spectrometer lens voltages are adjusted in such a way that a certain energy interval is detected while all other information is lost. The measurement interval around the central energy depends on the final electron momentum close to the detector (pass energy) and increases with increasing kinetic energy. However, as time-resolution is limited and large electron deflection leads to large aberration effects the resolution is significantly reduced for large pass energies. The electric lens configuration, however, allows to detect electrons in a much larger solid angle increasing the detection in the field-free case of 2° to 15° for a given central energy. By decreasing the pass energy the time resolution of the detection becomes insignificant whereby the energy resolution can be increased above the field-free case.

3.2.2. Electron detection and acquisition electronics

The first step of the electron detection in both setups is the amplification of the electron signal by an electron multiplier (in the current setup a microchannel plate (MCP)). Single-electron event counting is technically challenging, hence, preamplification of the single-electron event to an electron cloud is the preferred solution[144, 145]. The preamplification increases the signal but adds spatial broadening of the electron signal on the detector depending on the geometry and operation of the multiplier. In the case of the electronic lens spectrometer (S2) such a broadening reduces the energy and angle resolution. After preamplification the electron cloud is captured by an anode and the pulsed voltage change due to the electron impact on the anode recorded. In S1 a phosphor screen is used to record the electron impact and simultaneously emit light and, thus, visualize the electron detection. In S2 the electron impact position and instant are recorded by a delay line detector[146]. Typically, the anode has to be biased to several kV and the impact of the electron cloud is changing the potential by a few mV. The necessary decoupling of the AC (signal) and DC (bias) voltages is performed by a high-pass filter (see right panel of Fig. 3.3). As the time resolution of the detection strongly determines the energy resolution of the spectrometer a sufficient bandwidth needs to be supported by the whole apparatus[145]. This includes the MCP and anode as well as consequential amplification stages which in S1 is realized using the commercially available amplifier[147]. The time resolution can, thus, be estimated as approximately 0.2 ns to 0.3 ns. In the case of S2 the time resolution is approximately 0.2 ns[141]. To conserve the signal quality and to avoid reflections the impedance (50 Ω) of the whole acquisition line up to the

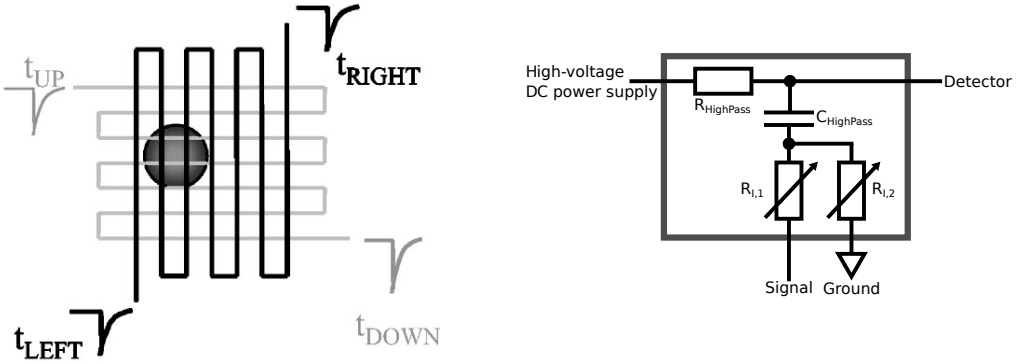

Figure 3.3.: Electron detection and decoupling. Left: Scheme of a delay line detector. The electron cloud hits the stack of delay lines at a certain position. The pulsed signal is transmitted along the delay line and will be detected (in both directions for each dimension) with a certain delay depending on the impact position. From delay and transmission velocity the exact positioning can be reconstructed. Reprinted from Da Costa et al.[150], with the permission of AIP Publishing. Right: Decoupling of weak AC signals from large potentials by an high-pass filter assembly. As the detector is typically operated current-free the high pass resistor can be large and the capacitor adjusted to the signal strength and impedance. Two additional variable resistors can be used to further help impedance matching.

analog-digital converter needs to be matched. In S1 the time-to-digital conversion was performed by the commercially available RoentDek fADC4[148] while in S2 the delay line detector Surface Concept SC-TDC-1000/02 D[149] was employed (see as well left panel of Fig. 3.3. A more in-depth discussion of time-to-digital conversion for the present application is presented below.

3.2.3. Time-to-digital conversion

To determine the electron kinetic energy electron arrival times need to be correlated to their destination time. The destination time is defined as the instant when the light interacts with the matter and is therefore the same for all arriving electrons within one shot. The time resolution of electronic circuits is of the order of hundreds of picoseconds up to several nanoseconds, thus, disregarding the ultrashort (tens of femtosecond) time envelope of the laser beam is reasonable. To determine the destination time t_0 and at the same time calibrate the spectrometer two methods can be applied. Either the photon arrival time t_p is measured taking the fixed travel time defined by the spectrometer length l and the speed of light c into account or known electron kinetic energies are recorded. The first method and its uncertainty Δt_0 are represented by:

$$t_0 = t_p - \frac{l}{c} \tag{3.16}$$

$$\Delta t_0 = \sqrt{(\Delta t_p)^2 + \left(\frac{\Delta l}{c}\right)^2} \tag{3.17}$$

where Δt_p and Δl represent the uncertainty in arrival time and travel length. Typically Δt_p is of the order of the width of the detector response function ($\approx 0.5\,\mathrm{ns}$) while $\Delta l/c$ is much smaller. However, the photon signal can be affected by the experimental conditions (e.g. excited samples can fluoresce with decay times of several nanoseconds, infrared light can not be detected, ultraviolet light reflected from other surfaces, ...) yielding a imprecise determination of the destination time using Eq. (3.16).

The second approach via known electron kinetic energies E_e and their arrival times t_e results in the calibration by:

$$t_0 = t_e - \sqrt{\frac{m_e}{2E_e}}l \tag{3.18}$$

$$\Delta t_0 = \sqrt{(\Delta t_e)^2 + \frac{m_e l^2 \Delta E_e^2}{8E_e^3} + \left(\frac{m_e \Delta l}{2E_e}\right)^2} \tag{3.19}$$

$$= \sqrt{(\Delta t_e)^2 + \frac{ml^2}{2E_e}\left(\frac{(\delta E_e)^2}{4} + (\delta l)^2\right)}, \tag{3.20}$$

where m_e is the mass of the electron, Δt_e and ΔE_e represent the absolute uncertainty in the arrival time and electron kinetic energy, respectively, while δE_e and δl denote relative uncertainties. One can directly see that for large kinetic energies the precision of Eq. (3.20) is limited by the detector response function as in the case of Eq. (3.16), however, for lower kinetic energies the uncertainty increases additionally depending on the relative error of energy and length. The main advantage of the second method, however, is the possibility to track different energy and arrival time pairs allowing to fit Eq. (3.18) which enables to decrease the uncertainty below the value of Δt_e with increasing sample size.

The time-to-digital conversion of electron flight times with precision of a few hundreds of picoseconds often yields rather high dead times of the detector after the first electron detection in the order of at least a few nanoseconds. In the current case this manifests in a loss of all occurring electron events after the first detected electron up to the end of the dead time. In the case of a sequence of electrons pairwise separated by less than the dead time only the first electron is detected while all others are omitted. To avoid such issues a sufficiently low event rate depending on the dead time and electron distribution needs to be provided.

3.3. Liquid jet and vacuum setup

3.3.1. Photoelectron spectroscopy of liquids

Photoelectron spectroscopy of liquids represents a key factor in understanding the structure and dynamics of functional materials (a more in-depth analysis can be found elsewhere[151]). However, photoelectron spectroscopy of dense systems is aggravated by the interaction of free electrons with the sample after the ionization process. Such interaction can result in elastic or inelastic scattering where latter can induce many secondary processes in the sample as sequential impact ionization, dissociation or other excitations. Most of these are not observable without electron sample interaction and highly affect the electron momentum spectrum effectively obliterating the information gain of the studied system. Hence, studying dense phase ionization always needs to incorporate separation of electron and sample after the ionization process.

The mean free travel distance also called electron attenuation length (EAL) in water is studied intensively in experiment[152, 153] and theory[154, 155, 156, 157] and a general theory of electron attenuation in liquids is in development. Fig. 3.4 shows the discrepancy of different results by theory and experiment in the range of small kinetic energies. The different indirect approaches to study the EAL leads to a strong variation in the result (relative experimental deviation is of the order of 3) from sub-nanometer (of the order of the distance between water molecules) up to several nanometer (the size of many water hydration shells). Understanding the motion of electrons in liquids plays a key role in understanding photoelectron spectroscopy of liquids.

Nevertheless, first spectra of liquids[158, 159, 160] and clusters[161, 162] where published decades after gas phase ionization studies[163] due to above mentioned limitations. The key to study high density targets was the development of sample injection into an vacuum (with sufficiently large EAL) in terms of gas nozzles and the liquid microjet technique (see Sec. 3.3.2).

Liquid phase spectra typically show a broadening and a shift of the emission bands[159]. The broadening is typically explained by the interaction of a single molecule with its non-homogeneous environment. As liquid structures are neither stable nor periodic emission from different molecules and, thus, averaging over the statistically distributed molecular environments leads to the aforementioned broadening. The shift, however, can be explained by the electric polarizability of the sample, Coulomb interaction due to the liquid-vacuum interface or interaction of molecular orbitals with neighboring orbitals (e.g. hydrogen bonding). The first one appears to be dominating under reasonable experimental conditions for water[159] and well reproduces the mean shift of all orbitals. The second origin plays an important role if the electrostatic potential landscape in the liquid gas interface shows strong modulation. Typical examples are streaming potentials of the jet[164] or dipole (multipole) electrostatic forces[165] e.g. due to surface orientation[166].

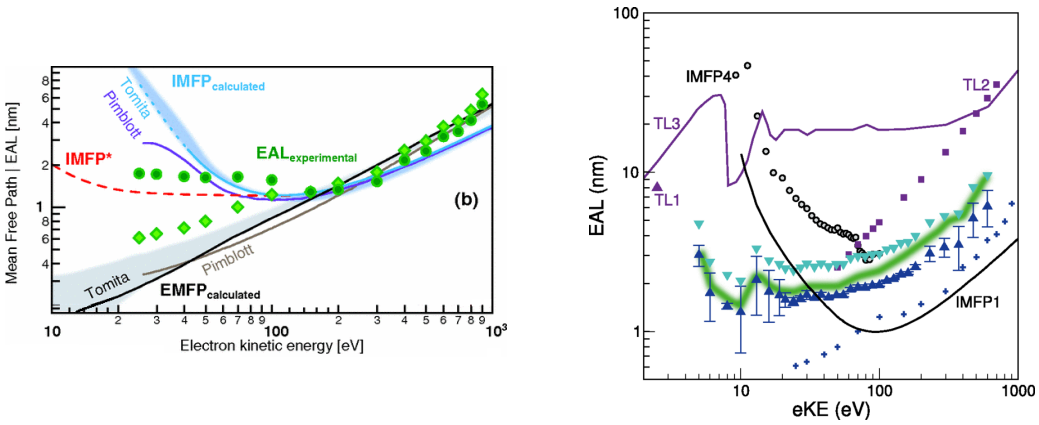

Figure 3.4.: Electron attenuation length as a function of electron kinetic energy. Left: Experimental (diamonds) and summary of theoretical results reported by Thürmer et al.[153] in the range of 20 eV to 1000 eV. While the predictions by theory are in well agreement with the experiment in the limit of large kinetic energies a strong deviation is observable in the low kinetic energy regime. While the theory predicts that the mean free path will increase with decreasing energy (equivalent to the case of solids) experimental results rather confirm that there is a plateau structure or even a further decrease of the EAL below 100 eV. Right: Experimental (triangles) and summary of theoretical results in the range of 20 eV to 1000 eV. Here the EAL shows a local minimum around 20 eV and an consequent increase for lower energies until the ionization potential of water at approximately 10 eV is approached and a resonance-like pattern appears. Reprinted figure with permission from [Suzuki et al.[152], Physical Review E, 90, 010302 (2014)] Copyright (2014) by the American Physical Society.

If streaming potentials are avoided the energy shift of liquid water due to these effects is rather low. The direct interaction of molecular orbitals with the neighboring ones and, thus, modulation of the orbital structure can lead to an orbital dependent shift and strongly depends on the localization of the orbital density.

3.3.2. Liquid microjet under vacuum conditions

As mentioned before, photoelectron spectroscopy of liquids requires tough experimental conditions. To increase the density gradient of the liquid-vacuum interface typically two approaches are considered. The first employs the insertion of a limiting solid surface into the interface, thus, adjusting the sample gradient to be step-wise. Such setups (e.g. a flow cell[167] or a window-separated chamber[168]), however, require to be transparent for incoming photons and outgoing electrons. As the EAL for electrons in solids for energies around 1 eV to 1000 eV is typically much smaller than 1 µm the separating window needs to be sufficiently thin but additionally stable enough to withstand several orders of magnitude pressure difference and light illumination. A recent and promising approach to satisfy these conditions are the invention of nanoporous single-layer graphene-coated

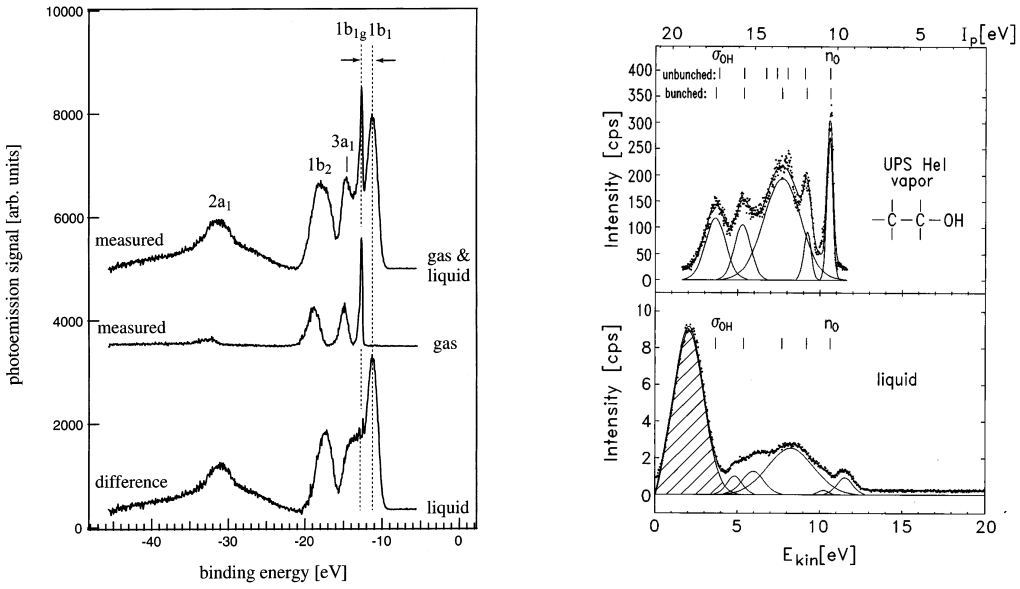

Figure 3.5.: Photoelectron spectrum of gaseous and liquid water and ethanol. Left: Valence spectrum of water in the liquid and gas phase. While the overall structure in gas and liquid phase resembles there a shift of all orbitals of around 1.45 eV is observable. Typically the liquid phase spectrum is broadened and vibrational substructures as in the gas phase are not observable. Reprinted (adapted) with permission from Winter et al.[159]. Copyright 2016 American Chemical Society. Right: Valence spectrum of ethanol in the liquid and gas phase. As in the case of liquid/gaseous water a shift and a broadening of the individual orbitals is observable. The mean energy shift of all shown valence orbitals is approximately 1 eV. Reprinted from Faubel et al.[158], with the permission of AIP Publishing.

flow-cells[169]. However, due to the laser beam damage by strong laser fields conduction of experiments will not be possible.

A second approach represents the microjet technique. Here the sample is directly injected into the vacuum and after passing through the interaction region extracted from the vacuum system either by differential pumping[170, 171] or by freezing the liquid[172, 158, 159] in the experimental chamber. Crucial for operation of such a jet is that molecules can evaporate and move out of the sample region without interaction. It was shown that the jet diameter has to be of the order of a few µm to satisfy unrestricted evaporation[173]. In that case the evaporation of molecules from the jet surface follows an undisturbed Maxwellian distribution[173] and the density of the sample decreases hyperbolically[174] such that a calibration of the gas sample pressure, ρ, as a function of the jet distance, R, can be written as:

$$\rho(R) = \frac{R_0}{R}\rho(R_0) \tag{3.21}$$

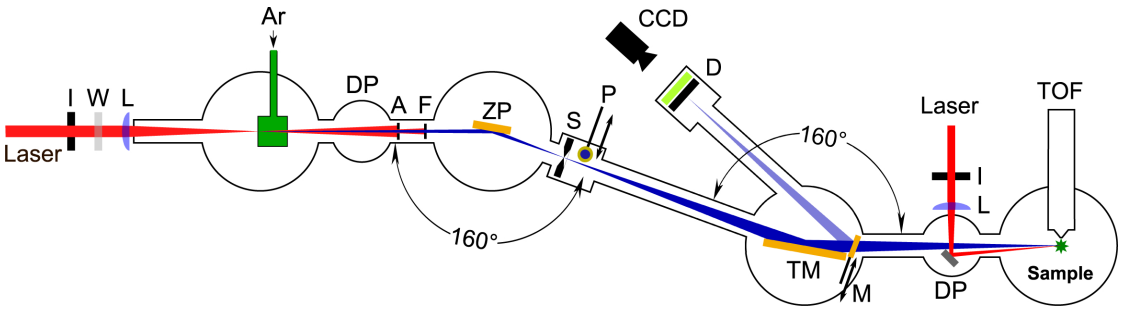

Figure 3.6.: Schematic view of the weak-field extreme-ultraviolet spectroscopy setup (E1). The infrared laser beam is send through an iris aperture (I), its polarization adjusted by a wave plate (W), and focused into the HHG cell by a spherical lens (L). To reduce reabsorption of high harmonic photons, a differential pumping stage (DP) separates the HHG and zone plate (ZP) vacuum chamber. The residual infrared beam is clipped by an aperture (A) and suppressed by an aluminum foil (F). One harmonic (17th, 21st, or 25th) can be selected by a slit (S) and will be focused into the experimental chamber by a toroidal mirror (TM) in front of the time-of-flight electron spectrometer (TOF, labeled S2 throughout this work; see Sec. 3.2.1.2 for more information). For analysis and calibration an additional movable photodiode (P) and a movable plane mirror (M) to observe the XUV photon beam on the position-sensitive detector (D) are installed.

where R_0 is the jet radius and $\rho(R_0)$ the gas density at the jet surface. This characteristic dependency is utilized in the density studies in Sec. 5.2 and Sec. 5.4.

The vapor pressure of a liquid strongly depends on the liquid temperature and evaporation of molecules from the jet in the vacuum-liquid interface leads to a cooling of the liquid[174, 175, 176]. Thus, the temperature and vapor pressure are not constant along the propagation of the liquid in the vacuum. In a distance of around one millimeter the liquid can cool down to approximately 0 °C, if injected at room temperature[164, 175].

3.3.3. Weak-field extreme-ultraviolet spectroscopy setup (E1)

The characterization of the experimental setup 1 (E1) is discussed in detail in Metje et al. 2014 *Opt. Express* **22** 10747-60 (Ref. [23]). It consists of a setup to generate XUV photons via HHG and employ these for transient photoelectron spectroscopy. The XUV light is generated by focusing laser pulses with a central wavelength at 800 nm and pulse durations of 25 fs into an argon gas cell. By the use of a zone plate monochromator and a postpositioned slit a specific (i.e. the 17th, 21st, or 25th) harmonic can be selected. After monochromatization the HHG pulses are focused into the experimental chamber in front of the electron spectrometer S2. The spectral width and the pulse duration of the XUV pulses are of the order of 0.3 eV and 50 fs, respectively. A schematic overview is shown in Fig. 3.6.

In the interaction region the XUV pulses are overlapped in time and space with the

pump beam to enable transient photoelectron spectroscopy (see Sec. 6.3.2 and Sec. 7 for results of this technique). The central wavelength of the pump beam can be chosen from the fundamental (800 nm corresponding to a photon energy of 1.55 nm) or 2nd, 3rd, and 4th harmonic of the fundamental frequency giving rise to a photon energy of 3.60 eV, 4.65 eV and 7.20 eV, respectively, or from a wide range (260 nm to 2000 nm) of supported frequencies obtained from an OPA [123] (see Sec. 3.1.2). The delay between pump and probe pulses is adjusted by a motorized linear stage spanning a maximal delay range of 3 ns with an accuracy of less than 2 fs.

To enable liquid photoelectron spectroscopy, a number of turbomolecular and cryogenic pumps are installed in the time-of-flight spectrometer and the experimental setup (often referred to as "endstation") containing the interaction region. Evaporation from the liquid filament is significantly reduces by freezing the liquid after leaving the interaction region in an cryogenic adsorption pump (denoted as liquid trap throughout this work). The main principle of the realization of liquid spectroscopy under vacuum conditions can be found elsewhere[177].

3.3.4. Strong-field near-infrared spectroscopy setup (E2)

The experimental setup 2 (E2) was developed to access higher accuracy in the determination of collective effects during strong-field ionization of dense gas targets (see Sec. 5.4) than the previously used setup E1 (see Sec. 5.2) were three main obstacles restricted the accuracy of data acquisition: (i) The residual gas pressure by employing a liquid microjet of acetone (of approximately 1×10^{-4} mbar to 1×10^{-3} mbar) does not facilitate unperturbed photoelectron detection, (ii) liquid jet and laser beam pointing stability led to significant uncertainties in the distance between the laser beam and the jet center, (iii) data acquisition was restricted to long integration times and included preprocessing of acquired data, limiting the data evaluation.

The endstation of E2 resembles the one of the E1 and follows the same operation principle as described elsewhere[177]: Liquid photoelectron spectroscopy is realized by injecting the liquid sample into the vacuum and consequently freezing it after the passage through the interaction region by the use of an cryogenic adsorption pump. To further decrease the gas pressure in the chamber containing the interaction region and the spectrometer, turbomolecular and cryogenic pumps were attached. Depending on the target sample (e.g. water, ethanol, or acetone) a residual pressure of approximately 1×10^{-6} mbar to 1×10^{-5} mbar was achieved enabling unperturbed movement of photoelectrons into the electron time-of-flight spectrometer (labeled as S1 throughout this work; see Sec. 3.2.1.1 for more information). This improvement over E1 was achieved by reducing the distance between laser jet and cryogenic pumps and increasing the total surface and volume of the attached liquid trap.

The liquid jet stability was improved by a commercially available pulsation-free high-

precision syringe pump[178]. Additionally the supporting frame of the end station was stiffened and vibrations induced by the vacuum prepumping system were mechanically decoupled. The laser beam pointing was controlled via motorized linear high-precision translation stages and all optics mounted on high-stability mounts[179]. Laser beam diagnostics to determine the pointing stability, focus size, and quality of the laser beam profile of the near-infrared beam are employed by the use of a razor blade mounted on a motorized translation stage.

A more in-depth description of the design and characterization process of a setup for photoelectron spectroscopy on liquids can be found elsewhere[180].

Finally, a modular data acquisition program enabling high repetition rate measurements (1 Hz to 1000 Hz) was developed (see Sec. 4).

4. Development of a Modular Event-Based Acquisition Program

A modular event-based acquisition program was developed to support fast acquisition procedures. It consists of three components: (i) a device control unit to operate a large number of independent devices in parallel, (ii) a data view unit to observe experimental conditions on the fly as well as to do single- and multi-pass data analysis, and (iii) a data bundle and compression tool to reduce the unnecessary data load due to the event-based acquisition design.

The program was written using the object-oriented programming language C# and is based on the Windows Forms GUI framework. As most operations are employed on objects as devices, acquisitions routines, and datasets an object-oriented approach appears natural and supports extensibility and operational stability (by encapsulation). This approach is realized by abstraction and inheritance of the required structures and operations into generic classes.

As all devices and measurements are operating in parallel the acquisition software is based on multi-threading operation.

The concept of the implementation is only briefly discussed in the following sections and does not represent a manual for the operation or further development of the program.

4.1. Device control unit

The device control unit has two main tasks. First, it needs to control (i.e. manipulate and readout) all connected devices and, furthermore, requires the ability to acquire data as a function of the device settings. The latter is realized by allowing dynamic sampling of certain device parameters (e.g. sampling of a voltage or a motor position) and, hence, creating a queue of jobs (job list) that needs to be processed.

4.1.1. Device handler

The device handler overviews all installed devices. Installation of a device requires the connection of the device to the measurement PC and inclusion of the corresponding `*.dll` into the device loading routine. If a module stops responding or is otherwise out of function, the device handler is responsible to restore the device without the need to restart the whole program. Thus, the thread-management of each device needs to be

highly encapsulated and no direct communication between devices or from a devices to other processes (as the main process) is tolerated (see Sec. 4.4.3).

4.1.1.1. Devices

Abstraction, interfaces and inheritance are the main concepts to generalize the communication with devices. The abstract base class (thus, a non-instantiable class) supports the readout routine of each parameter and setting a certain device has implemented (see Sec. 4.1.1.1.1). Here, a parameter is defined as an observable of an experiment that can either be read out (dependent entity; e.g. a photodiode signal) or manipulated (independent entity; e.g. a motor position) in order to sample an experimental condition (see Sec. 4.1.1.2). On the other hand, a setting is a quasi-static condition required for the communication with a device (e.g. an IP-address, serial port) and, thus, can be adjusted during the operation but will not be sampled or saved in order to perform an experiment (see Sec. 4.1.1.3).

Another abstraction layer builds upon the abstract base class enabling to generalize communication using specific communication designs or protocols (e.g. TCP/IP devices, RS232/COM devices)

4.1.1.1.1. Abstract device base class The abstract device base class has a number of generalized tasks common for the communication with devices. It handles the graphical user interface (GUI) of an device showing and allowing to adjust all parameters and settings. The GUI is updated by an encapsulated timer (see Sec. 4.4.3.1 for more information) with a fixed refresh rate of 10 Hz. The updating thread reads all available data from the parameter cache and updates the shown values accordingly.

Another encapsulated timer handles one (if existent) user input (manipulation of settings or parameters) and all read out routines specified by the device per timer event. Manipulation is handled in a separate encapsulated background thread (see Sec. 4.4.3.2 for more information), such that user input does not interfere with the readout of the device status. The readout time of a device can be dynamically specified by a setting and typically is limited by the hardware response time (i.e. rates of around 10 Hz to 100 Hz for TCP/IP and USB devices and 1 Hz to 10 Hz for RS232/COM devices are possible).

The abstract base class handles the device-specific garbage collection and freeing of resources and saves all settings permanently while discarding cached parameter values upon shutdown.

All the following classes are derived from the abstract device base class and, thus, due to inheritance provide the before-mentioned properties and structures.

4.1.1.1.2. TCP/IP device class The abstract TCP/IP device class supports communication via TCP/IP. Upon initialization it connects the device to the specified LAN port

and opens a number of communication threads if the device supports multi-threaded communication. All parameters of the TCP/IP communication (IP address, Port, number of communication threads) are adjustable as settings. This class provides one-way communication (Write, Read) and two-way communication (Write and Read) to the specific device child class.

4.1.1.1.3. RS232/COM device class The abstract RS232/COM device class supports communication via the RS232/COM protocol. It supports asynchronous and synchronous communication with the specified port, depending on the communication protocol of the device. All RS232/COM parameters (as COM port, baud rate, parity) are adjustable as settings. This abstract class provides one-way (single-character read/write and multi-character read/write) as well as two-way communication (multi-character write and read).

4.1.1.1.4. IPC device class The abstract IPC device class supports communication via a generic inter-process communication (IPC) protocol (see Sec. 4.4.2). The exact implementation of the IPC routine as well as the one-way and the two-way communication protocol is hidden to the device. The IPC device can be used if different components within the same device control unit (e.g. software devices as software-implemented lock-in amplification or PID-controller) or components of different control units (e.g. remote control) have to communicate.

4.1.1.1.5. Named pipe device class The abstract named pipe device class supports communication via a specific IPC protocol (named pipe protocol). This implementation can be used if the connected device explicitly uses a named pipe to communicate with the device control unit. The communication protocol is handled by the child device class and this abstract class only provides the necessary handles to read and write via a specified named pipe.

4.1.1.1.6. Local store device class The abstract local store device class provides a saving routine for all parameters. Instead of discarding parameters upon shutdown and only saving the device settings all values of parameters are saved to disk and reloaded upon initialization. Quasi-static information that is required to be saved to the acquisition (e.g. project name, sample name) can be controlled using this class. Typically, such information would be stored as device setting instead but due to its importance for the experiment is treated as parameter.

4.1.1.1.7. Dynamic device class The abstract dynamic device class allows to dynamically adjust the number and implementation of a specific parameter. The design of a

dynamic device is, thus, fluid and depends on the operational condition of the experimental apparatus. The dynamical adjustment is handled by the specific implementation of the child device class.

4.1.1.2. Device parameter

Each device contains a number of `Parameter`s. These typically represent observables of an experiment (e.g. motor position or photodiode signal). The parameters support a two-dimensional structure to support multi-axis or multi-stage devices. Each parameter contains a name, a value (see Sec. 4.4.1), and a manipulation and readout routine to update the value. These routines needs to be explicitly specified by the device. If a parameter does not provide a readout routine (e.g. a calibration/homing procedure) or a manipulation routine (e.g. a readout parameter) they need to be specified as such. Accordingly, the GUI of the device and the update routine in the abstract base class will be adjusted to reflect this condition. Separately, the appearance of these parameters on the GUI can be adjusted in the device implementation. The value of a parameter can be saved to file and/or network stream as specified but will be discarded upon shutdown. There are two different ways to read out a parameter: Either one reads a cached version (`Peek`) of the last readout or one `Retrieve`s all cached values from the parameter which will empty the cache. Emptying of the cache is only recommended for saving routines and yield a warning otherwise.

4.1.1.3. Device setting

Device `Setting`s represent a quasi-static value (see Sec. 4.4.1) that is required for the correct operation of a device. These settings are saved to disk upon shutdown and, accordingly, restored during the boot process of the program. Settings are not saved to disk for a specific measurement and outdated values are not cached.

4.1.2. Acquisition sampler

The acquisition sampler allows to specify a multi-dimensional acquisition and add it to the job list (see Sec. 4.1.3). The sampled value range for each parameter can be given by a comma-separated list of elements which is either a single value or a colon-separated value range of the form `start:end:resolution`. Thus, a sample value of `0,1,2:6:2,6:10:4` samples the positions `0,1,2,4,6,6,10`. Each of these positions is referred to as `Measurement`. If more than one parameter is specified all combinations of the two single dimensional parameter space are sampled. E.g. if one device is set to sample `0:4:2` and a second device is set to sample `0:10:5` all combinations `{0,0},{0,5},{0,10},{2,0},{2,5},{2,10},{4,0},{4,5},{4,10}` are sampled where the first (second) number denotes the setting of the first (second) device.

All these `Measurement`s together represent a `Series`. Hence, each addition of a multi-dimensional acquisition yields a new `Series`. Each `Series` is saved in its own file and, thus, consists of a number of samples. All `Measurement`s within the same `Series` share the series name and integration time and can be repeated several times as specified.

4.1.3. Job list

The job list represents a queue of series. When the acquisition is started the job list starts the first non-finalized series. Within this series the first non-processed measurement is handled. This includes manipulating all devices according to the specified value, waiting for all devices to confirm execution and finalization, starting acquisition for the specified integration time, and finalizing the measurement by stopping the acquisition. After finalization of a measurement the next non-processed measurement is started. After processing of all measurements within a series, the series is finalized by releasing the file handle of the series and post-processing of the acquired data (see Sec. 4.3).

4.2. Data view unit

The Data view unit represents a simple data visualization and processing tool. It either represents the data as a two-dimensional graph or the latest obtained value. The data viewer can communicate with the control unit using the IPC interface (see Sec. 4.4.2) and, thus, allows to process and visualize the data with a short delay (≈100 ms to 500 ms).

4.3. Data shrink unit

The size of event-based data can be significantly large depending on the sample rate, integration time, and number of connected devices as no processing of data is applied. To reduce the file size of a given series without processing of data, redundant information (such as constant temperature or voltage readings) can be removed. Additionally the data will be compressed by the `gzip` algorithm.

4.4. Other generic components

4.4.1. Data value

Each data `Value` consists of a type (`Boolean`, `Date/Time/TimeSpan`, `Double/Float`, `Integer`, `String`), a precision or accuracy, and a value buffer consisting of a thread-safe first-in-first-out (FIFO) queue and a single cache for the latest value (peek value). Each time a value is updated, the newest value is added to the FIFO queue and the single cache value is assigned to the same value.

There are two operations to obtain the saved data. Either the data is `retrieved`, corresponding to the extraction, consumption, and emptying of the whole FIFO queue without update of the single cache, or the single cache value is `peeked` and the FIFO queue remains unaffected. Thus, retrieving of data is only allowed to those procedures that save the content of the queue. A warning is issued if another object tries to retrieve a value to avoid loss of data.

`Value`s can be collected in `SettingList`s representing the data set equivalent of a device. These setting lists can be bundled into `DataSet`s corresponding to a single event in the acquisition routine collecting all available data of all available devices (and, thus, is equivalent to the current state of the device handler).

`Coordinate`s represent the extension of data values allowing to do simple operations, as addition, subtraction, division, multiplication, concatenation, and counting. Additionally coordinates carry information about their (in-)dependency and data origin (device and parameter name). A vector of coordinates represents a `CoordinateGroup` (i.e. a single vector in the data evaluation and visualization).

4.4.2. Inter-process communication (IPC)

The included IPC interface allows communication between two different processes without exposing the underlying method. Currently a message system via named pipes is used. The message system consists of a multi-step communication protocol. First, the server opens a main stream where all clients can connect at any time. In the main stream the server only accepts requests for creation of a side stream. Before a client can request a side stream it has to validate itself by a simple password request. If the stream is verified/trusted the client can transmit the request for a side stream. The server, then, answers with the name of the newly created side stream, which name is a uniquely created globally unique identifier (GUID) of 16 characters. After receiving the name of the side stream the client leaves the main stream and joins the created side stream.

In the side stream a number of new operations is available which are: `Idle`, to keep the communication alive without requesting anything from the server, `GetAll`, to get all cached `DataSet`s available to the stream server, `Devices`, to obtain the names of all connected devices, `SetSetting`, to request the server to send a request to one of the connected devices to adjust a setting, although the device can decline, `SetCommand`, to request the server to send a request to one of the connected devices to adjust a parameter, although the device can decline, `CloseRequest`, to close the connection because the client is shutting down. It is not possible to request a new pipe in the side stream.

The communication always has the same scheme: (i) the client connects to the stream opened by the server, (ii) the client verifies the server (reads from the pipe), (iii) the client sends its own verification string to the server which verifies it, (iv) the client sends one of the above-mentioned request to the server, (v) the server either fulfills the request

or declines and issues an `OK` or `NotOK`, respectively, to the client.

If a close request is send either by the server or the client, both ensure that the other side is informed about the closing state, independent on the current status of communication.

4.4.3. Thread management

To ensure stability of the main process independent on the stability of a single device a thread management needs to be implemented providing encapsulation and long-term stability. In the present program two types of threads are used: encapsulated timers and encapsulated background threads which are presented below. Within an encapsulated thread all `catch`-able exceptions are caught and logged. Dependent on the thread the work is continued or aborted after handling of the exception. All threads need to register into the thread management with their name, their origin (invoking class), and supposed life time and are, thus, observable and controllable by the user.

4.4.3.1. Encapsulated timer

The encapsulated timer is not a real timer but rather a continuously running background thread with dynamic idle times between invocations of the corresponding method. Thus, there will never be two or more invocations of the same method at the same time. Encapsulated timer can always be paused, aborted, restarted, or their invocation interval/idle time adjusted. Additionally the amount of time used for the invoked method and the idling time is recorded to debug critical methods.

4.4.3.2. Encapsulated background thread

The encapsulated background thread is similar to the timer, however, invokes the corresponding method only once and, thus, no idle interval is defined. Accordingly, a background thread can not be paused but only aborted or restarted.

4.4.4. Event and message logging

All `catch`-able exceptions are caught within the thread management and corresponding error messages logged to a file and into a console in the main window. Additionally warnings and information issued by the components can be displayed.

4.4.5. File interfaces

A generic file interface was implemented to enable saving of data specified by the user. Typical formats of saved data are the two-dimensional formats as comma-separated values (CSV) and tab-separated values (TSV) files or higher dimensional formats as INI, hierarchical data format 5 (HDF5), and extensible markup language (XML) files.

Although all of these formats are reasonable choices only the XML interface was implemented. XML represents a natural choice to save objects consisting of attributes and other objects without prioritizing specific structures (contrary to the HDF5 format).

5. Results and Discussion on Ionization of a Dense Gas

This chapter is based on the publications Wilke *et al.* New J. Phys., **16**, 083032 (2014), doi:10.1088/1367-2630/16/8/083032 (Ref. [181]) and Wilke *et al.* Phys. Rev. A **94**, 033423 (2016), doi:10.1103/PhysRevA.94.033423 (Ref. [182]).

5.1. Introduction

Low density strong-field emission was comprehensively studied in atomic and small molecular systems where theoretical description of the emission was employed to interpret the recorded data. For higher density targets (such as clusters) macroscopic semi-empirical or semiclassical modeling is preferred, since calculations employing quantum-mechanical descriptions are essentially impossible because of computational restrictions. Therefore, there is a lack of an accurate theoretical description of strong-field ionization in dense media.

In this chapter, the theoretical interpretation is based on the step-wise consideration of a sequence of elementary processes, whereas each process is considered for an isolated molecule and can be described semiclassically or quantum-mechanically. In particular, the first step involves the electron emission from molecules in a strong field and the second step involves the scattering of the emitted electron on a neighboring molecule in the presence of the laser field. Of course, such a sequence is possible if the time interval between the two events is smaller than the laser pulse duration. Such a condition is fulfilled for sufficiently dense media. The here developed approach is applied to describe the laser interaction with a dense gas, but can also be extended for other types of media such as clusters or droplets.

Below we consider interaction of water and acetone molecules with a laser pulse of high peak intensity and short duration. So far, strong-field interaction of water molecules is sparsely studied, although interesting features are observable in the condensed phase: Water droplets can be used as a target for coherent high-harmonic generation as well as for the generation of incoherent plasma radiation, showing a dependency of the generated photon yield on the target density[54, 55]. In general, it was shown that the extreme ultraviolett (XUV) yield can be significantly enhanced by increasing the target density[183, 184]. However, ionization represents the major effect occurring in a strong

laser field. For moderate laser intensities of $5 \times 10^{13}\,\mathrm{W\,cm^{-2}}$, the laser beam filamentation in dense water vapor was observed, leading to subsequent amplified stimulated emission (ASE)[185]. In the same study it was shown that dissociation of water molecules plays an important role in the sample deexcitation and that multiple transitions can influence the absorption of water gas (e.g. HOMO or HOMO-1 excitation). However, it was shown in other studies that the strong-field ionization from single water molecules is dominated by the HOMO ionization and other ionization channels involving dissociation are barely observable within ultrashort laser pulses after averaging over all molecular orientations[186, 187, 188].

This chapter provides further new insight into the ionization process by addressing its coherent and incoherent channels associated with the first and second step, respectively, of the sequence of elementary processes. This study is focused on the electron emission at higher kinetic energies where the coherent and incoherent channels compete with each other.

5.2. Strong-field emission from water vapor

5.2.1. Experimental conditions

In this work the experimental setup experimental setup 1 (E1) was used in combination with the spectrometer spectrometer 1 (S1) (see Fig. 5.1(a)). The spectrometer was operated in the field-free mode with an acceptance angle of 1.1°. This value constitutes the angular resolution in the present experiment. Additionally, a low electron kinetic energy filter was applied to significantly reduce the load by low energy electrons ($\leq 60\,\mathrm{eV}$)

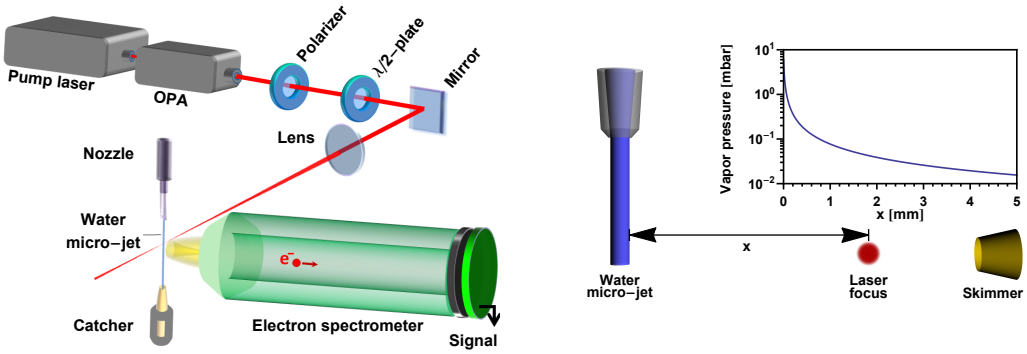

Figure 5.1.: Experimental setup[181]. Left: Schematic view of the laser beam preparation and propagation to the electron time-of-flight spectrometer. Right: Geometry of laser, liquid microjet and spectrometer in the interaction region. The density dependence on the distance between microjet and laser focus is shown in the inset assuming a water surface temperature of 0 °C close to the laser focus.

due to above threshold ionization (ATI).

Linearly polarized near-infrared laser pulses of 40 fs pulse duration and central wavelength of 1450 nm were focused by a spherical lens into the experimental chamber into a focal spot of approximately 25 µm. The pulse energy was attenuated to 40 µJ yielding a laser peak intensity of approximately $1.3 \times 10^{14}\,\mathrm{W\,cm^{-2}}$ and giving rise to the ponderomotive energy of 25.6 eV. The beam polarization axis was controlled with the use of a waveplate allowing angle-resolved measurements.

The target medium lies in the vicinity of a 20 µm water microjet where the evaporation of molecules from the liquid phase yields a well defined density gradient (see Sec. 3.3.2). By adjusting the distance between the laser focus and the jet surface, the density can be varied by orders of magnitude between the residual gas pressure in the chamber of approximately 1×10^{-5} mbar and the equilibrium vapor pressure of liquid water. At around 0 °C temperature, the equilibrium pressure can be estimated to be approximately 6 mbar (see Fig. 5.1(b)). Due to the uncertainty in the microjet temperature close to the laser focus, the exact absolute value of the vapor pressure at the jet surface is only roughly defined. However, the absolute density scale is not of importance for the interpretation of the data since the hyperbolic decrease of the gas density along the radial component due to radial diffusion allows to well specify the density dependence of the photoelectron emission. All relative density changes are, thus, accurate. A small concentration (20 mM) of NaCl was added to the purified water to avoid streaming potentials[164].

5.2.2. Interface study

This study focuses on the photoelectron emission at different water gas densities above the classical energy cutoff of the ATI process (i.e. at kinetic energies larger than approximately 50 eV). Only electrons after rescattering on the parent molecule will possess sufficient energy to be observable under the experimental conditions. The spectrum of these electrons exhibits the expected high-order ATI (HATI) features (a narrow electron cone around the polarization axis extending on the energy scale up to $10\,U_P$). Even though high sample densities might affect the final emission spectrum due to charging of the medium, such effects are of importance for electrons of low kinetic energies produced in the ATI process and do not significantly affect the fast electrons of the HATI emission. They decrease further with increasing kinetic energy. The effect of charging on the emission of photoelectrons ionized in strong laser fields under the given density conditions was studied elsewhere[189]. It was concluded that a slight angular broadening and changes in the energy distribution of electrons are only observable in the region up to $1\,U_P$.

A series of angle-resolved photoelectron spectra was recorded at 10 µm, 25 µm, 50 µm, 500 µm, 1000 µm and 1×10^3 µm distance with respect to the jet center yielding target pressures of 6 mbar, 3 mbar, 1.6 mbar, 0.2 mbar, 8×10^{-2} mbar and 8×10^{-3} mbar, respectively (as pointed out above, the uncertainty of these values lies withing a constant

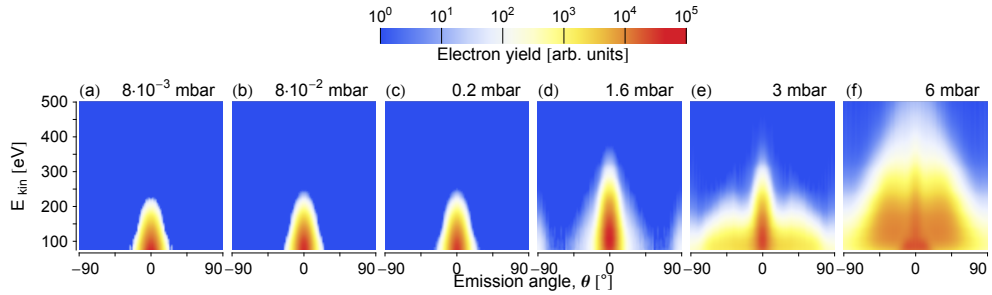

Figure 5.2.: Angle-resolved photoelectron emission spectrum of water gas in the vicinity of a liquid microjet[181]. The emission angle, θ is given with respect to the laser polarization axis where 0° denotes parallelism. The final kinetic energy, E_{kin}, is given in eV where $E_{\mathrm{kin}} = 10\,\mathrm{U_P} = 260\,\mathrm{eV}$ represents the semiclassical HATI cutoff energy. The spectra are obtained at different target pressures: (a) 8×10^{-3} mbar, (b) 8×10^{-2} mbar, (c) 0.2 mbar, (d) 1.6 mbar, (e) 3 mbar, (f) 6 mbar. To ease comparison the photoelectron signal in each spectrum was normalized to the target density.

factor close to unity depending on the jet temperature). The resulting spectra were normalized to the gas density and, hence, the photoelectron yield from the effects which are linearly dependent on the target density (such as ATI and HATI) should remain constant in the spectra. The recorded series of spectra is shown in Fig. 5.2. It is noteworthy that in the measurement at the density of 6 mbar, corresponding to the assumed vapor pressure at the surface, the laser beam partially overlaps with the liquid sample. Due to the higher number density in the liquid phase, one would, thus, expect that at this position (and possibly at others positions where the laser focus is centered close to the jet surface) the emission is dominated by photoelectrons from the liquid phase. However, one should also consider the penetration depth of electrons in water, called as electron attenuation length (EAL), which is shown to be of the order of the thickness of a single water layer (≈ 1 nm) at electron kinetic energies considered in this work (50 eV to 500 eV). Thus, even though more electrons are generated in the liquid phase, most of them will scatter in the liquid leading to secondary effects. Typically the interaction of incident electrons with a dense liquid sample leads to a decrease of the electron kinetic energy as well as to an increase of the isotropy of the scattered electrons from the liquid phase. If not recaptured by positive ions produced in the laser focus, the electrons ionized from the liquid phase will from a large isotropic secondary electron tail in the spectrum, which can be effectively blocked by the low-energy electron filter. Indeed, the amount of slow electrons upon illuminating the jet with strong laser pulses is sufficiently large to damage the detection and amplification devices of the spectrometer. This is the main factor for applying the low-energy electron filter and for choosing the specific threshold voltage. Hence, even though the laser is partially overlapping with the liquid phase the electrons generated from the liquid play an insignificant role for the

total electron yield in the high kinetic energy range.

Fig. 5.2 shows that the photoelectron emission remains unchanged up to a density of 0.2 mbar (see panels a-c). In this range of lower densities the high-energy cutoff appears at 230 eV in agreement with the 10 U_P-cutoff law of the HATI process. Additionally, the emission appears rather narrow around the laser polarization axis ($\theta_f = 0°$). Hence, all three spectra recorded at lower target densities demonstrate the photoelectron signal of rescattered HATI electrons ionized from the water gas.

A tremendous change is, however, observable upon further decreasing the distance between the jet surface and the laser focus, leading to the increase of the target pressure. Above 0.2 mbar, a nonlinear change of the emission spectrum is observable which can not be explained in terms of the aforementioned ionization channels of ATI and HATI (see Sec. 2.1). First, electrons with much larger kinetic energies are recorded: $T_{\max} = 400$ eV in the spectra shown in Fig. 5.2 (d) and (e), $T_{\max} = 550\,\text{eV} = 20\,U_P$ in the spectra shown in Fig. 5.2(f). Additionally, electron emission at larger angles becomes significant and a local maximum exceeding up to approximately 10 U_P is observable *perpendicular* to the laser polarization ($\theta_f = \pm 90°$). While the signal in Fig. 5.2(d) shows emission signals concentrated around 0° and ±90°, the larger broadening of the angular distribution in Fig. 5.2(f) gives rise to a plateau-like structure of higher isotropy. The evolution of the photoelectron signal under changing the target pressure from 1.6 mbar(d) to 6 mbar(f) suggests that either two different processes occur simultaneously or that the observed effect exhibits multiple emission features.

The development of the high-energy cutoff with the increase of the gas density can be seen in Fig. 5.3 which shows the kinetic energy distribution of photoelectrons emitted along the laser polarization direction ($\theta_f = 0°$). Again, three different phases are observable. (i) Up to 0.2 mbar, the emission appears to exhibit the features of the HATI process. (ii) Upon further density increase, the cutoff-law is violated and emission up to approximately 12 U_P is observable. (iii) Finally, at 6 mbar electrons up to 20 U_P are generated in the ionization process. As the observed spectral change appears to be more significant in the high-pressure range, one can conclude that the interaction of neighboring molecules with the quasi-free electron created during the ionization process becomes the dominant effect modifying the photoelectron emission. The most reasonable approach to describe the observations is to consider the laser-assisted electron scattering (LAES) process following the ionization event. Thus, the observed effect is represented in a stepwise manner: the electron is ionized from a parent molecule, oscillates in the driving laser field, and eventually scatters on a neighboring molecule and is further accelerated. The first observation of this effect during an ultrashort laser pulse was recently enabled[49], however, its probability in diluted samples appears rather weak.

Other considerations to describe the change of the photoemission spectrum could include electrostatic interaction between the sample and the electron cloud, molecule dissociation, multiple ionization, and cluster formation in the vicinity of the jet. As

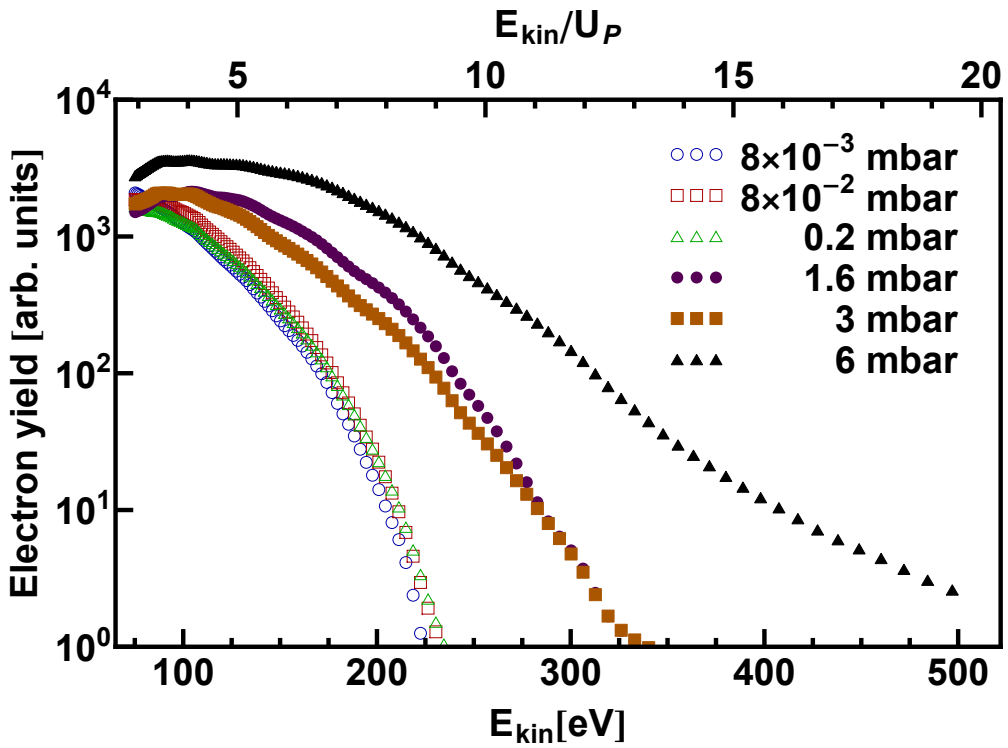

Figure 5.3.: Kinetic energy distribution of the photoelectron emission along 0° (parallel) polarization obtained at different target pressures[181]. All spectra are normalized to the the target pressure to distinguish linear and non-linear changes. Three phases are observable with corresponding cut-off energies of approximately10 U_P, 12 U_P and 20 U_P

already discussed above, the Coulomb interaction within the electron cloud can increase the kinetic energy of faster electrons and to some extent broaden the emission spectrum, while the electron interaction with the sample leads to a decrease in the final kinetic energy. However, such effects are negligible for the current experimental conditions in the considered energy range. Indeed, the fast electrons with kinetic energies above 50 eV leave the interaction region before a significant charge is accumulated. Molecular dissociation processes as discussed previosuly, can give rise to non-negligible deexcitation mechanism[185]. However, dissociation turns out to be much less efficient under ultrashort pulse conditions[186] as used in this experiment, and additionally can be delayed by some optical cycles which decreases the appearance of dissociated species during the laser pulse. Moreover, molecular dissociation is expected to be pressure independent which is in contrast to the observation described in this chapter. As reported before[8], sequential double ionization can lead to a shift of the high-energy cutoff. However, such an effect is only apparent in the case of ionization saturation and does not lead to an increase of the high-energy cutoff above the 10 U_P limit in the case of double ionization. It rather leads to a decrease of the kinetic energy cutoff of the single ionization (see Fig. 2 in Ref.[8]) due

to the saturation effect. Additionally, it is noteworthy that double ionization is typically orders of magnitude less probable under the given experimental conditions[190]. The existence of clusters in the vicinity of the jet was once observed indirectly by measuring the streaming current of a liquid microjet[191]. However, there are other approaches to explain these observations, e.g. as due to the charge separation within the jet without the cluster formation[192]. In general, it is assumed that the existence of clusters close to the jet surface is improbable due to the large amount of hydrogen bonds needed to be broken to form a cluster from the bulk. Most of the previous studies report a rather homogenous gas phase around the microjet[174, 175].

Thus, taking the LAES process into account appears as a right approach to the description of the observed photoemission. One condition for LAES to be observable is that ionization, quasi-free motion and scattering of a photoelectron on a neighboring molecule have to take place during the time interval of the laser pulse duration. Assuming that the water gas surrounding the liquid microjet is an ideal gas with a temperature of 0 °C and a pressure of 0.2 mbar, one can find that the number density of water molecules is of the order of $5 \times 10^{15}\,\mathrm{cm}^{-3}$. Hence, the mean distance between water molecules is of the order of 60 nm, which can be overcome within the pulse duration of 40 fs by electrons with kinetic energies higher than 6 eV. It means that at the present experimental conditions, only electrons with kinetic energies larger than this threshold can undergo subsequent LAES after the direct ionization process. As the semiclassical high-energy cutoff of the ATI spectrum in this experiment is of the order of 50 eV (corresponding to to a value of $2\,U_P$), a significant part of the emitted electrons can interact with the neighboring molecules. However, as the maximum of the electron emission spectrum lies considerably below the semiclassical cutoff (at approximately 5 eV as shown in Sec. 5.3), the amount of electrons which can scatter on neighboring molecules within the laser pulse duration will significantly increase with increasing the sample density. Thus, the density range between 0.2 mbar and 1 mbar can be considered as the threshold density for the LAES process to occur. In this discussion electrons generated in the HATI process are not considered. Even though the HATI electrons would fulfill the scattering condition due to their significantly higher kinetic energy, the HATI process has a much lower contribution to the total photoemission yield. Therefore one can disregard the sequence of events HATI →LAES and consider only the ATI →LAES sequence.

The existence of a threshold density is directly observable from the experimental results in Fig. 5.4 showing the dependency of the ionization yield as a function of vapor pressure. This is due to the fact that the yield of the HATI process and the yield of the ATI →LAES sequence have different characteristic dependencies on the gas density. The reason is that the HATI process involves interaction of one molecule with the laser field, whereas two molecules are involved in the sequence of ATI and LAES. The yield plotted in Fig. 5.4 was integrated over the kinetic energy range above 75 eV and over the entire solid angle of electron emission. One can see that in the diluted gas phase limit, the

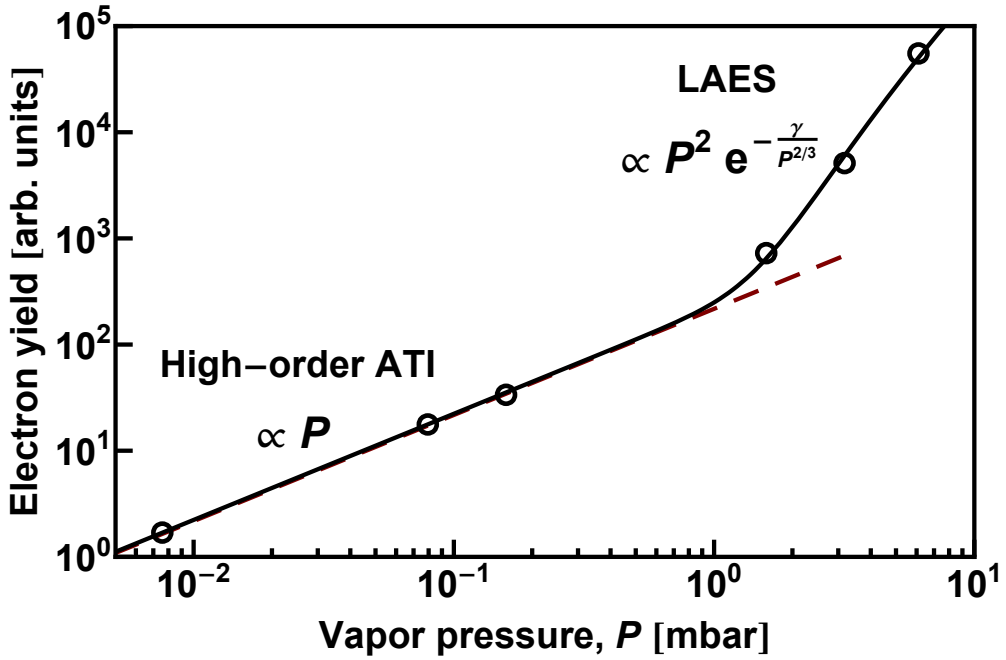

Figure 5.4.: Dependence of the total electron yield on the target vapor pressure obtained for water gas[181]. The transition from a linear to a non-linear (mostly quadratic) behavior is observable at approximately 1 mbar. The lower density region is dominated by the HATI process while in the high density regime ATI →LAES yields the largest contribution to the total ionization yield.

total electron yield is linearly dependent on the density of the target, corresponding to the ionization branch where only one molecule is involved (HATI). However, upon increasing the pressure above the threshold value of approximately 1 mbar the signal increase follows approximately a quadratic dependency, which is in agreement with a two-molecule process. Since the scattering condition on neighbors is dependent on the kinetic energy, a small correction arising from the kinetic energy distribution of ATI electron, which has an exponential behavior in the asymptotic limit, was added. As a larger amount of slower electrons can undergo the scattering with increasing pressure, the empirical function $P^2 \exp\left(-\mu/P^{2/3}\right)$ was used to describe the total electron yield in the high density regime. Here μ is a constant determined by the ATI ionization rate. The above estimated density threshold appears to be of the same order as the observed threshold in Fig. 5.4. This is despite the estimation assumed an inelastic scattering probability of unity, which can lead to an underestimation of the density threshold.

5.3. Simulation of laser-assisted scattering using the Kroll-Watson approximation

Whereas the density dependence of the total electron yield provides a strong support for the description of the observed processes beeing due to the LAES effect this section presents theoretical simulations of the emission spectrum after the the LAES process to prove its importance for the considered density range. The aim of these simulations is to show that after the LAES event the deviation of the photoelectron distribution from the HATI emission spectrum appears in agreement with the observed signal changes. A strict quantitative description of this process on the basis of the theoretical consideration used in this section is, however, not possible due to the complexity of the ionization pathways.

To describe the final emission spectrum after the LAES event, the initial distribution of incident electrons was simulated according to the quantum-mechanical description of the angle-resolved ionization rate presented in Sec. 2.1.1.3. Though the description was developed for the case of strong-field ionization of atomic particle, whereas a molecular target was used in the current experiment, the simulated emission of ATI electrons is satisfactorily reproduced by this theory. In addition, different tests confirmed that the initial electron distribution is not of crucial importance for the final emission spectrum of the LAES electrons and a slight inaccuracy in the description of the incident electron spectrum does not change qualitatively the final result. In the simulation of the initial distribution, a single-active electron configuration (1b1 water orbital) was considered with an ionization potential of 12.6 eV[193] and with the electron angular momentum in the ground molecular state $l = 1$ (p-electron)[194]. As reported elsewhere[188], the single-electron configuration is valid when a gas of non-oriented water molecules is considered. Additionally, the in Sec. 5.2.1 described laser parameters, including the spatio-temporal intensity distribution in the laser focus were considered. The result of the ATI simulation is shown in Fig. 5.5(a) and exhibits a typical emission structure including a narrow emission along 0° at larger kinetic energies, a high-energy cut-off of approximately $2\,U_P$, and the interference-like pattern on top of the average spectrum. The high-energy part along of the spectrum integrated over the emission angle can be described by an exponential decrease as discussed in Sec. 2.1.1.3. The global maximum of the emission spectrum appears at kinetic energies below 5 eV.

The angle-resolved energy distribution of electrons after the scattering event was calculated using the Kroll-Watson inelastic scattering approximation as described in Sec. 2.3.3, which is valid in the soft-photon regime. The calculations, however, require knowledge of the partial elastic scattering cross-section which can be either obtained from modeling of the water molecular potential or by interpolating the available experimental data[195, 196]. The latter was employed in the present simulations. Finally, the yield has to be integrated over all ionization channels satisfying the energy conservation,

$\boldsymbol{k}^2 - \boldsymbol{k}_\mathrm{i}{}^2 = 2n\omega$, to obtain the differential cross section after the LAES process, $\mathrm{d}\sigma(\boldsymbol{k})/\mathrm{d}\Omega_{\boldsymbol{k}}$:

$$\frac{\mathrm{d}\sigma(\boldsymbol{k})}{\mathrm{d}\Omega_{\boldsymbol{k}}} = \sum_n \int_{\boldsymbol{k}_\mathrm{i}} \mathrm{d}\boldsymbol{k}_\mathrm{i} \frac{\mathrm{d}\sigma_i(\boldsymbol{k}_\mathrm{i})}{\mathrm{d}\Omega_{\boldsymbol{k}_\mathrm{i}}} \frac{\mathrm{d}\sigma_n(\boldsymbol{k}, \boldsymbol{k}_\mathrm{i})}{\mathrm{d}\Omega_{\boldsymbol{k}}} \tag{5.1}$$

where $\mathrm{d}\sigma_i(\boldsymbol{k}_\mathrm{i})/\mathrm{d}\Omega_{\boldsymbol{k}_\mathrm{i}}$ represents the initial electron distribution due to the ATI process (as described above) and $\mathrm{d}\sigma_n(\boldsymbol{k}, \boldsymbol{k}_\mathrm{i})/\mathrm{d}\Omega_{\boldsymbol{k}}$ represents the n-photon inelastic scattering cross section described by using the Kroll-Watson approximation (KWA) (Eq. (2.145)).

The result of simulation of the angle-resolved kinetic energy distribution of electrons after the scattering event is shown in Fig. 5.5(b). The remarkable features are the extension of the high-energy cut-off up to $12\,U_\mathrm{P}$ and the broad emission around $\theta_f = 0°$ and a local maximum at $\theta_f = \pm 90°$. Additionally, two plateaus are present corresponding to forward and backward scattering during the LAES event. The predicted emission, thus, qualitatively reproduces the major features observable in the experimental data for 1.6 mbar and 3 mbar (Fig. 5.2(d)-(e)).

The discrepancy between predicted and observed spectra at 6 mbar pressure (Fig. 5.2(f)), however, suggests that another ionization channel is opened at higher densities. Due to the smaller distance between molecules, more electrons generated by ATI can scatter on neighboring particles even earlier during the laser pulse. Their acceleration by LAES then yields the possibility that these electrons can visit another neighbor during the pulse and, thus, can be involved in a two-step scattering channel (ATI $\rightarrow$ LAES $\rightarrow$ LAES). The emission of this step-wise scattering can be represented in a similar fashion:

$$\frac{\mathrm{d}\sigma(\boldsymbol{k})}{\mathrm{d}\Omega_{\boldsymbol{k}}} = \sum_l \int_{\boldsymbol{k}_\mathrm{m}} \mathrm{d}\boldsymbol{k}_\mathrm{m} \frac{\mathrm{d}\sigma_i(\boldsymbol{k}_\mathrm{m})}{\mathrm{d}\Omega_{\boldsymbol{k}_\mathrm{m}}} \frac{\mathrm{d}\sigma_l(\boldsymbol{k}, \boldsymbol{k}_\mathrm{m})}{\mathrm{d}\Omega_{\boldsymbol{k}}} \tag{5.2}$$

where $\mathrm{d}\sigma_i(\boldsymbol{k}_\mathrm{m})/\mathrm{d}\Omega_{\boldsymbol{k}_\mathrm{m}}$ represents the intermediate electron distribution after the first (and before the second) LAES event (Eq. (5.1)) and $\mathrm{d}\sigma_l(\boldsymbol{k}, \boldsymbol{k}_\mathrm{i})/\mathrm{d}\Omega_{\boldsymbol{k}}$ represents the l-photon inelastic scattering cross section described by the KWA (Eq. (2.145)).

The emission of such a double scattering event is displayed in Fig. 5.5(c). Again two major features are observable. First, the energy cut-off is further increased up to approximately $20\,U_\mathrm{P}$. Second, the spectrum appears broadened and the initially sharp plateau structure (especially for large emission angles) is less visible. Both features are in qualitative agreement with the experimental data.

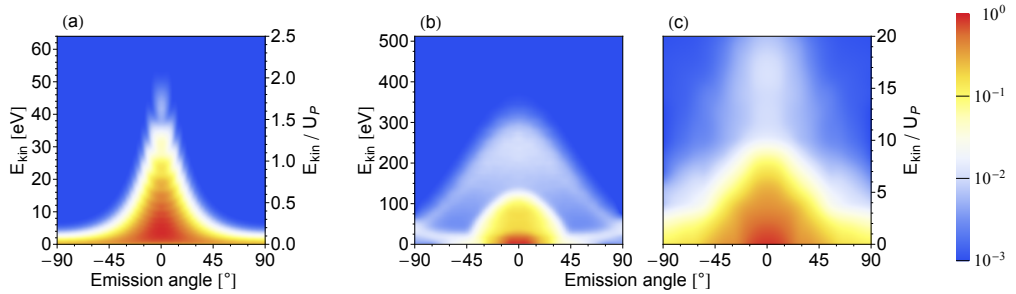

Figure 5.5.: Results of simulations of photoelectron distribution.[181] (a) ATI emission of water molecules calculated on the basis SAE considerations (1b1 orbital). Due to Coulomb and intramolecular interactions this results only roughly represents the water emission but suffices to describe the initial ionization process. The emission appears rather narrow along 0° and shows an exponentially decreasing behavior with an cutoff of approximately $2\,U_P$. (b) ATI $\rightarrow$ LAES emission simulated on the basis of the Kroll-Watson scattering approximation. The emission appears broad and electron yield at kinetic energies larger than the HATI cutoff of $10\,U_P$ is observable. Additionally, the features due to forward and backward scattering, leading to local maxima at $\theta_f = \pm 90°$, are evident. (c) ATI $\rightarrow$ LAES $\rightarrow$ LAES emission simulated as a two-step process on the basis of the Kroll-Watson scattering approximation. The emission is further enhanced towards larger kinetic energies with a cut-off of approximately $20\,U_P$ and acquires a broad angular distribution.

5.4. Density studies on acetone and water

While these above presented results of experiment (Sec. 5.2) and simulation (Sec. 5.3) show the first fingerprints of laser-assisted scattering during the laser pulse, some questions remain open and will be answered in this section. First of all, the transition from the diluted gas phase to the dense gas phase needs to be described in more detail. This includes the precise determination of the density threshold and verification of the existence of other thresholds for the secondary or higher-order scattering events if they exist. Additional scatter events should manifest in the photoelectron emission as well as in the electron yield dependency on the molecular density. Since the present approach (especially the simulation) shows that small variations in the initial ionization process (ATI spectrum) do not affect the final emission spectrum, the characterization of LAES emission in dense gas experiments should be of general character and not limited to the water case. Thus, an extension to other samples is required to either falsify or prove this assumption and, hence, the underlying theory. Furthermore, there is so far no discussion of the transition from the dense gas to the liquid phase and how much the emission from liquid disturbs the recorded dense-gas spectra. Finally, it would be favorable to clearly discriminate emission from isolated molecules and emission involving collective effects in order to test directly the theory describing these effects.

Due to the technical limitations of the experimental setup E1 which does not allow to acquire shown experimental data with a higher quality and resolution a more sophisticated experimental setup (experimental setup 2 (E2)) was designed, manufactured, and calibrated. This development lead finally to the opportunity to study in greater detail laser-assisted scattering induced by ultrashort laser pulses in water and acetone.

5.4.1. Experimental conditions

The experimental conditions are in general similar to those described in Sec. 5.2.1. However, some changes in the experimental setup and the laser parameters will be specified below.

As mentioned above, the experimental setup E2 was used in combination with the spectrometer S1 for this study. The spectrometer was operated in the field-free (drift) mode with an electron acceptance angle of 1.1° which constitutes the angular resolution in this experiment. To avoid saturation of the detector and signal amplification devices, the electron signal was restricted by applying of a low electron kinetic energy filter as it was accomplished in the previous study. The threshold was set to 50 eV, effectively decreasing the amount of slow electrons by several orders.

Linearly polarized near-infrared laser pulses of 40 fs pulse duration and central wavelength of 1300 nm were focused by a spherical lens into the experimental chamber into a focal spot of approximately 20 µm. The pulse energy was attenuated to approximately 15 µJ yielding a laser peak intensity of about $5 \times 10^{13}\,\mathrm{W\,cm^{-2}}$ and giving rise to the ponderomotive energy of 9 eV. The beam polarization axis was controlled with the use of a waveplate allowing angle-resolved measurements.

Apart from using water as a sample, a liquid microjet of acetone was applied as well. Acetone has an equilibrium vapor pressure which is almost two orders of magnitude larger than the equilibrium pressure of water, allowing to study the nonlinear density effects in a wider pressure range. A small concentration (20 mM) of NaI was added to both water and acetone samples to avoid streaming potentials[164]. As in the previous experiment the liquid microjet was injected into the vacuum and the distance between the laser focus and the jet surface was adjusted to vary the target density in the interaction volume (see Sec. 3.3.2). However, due to the improved experimental conditions the full angular emission was recorded in shorter time intervals allowing to acquire data under more stable conditions and with a much larger amount of sampled densities. As before, the jet temperature is assumed to be 0 °C near to the interaction region giving rise to an equilibrium vapor pressure at the liquid surface of 6 mbar for water and 100 mbar for acetone. As discussed above, the jet temperature can affect the exact pressure calibration up to a constant factor and can be different for both samples. Hence, an absolute comparison of recorded spectra for acetone and water is not possible, but equally is not necessary for the interpretation of the data.

5.4.2. Linear and nonlinear density effects in the strong-field emission at liquid-gas interface

As in the previous experiments the angle-resolved emission was recorded for a set of distances from the jet surface to the laser focus. However, contrary to the prior study the sampling density was increased by approximately one order of magnitude to approximately 50 positions per sample, allowing to quantify the changes in the photoemission in much greater detail. For acetone (water), the sampled pressure range was of the order of 7×10^{-2} mbar to 1×10^{2} mbar (4×10^{-3} mbar to 6 mbar). Two representative photoelectron emission spectra of acetone in both low and high pressure limits (1×10^{-1} mbar and 2×10^{1} mbar, respectively) are shown in Fig. 5.6. The respective angular emission of electrons ionized from water are very similar and, therefore, not shown. As shown before and evident from Fig. 5.6(a), the emission in the diluted gas limit at kinetic energies above 50 eV ($\approx$5.5 U_P) is prevailed by electrons generated by the HATI mechanism and, thus, is dominated by an interaction of isolated molecules with the intense laser pulse. The emission exhibits a narrow angular distribution parallel to the laser polarization axis and the high energetic electrons are observable to a cut-off energy of 10 U_P ($\approx$90 eV). The spectrum undergoes a tremendous change upon increasing the target density (as one can see in Fig. 5.6(b)), which is similar to the emission behavior reported above. First of all, electrons with kinetic energies above the HATI cutoff energy of 10 U_P are observable. Their yield can be distinguished from the noise level in the kinetic energy range that extends to approximately 20 U_P. Additionally, the emission is remarkably broadened and a significant ionization yield arises at emission angles of $\pm 90°$. Similar to the ionization of dense water gas, emission perpendicular to the laser polarization axis can exceed energies of 5 U_P and a significant contribution appears with a large azimuthal angle of 45° and extends over kinetic energies up to 10 U_P. One can directly see that the dense gas emission from water (Fig. 5.2(f)) and acetone (Fig. 5.6(b)) appear rather similar, despite the differences in the molecular structure, the ionization pathways and potential (the orbital structure), and the equilibrium vapor pressure at the jet surface. These observations are in agreement with the findings of the theoretical study presented above (see Sec. 5.3).

Contrary to the analysis of the density dependent angular photoelectron emission used above (see Sec. 5.2), where only the total electron emission was studied as a function of density and the qualitative results shown in Fig. 5.4 were obtained, in the current study the pressure dependency is considered independently for all observable kinetic energies and emission angles with a resolution of 1 eV and 1°, respectively. This new routine allows to decompose the recorded spectra into the sum of emission yields of the HATI and the iHATI process due to their characteristic linear and square density dependency, respectively. This quantitative approach, however, requires a much higher sampling density, which is accomplished in the current experiment but was lacking in the

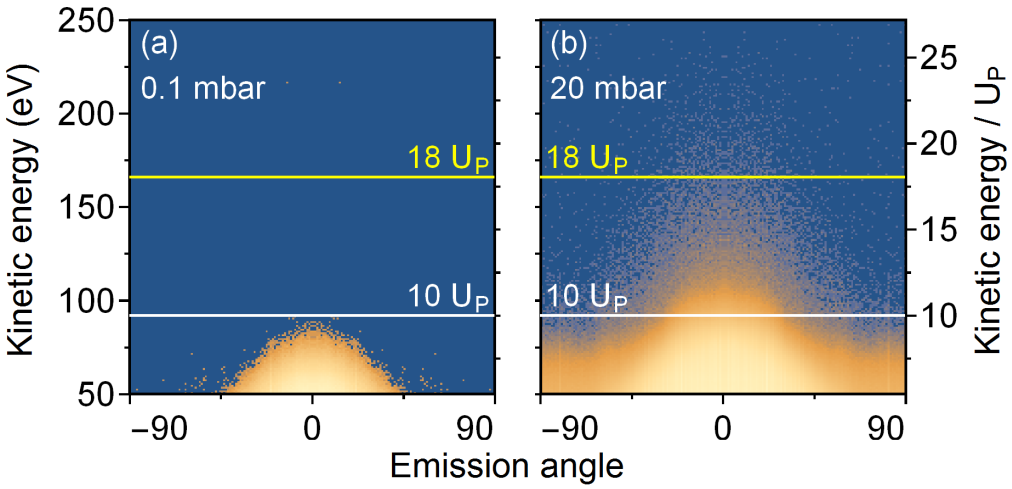

Figure 5.6.: Angle-resolved photoelectron emission spectra obtained for acetone. Different panels denote different target pressures where (a) represents a typical diluted gas phase emission (1×10^{-1} mbar) and (b) a representive dense gas emission spectrum (20 mbar). Both the HATI and iHATI processes contribute to the electron yield in the shown energy range above 50 eV. Horizontal lines indicate kinetic energies of 10 U_P (HATI cutoff energy) and 18 U_P (iHATI cutoff energy, as discussed in Sec. 5.5). Reprinted figure with permission from [Wilke et al.[182], Physical Review A, 94, 033423 (2016)] Copyright (2016) by the American Physical Society.

previous study. The accuracy of this approach also depends on the precise knowledge of the relative sampled target pressure, which is provided due to the short acquisition time per position of the jet relative to the laser focus and became possible due to the improvements on the experimental setup.

A typical dependency of the partial electron yield for a given kinetic energy interval and emission angle on the target gas pressure is displayed in Fig. 5.7. The signal shown in this figure was integrated over the emission space including the kinetic energy range between 85 eV and 150 eV and emission angles between 10° and 20°. This integration range lies essentially near the HATI cutoff region. The energy and angle intervals of integration are chosen larger than the resolution values values specified above for the sake of demonstration. The intervals of the resolution size are used in the data analysis presented below. For the illustrative purposes, only results of the water ionization is shown as they reveal a larger dynamic range of HATI, iHATI, and liquid-phase emission and, thus, the contribution from the three phases (diluted gas, dense gas, and liquid phase) are well distinguishable. One can see that the liquid phase is pronounced by its sudden step-wise increase in the photo-ionization yield upon overlapping the high-intensity part of the laser beam with the liquid phase. Apart from the large number density increase of illuminated molecules due to the phase transition, other possible reasons for the sudden

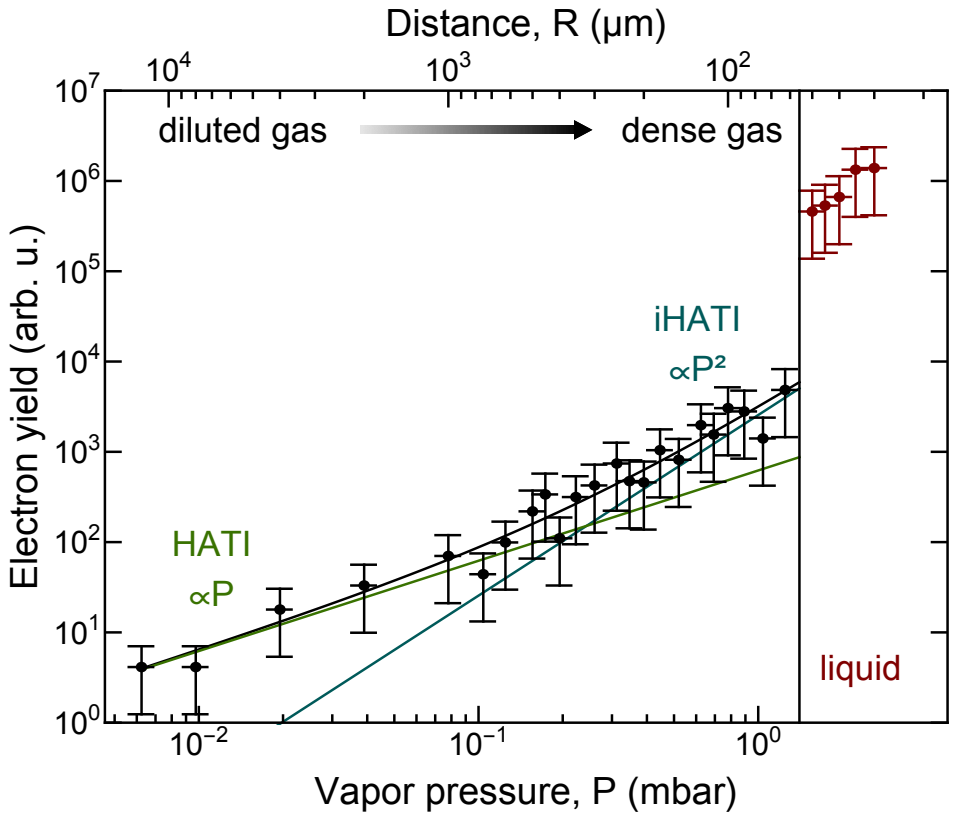

Figure 5.7.: Ionization yield of water as a function of the distance between the laser focus and the micro-jet (top scale). The partial electron yield is integrated over the range of electron kinetic energies from 85 eV to 150 eV and emission angles $10° \leq \theta \leq 20°$. The experimental signal dominated by emission from the liquid phase is marked by red color. Strong-field ionization of water in the gas phase exhibits a linear (green) and a quadratic (cyan) dependency in the limit of dilute and dense gas, respectively. A fit to the linear combination (superposition) of these dependencies is indicated by the black line. The gas pressure (bottom scale) is derived from the hyperbolic decrease of the density as a function of distance and is calibrated according to the phase transition from liquid to dense gas. The equilibrium vapor pressure of water at 0 °C of 6 mbar. Reprinted figure with permission from [Wilke et al.[182], Physical Review A, 94, 033423 (2016)] Copyright (2016) by the American Physical Society.

increase are ionization of dissolved iodine ions at the surface of the liquid jet, a multi-step iHATI process efficiently heating electrons and possibly leading to secondary ionization, or other so far not discussed collective effects which require an even larger target density. This phase-transition is observable for water and acetone and appears at small (< 20 µm) distances between the jet surface and the laser focus, whereas moderate variations are present when the jet is moved across the laser beam. Ionization of the liquid phase and its description, however, lies beyond the scope of this study.

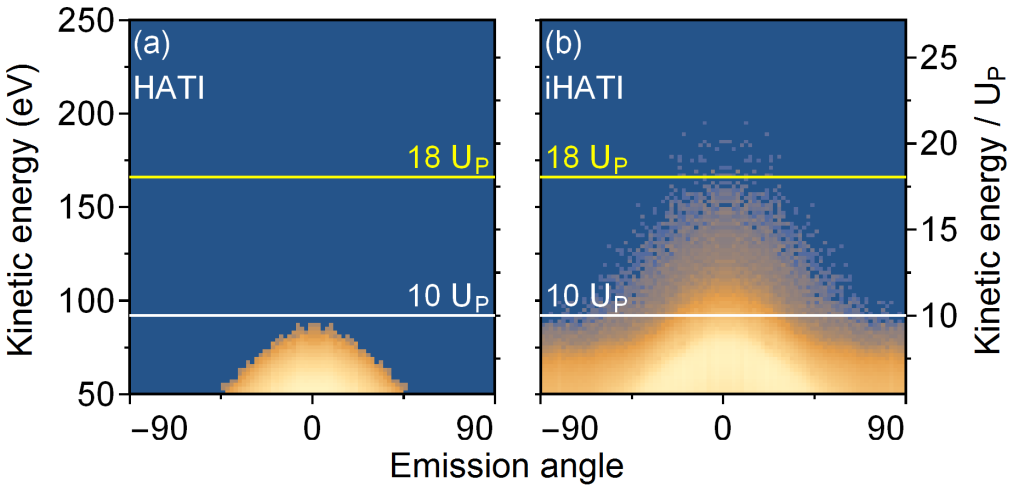

Figure 5.8.: Decomposition of the photoemission signal of acetone. (a) HATI (linear dependency) and (b) iHATI (quadratic dependency) signal as a function of energy and emission angle. Each spectrum shows the coefficients of a polynomial fit to the partial electron yield depending on the target pressure. The HATI signal appears similar to the gas phase emission and shows a typical HATI spectrum. The nonlinear emission represents the first published iHATI spectrum. Reprinted figure with permission from [Wilke et al.[182], Physical Review A, 94, 033423 (2016)] Copyright (2016) by the American Physical Society.

As one should expect for a single-molecule and two-molecule processes, the ionization yield follows a linear or quadratic dependency on the pressure, respectively. This behavior is consistent with the results shown in Fig. 5.7, where the two dependencies are apparent in the limit of low and high vapor pressure, respectively. Similar results were obtained for both water and acetone. However, due to the larger vapor pressure the iHATI process dominates in the applied pressure range in the case of acetone. The quadratic dependency of the photo-ionization yield fingerprints the iHATI process in the current experiment and, thus, can be exploited to retrieve the pure iHATI emission spectrum by decomposing it from the HATI signal. The total yield, $Y(T, \theta_f)$, as a function of electron kinetic energy, emission angle, and target gas pressure p reads:

$$Y(T, \theta_f, p) = Y_{\mathrm{HATI}}(T, \theta_f)p + Y_{\mathrm{iHATI}}(T, \theta_f)p^2 \tag{5.3}$$

The decomposed HATI (Y_{HATI}) and iHATI (Y_{iHATI}) emission spectra for acetone are shown in Fig. 5.8. Such a procedure was never applied before and, thus, Fig. 5.8(b) represents the first experimental emission spectrum of the iHATI process.

5.5. Semiclassical trajectory analysis

To describe the ionization process in dense media, a different approach is employed than before in Sec. 5.3. Although the Kroll-Watson approximation (KWA) appears as a valid starting point to characterize the electron trajectory after the ionization process and was shown to be in qualitative agreement with experimental results, it lacks fundamental insights, is numerically unstable, and depends on the knowledge of the cross-section values for the elastic scattering and the initial ionization distribution. However, the present experimental results demonstrate that both acetone and water give rise to rather similar spectra of the iHATI emission. This implies that the iHATI yield is barely dependent on the elastic scattering cross section and on the spectrum of direct ionization, which was confirmed in the previous simulations based on the KWA (see discussion in Sec. 5.3). Finally, the KWA describes the electron-photon interaction during the scattering event as an event completely independent on the ionization process.

To make the description more comprehensive and to improve the numerical stability and overall description of the scattering process within the ionizing laser pulse, the application of semiclassical trajectory-based simulations, as discussed in Sec. 2.3.3.2.1, is performed in this section. As the trajectory conditions are derived on the basis of the quantum-mechanical description in the low-frequency regime ($\gamma \ll 1$), the allowed transitions are restricted to those satisfying the energy conservation rule during the scattering event (Eq. (2.146)), but can also be extended to satisfy further conditions such as the HATI condition (Eq. (2.101)) or other coherent conditions (e.g. scattering on a periodic potential or within the parent molecule[26]).

Summarizing for the currently observed iHATI process, a quasi-free electron with momentum $\boldsymbol{k}_i$ scatters on a potential leading to the final electron kinetic energy, T:

$$T = 4\mathrm{U_P}\left(\alpha^2 + \beta\gamma_i + \frac{\gamma_i^2}{2} \pm\alpha\sqrt{\alpha^2 + 2\beta\gamma_i + \gamma_i^2}\right) \tag{5.4}$$

with

$$\alpha = \cos\omega t \cos\theta_f \qquad |\alpha| \leq 1 \tag{5.5}$$

$$\beta = \cos\omega t \cos\theta_i \qquad |\beta| \leq 1 \tag{5.6}$$

$$\gamma_i = \frac{\boldsymbol{k}_i}{A} \qquad 0 \leq \gamma_i \leq 1^{\mathrm{A}} \tag{5.7}$$

One can directly see that the sign of $a = \cos\theta_f \cos\omega t$ and $b = \cos\theta_i \cos\theta_f$ in combi-

[A] This condition represents the semiclassical cutoff law of the direct ionization which limits the final electron kinetic energy to below $2\,\mathrm{U_P}$. In the quantum-mechanical description the ionization yield, however, decreases exponentially with increasing final energy and, thus, yielding larger values of γ_i than 1.

nation with the sign in front of the square root define different branches of emission. Indeed four different branches (each one is twice degenerate) can be identified. In the following part only the positive sign in front of the square root is considered and, thus, the degeneracy is omitted.

The first branch ($\{a > 0, b > 0\}$) is strictly monotonic and gives rise to final kinetic energies which increase with the increase of the parameters a, b and γ_i. This branch yields a maximum kinetic energy of $18\,\mathrm{U_P}$ when $a = b = \gamma_i = 1$ (thus, along the laser polarization axis), and zero kinetic energy if $a = \gamma_i = 0$ (perpendicular to the laser beam) independent on b. This branch produces the fastest electrons and can be expanded around the maximum in terms of θ_f as:

$$T = (18 - 9\theta_f^2 + O[\theta_f]^4)\mathrm{U_P} \quad , \tag{5.8}$$

giving rise to a parabolic shape in the kinetic energy distribution. Perpendicular to the laser polarization axis ($a = 0$), the highest kinetic energy is $6\,\mathrm{U_P}$. This energy cutoff is linearly decreasing with the increase of θ_f at larger angles.

The second branch ($\{a > 0, b < 0\}$) is more complex and yields the maximal kinetic energy of $(6{+}4\sqrt{2})\mathrm{U_P} \approx 11.66\,\mathrm{U_P}$ (in the figures and in the text this value is approximated by $12\,\mathrm{U_P}$) in the direction parallel to the laser polarization axis ($a = 1$), with a similar quadratic dependency on the emission angle as before (see Eq. (5.8)). The energy cutoff is linearly decreasing with the increase of the emission angle at larger angles and acquires a minimum of $2\,\mathrm{U_P}$ at $\theta_f = \pm 90°$.

The remaining two branches merely denote the same conditions as the first and second branches just in a flipped laser field (or scattering in the opposite hemisphere). Here the maximal kinetic energy is observable perpendicular to the laser polarization axis and reaches values of $6\,\mathrm{U_P}$ (branch III, $\{a < 0, b > 0\}$) and $2\,\mathrm{U_P}$ (branch IV, $\{a < 0, b < 0\}$), representing a continuous extension of the branches (I) and (II) into the opposite hemisphere. However, for the description of the present data branches III and IV are not of importance since their energy cutoffs lie below the energy range considered in this study.

The final emission spectrum, $w_f(\boldsymbol{k}_f, \theta_f)$, can be obtained by integration over the initial momentum space, the scatter phase (ωt), and by applying the focal averaging (see Sec. 2.1.1.5.4):

$$w_f(\boldsymbol{k}_f, \theta_f) \propto \int_0^{I_0} \mathrm{d}I \int_0^{2\pi} \mathrm{d}\omega t \int_0^{\infty} \mathrm{d}\boldsymbol{k}_i \delta\left(\frac{\boldsymbol{k}_f^2}{2} - T(\alpha, \beta, \gamma_i)\right) w_i(\boldsymbol{k}_i, \theta_i) \frac{\mathrm{d}\sigma_n(\boldsymbol{k}_i, \boldsymbol{k}_f)}{\mathrm{d}\Omega} f(I) \tag{5.9}$$

where $f(I) = \sqrt{\ln I_0/I}\, I_0/I$ denotes the probability density of the local intensity I, $\mathrm{d}\sigma_n(\boldsymbol{k}_i, \boldsymbol{k}_f)/\mathrm{d}\Omega$ represents the scattering cross-section of the n-photon channel and $w_i(\boldsymbol{k}_i, \theta_i)$ is the initial electron momentum distribution before the scattering event. The

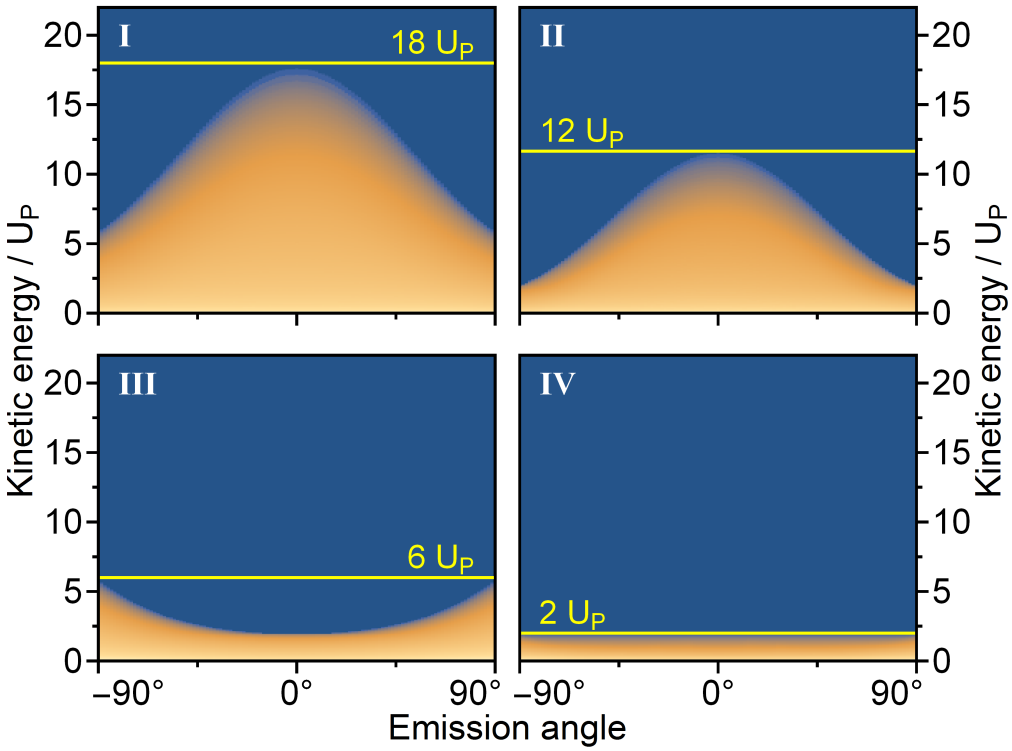

Figure 5.9.: Angle-resolved emission spectrum of the iHATI process. The panels show the contribution of each of the four electron trajectory branches: (I) $\{a > 0, b > 0\}$, (II) $\{a > 0, b < 0\}$, (III) $\{a > 0, b < 0\}$, (IV) $\{a < 0, b < 0\}$, where $a = \cos\theta_i \cos\phi$ and $b = \cos\theta_i \cos\theta_f$. The corresponding cutoff energies are $18\,U_P$, $12\,U_P$, $6\,U_P$ and $2\,U_P$, respectively. The ionization branches (I) and (II) lead to emission of electrons mostly along 0° while branch (III) enhances emission perpendicular to the laser polarization axis and branch (IV) appears rather isotropic. Reprinted figure with permission from [Wilke et al.[182], Physical Review A, 94, 033423 (2016)] Copyright (2016) by the American Physical Society.

latter, however, plays only a minor role as discussed before and, thus, is assumed to be constant in the energy range up to the ATI cutoff energy of $2\,U_P$ and to be isotropic:

$$w_i(\boldsymbol{k}_i, \theta_i) \approx \begin{cases} 1 & \frac{\boldsymbol{k}_i^2}{2} \leq 2\,U_P \\ 0 & \text{otherwise} \end{cases} \tag{5.10}$$

The scattering cross-section is also assumed to be constant, which is supported by the fact that there are rather small differences in the electron emission from acetone and water. Even though this cross-section might be significantly different, its influence on the final spectrum appears to be of minor importance for both samples.

The full emission spectrum of each branch is presented in Fig. 5.9 where the plateau structures up to the corresponding cutoff-energies are observable. The parabola shapes

discussed above at $\theta_f = 0°$ and the linear slopes at larger angles are apparent as well. It is noteworthy that the high-energy cutoff of each branch cutoffs is strongly dependent on the range of γ_i which is only semiclassically limited to below 1. An increase of γ_i by 10 % above unity already yields cutoff values of 19.2 eV, 12.4 eV, 6.8 eV and 2.4 eV, respectively, showing that the strict application of the simple-man model (SMM) is restricted to the low frequency limit. One can directly see that the application of the SMM reproduces at least qualitatively the experimental results of Sec. 5.2 and Sec. 5.4. One should point out that the results of the previous study (see Sec. 5.3) supported the theory of a multi-step scattering process describing emission up to 20 U_P, while the SMM theory suggests a multi-plateau structure even in a single scattering event. Here the strength of the semiclassical theory is directly demonstrated. As the KWA and the SMM approach represent complementary methods to describe the same process, their combination can be applied as well (in the low frequency limit). The straight application of the KWA on all trajectories, however, seems to overemphasize the emission branch II of the SMM. This is obvious by considering the scattering condition Eq. (2.146) which reflects a quantum-mechanical property, and, thus, by restricting the amount of regarded trajectories undergoing a scattering event. For the interpretation of the current experiment, the SMM description of the iHATI process appears to be the best approach to describe the final emission. The KWA, however, still can be applied to further improve the description by explicitly evaluating evaluating the differential cross section $\mathrm{d}\sigma_n(\boldsymbol{k}_i, \theta_i, \boldsymbol{k}_f, \theta_f)/\mathrm{d}\Omega$. To generalize the decription of the iHATI process for a large set of dense media (dense gas samples) and laser parameters, the three issues need to be comprehensively considered: (i) the initial electron distribution (e.g. by means of quantum-mechanical simulations of ATI), (ii) the semiclassical trajectories (e.g. in terms of the SMM), and (iii) the trajectory weighting (e.g. by applying the KWA). However, in the present case the SMM alone provides a satisfactory description of the experiment.

A comparison of the experimental emission of acetone and water with the SMM calculations can be found in Fig. 5.10. Overall, the emission is well described and the most significant features of the iHATI process are reproduced.

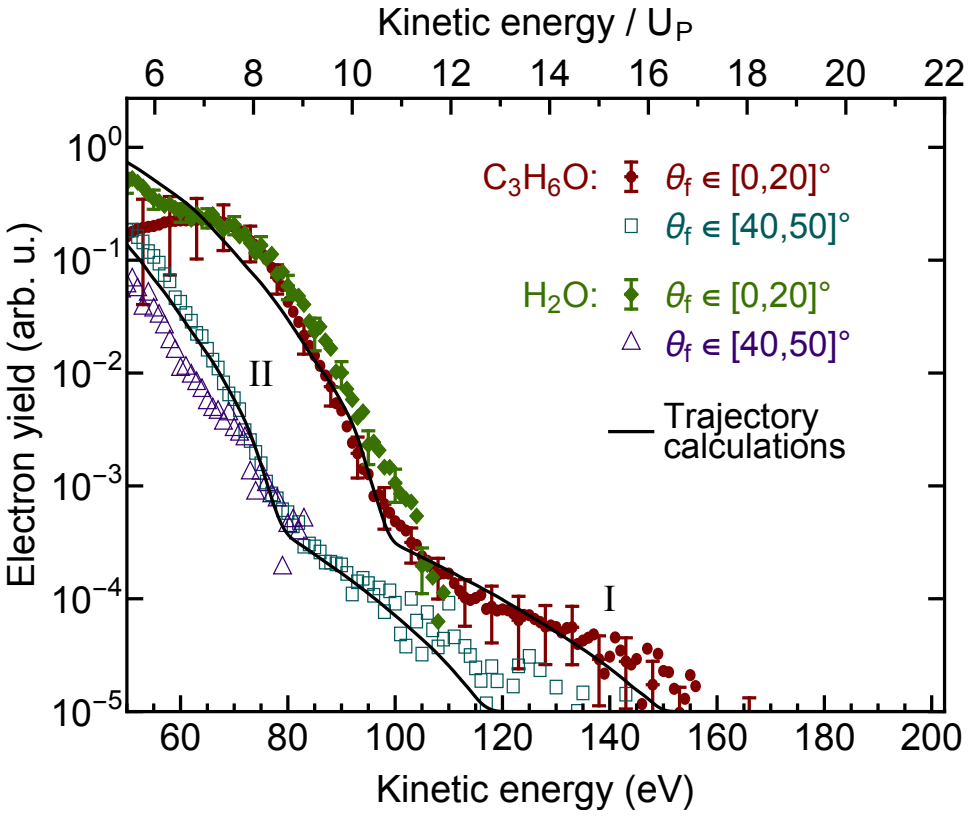

Figure 5.10.: Comparison of experimental results and semiclassical trajectory simulations. The partial electron yield of water (H2O) and acetone (C3H6O) ionized solely by the iHATI process integrated over two chosen intervals of the emission angle θ_f is illustrated for experimental data (symbols) and its corresponding simulation (solid line). The relative amplitude of the branches I and II (see as well Fig. 5.9) where fitted to the acetone data. Other branches do not contribute to the shown energy range for the given angular intervals. Both I and II branches yield the formation of plateaus in the emission spectrum characterized by the cutoff energies of 18 U_P and 12 U_P, respectively, and are observable in both the experimental and the simulated data. The water yield is normalized to the acetone signal. The agreement between simulation and experiment and between both samples is remarkable, although the initial ionization step is different for acetone and water and is "artificial" in the case of the simulation. Reprinted figure with permission from [Wilke et al.[182], Physical Review A, 94, 033423 (2016)] Copyright (2016) by the American Physical Society.

6. Results and Discussion on Ionization of a Condensed Medium

6.1. Introduction

The findings in Sec. 5 demonstrate that the strong-field ionization of single molecules is strongly affected by the presence of neighboring molecules in the dense-gas medium. While the number of possible interactions with neighbors appears to be limited to one for the applied pulse duration of 40 fs and the vapor pressure of ≈ 100 mbar, the study of a sequence of laser-assisted scattering events is possible if the number density of molecules is sufficiently increased. This condition is realized when the short laser pulse interacts with the liquid phase. As will be shown in the present chapter, the sequential scattering leads to an extension of the observable electron cut-off energies from $2\,U_P$ (above threshold ionization (ATI)) to $18\,U_P$, $50\,U_P$ and $98\,U_P$ for the first, second, and third scatter event of the incoherent high-order ATI (HATI) event, respectively. In general, the high-energy cutoff of the nth scatter event is described by $E_{kin} \leq 2(1+2n)^2 U_P$ and, thus, is quadratically increasing with n. However, the probability of a subsequent scattering event after the nth event decreases with increasing n due to the condition that all scattering events should occur during the same ultrashort laser pulse and due to the decrease of the elastic scattering probability with increasing kinetic energy (see Sec. 3.3.1).

Although the liquid phase offers the possibility to observe higher-order scattering events, the evidence of such occurrences is considerably harder to prove than in the dense-gas study as the particle density is not controllable. Additionally, the direct interaction of neighboring molecules complicates the description of the ATI step for instance due to resonances in the liquid phase (e.g. charge-transfer-to-solvent states[197, 171], resonant multiphoton excitation of the liquid (water) conduction band[198]), multiple ionization channels (e.g. inner vs. outer ionization[199, 200]), and solvent-solute effects (i.e. chemical shifts[201, 202]). Due to these circumstances a theoretical description of the observed experimental results is barely possible and are therefore only partially presented here.

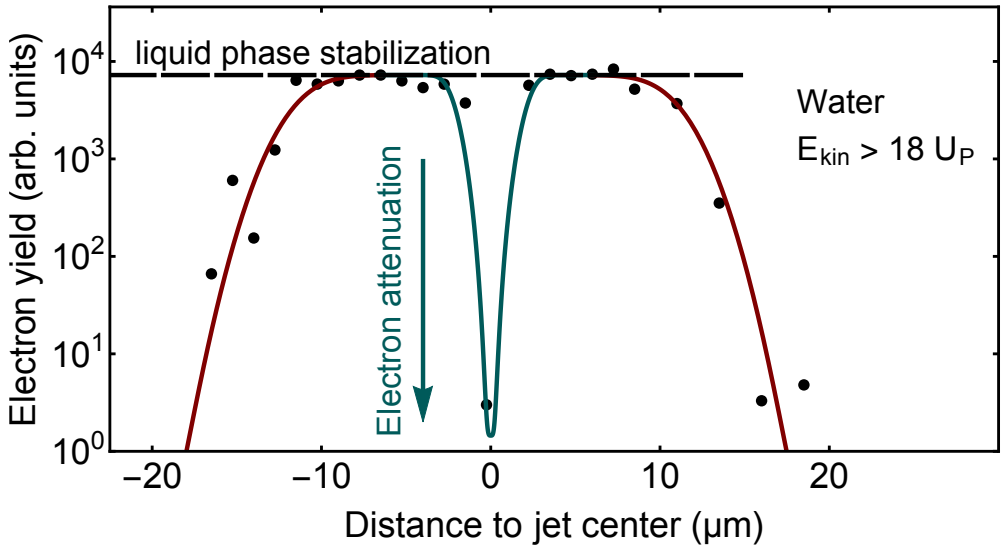

Figure 6.1.: Photoelectron signal integrated over electron kinetic energies above the single iHATI high-energy cutoff of 18 U_P as a function of the distance between the laser focus to the water jet center. Overlap of the liquid phase with the laser focus leads to an increase of the signal by several orders of magnitude within a distance range of a few µm. When the laser beam and the jet are aligned on top of each other, the photoelectron signal vanishes due to the small EAL in the liquid phase of a few nm.

6.2. Strong-field photoelectron spectroscopy of liquids

6.2.1. Experimental conditions

In this work, the experimental conditions were set as in Sec. 5.4. However, this time the liquid phase of the microjet, instead of the surrounding vapor, was examined. The distance between the center of the jet and laser beam, however, still represents an important parameter as shown below. To avoid streaming potentials a small concentration (10 mM) of sodium iodine was added.

6.2.2. Strong-field spectroscopy of a liquid surface

Upon overlapping the laser beam with the liquid phase, the strong-field photoelectron emission is significantly enhanced in comparison to the dense-gas case (as shown in Fig. 5.7). The explanation for such a behavior is not straightforward and requires consideration of different aspects including the target sample and the laser parameters. The emission can be significantly enhanced because of a number of different circumstances: the liquid phase contains a larger number of molecules per volume (number density), the ionization potential of molecules in the liquid phase is typically lower than in the gas phase[158], the electron yield due to ionization of solutes (with even lower ionization potential and

possible surface enrichment[159]) can give rise to a large contribution to the emission spectrum, and additional ionization pathways are available as resonant [203, 204] and inner and outer ionization[35]. On the other hand, the detected photoemission signal can be suppressed due to the reduced EAL in the liquid phase (see Sec. 3.3.1) defined by the elastic and inelastic electron scattering cross-section[205, 206] or it can be affected by the space-charge effect (SCE) [207, 208, 209].

Sampling the electron yield as a function of the distance between the laser focus and the liquid jet (see Fig. 6.1) demonstrates the interplay of such enhancing and suppressing effects. To exclude the contribution from dense-gas ionization slow electron signal below the iHATI energy cutoff of $18\,U_P$ was disregarded in the shown data. Upon intersecting the laser beam with the jet surface, the signal increases by four orders of magnitude within a distance interval of 10 µm until the electron yield becomes stable for a few µm (the stabilization appears in the same position range independent on the selected threshold energy). Upon overlapping the jet and the focus center-to-center, the electron yield decreases nearly to zero and increases again to the same maximum value, within a 5 µm distance. In this central region, the whole interaction volume, where ionization takes place lies in the bulk of the jet[1] and, thus, the small EAL leads to the tremendous decrease of the electron yield. At the back side of the jet, the yield exhibits rather similar dependency on the lase-beam-to-jet distance, though the signal value is slightly lower at the front side. This is because the jet of 20 µm size partially blocks the spectrometer entrance of 200 µm. This observed behavior of the emission signal allows to easily calibrate the distance between the jet and the laser focus. The region within the jet is considered to be dominated by the liquid-phase emission and is considered below in more detail (see Sec. 6.2.3).

Apart from the electron detection, photons emitted from the interaction region were also recorded with the same microchannel plate (MCP) detector. Upon overlapping the laser beam with the liquid surface, the amount of recorded photons increases dramatically by several orders of magnitude. The photon signal is shown in Fig. 6.2 as a function of the time delay after the laser pulse. Direct scattering of the near-infrared beam off the jet surface can not explain such an observation as the MCP has almost zero conversion efficiency for such low photon energies. To efficiently convert and amplify the photon signal into a detectable electron cloud, photon energies above ≈ 3 eV need to be generated. There are three different mechanisms which can lead to such photon up-conversion: harmonic generation, plasma fluorescence and intramolecular fluorescence. A fiber spectrometer from Ocean Optics[210] was used to resolve the spectrum of emitted light in the UV-VIS range. A strong yield of the third and fifth harmonic at the wavelength of 260 nm and

[1] It is noteworthy that the breakage of water hydrogen bonds and subsequent diffusion of molecules do not occur on the ultrashort femtosecond timescales since they are inertial processes. Although the liquid phase might be completely evaporated after interaction with the laser pulse, the electron emission is mainly affected by the instantly ionized liquid medium.

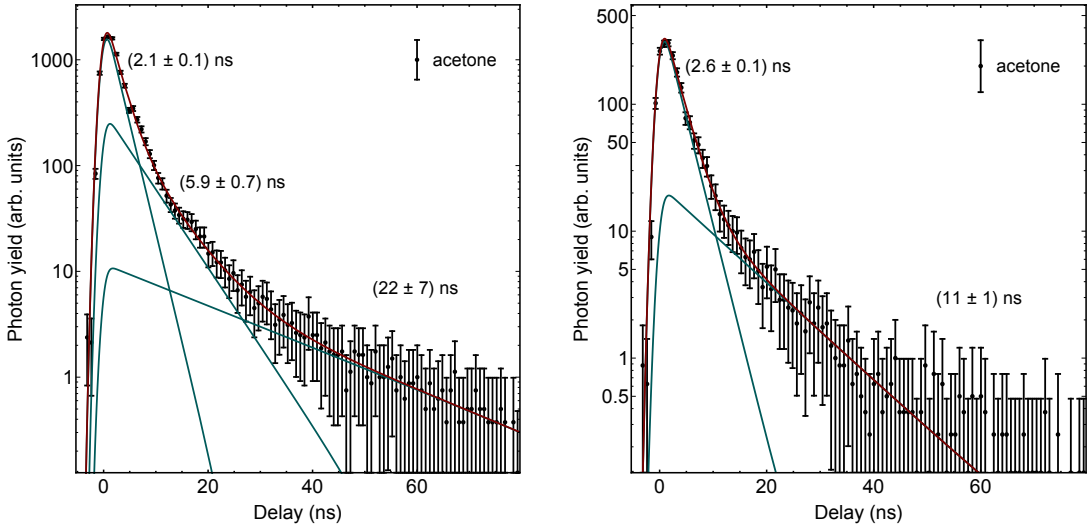

Figure 6.2.: Fluorescence signal of liquid (left) and gaseous (right) acetone as a function of the time delay. Fast components of 2.1 ns and 2.5 ns correspond to intramolecular deexcitation channels while slow components can be identified as plasma deexcitation.

430 nm, respectively, with a rather isotropic angular distribution was detected[2]. The detection of even higher-order harmonics was not possible although even harmonics from liquid samples were already recorded elsewhere[54]. The non-linearity of the photon signal dependency on the laser intensity was, however, not examined, leaving the open question whether the up-conversion was induced in the perturbation regime (i.e. as fifth harmonic generation (FHG)) or in the strong-field regime (i.e. as high harmonic generation (HHG)) where even high-order harmonics should be present. Since harmonic generation occurs within the laser pulse duration, no delay of the photon signal should be observable. On the other hand, fluorescence should yield decaying photon signals with a life time in the order of tens of ps or up to a few µs, where the former time scale is typical for plasma deexcitation by the Coulomb explosion and electron-ion recombination in strongly ionized plasma and the latter is observable in inner-molecular fluorescence and phosphorescence and electron-ion recombination in barely ionized plasma.

In the experiment, the photon signal dynamics where recorded by the MCP detector with a precision of 200 ps. A comparison of this signal for the gas-phase close to the jet and the liquid-phase as a function of the delay is shown in Fig. 6.2. One can see the initial decay on the time scale of 2.5 ns which is a good agreement with reported inner-molecular fluorescence of acetone[211]. Such a fluorescence can be induced with the excitation energy of approximately 4.5 eV[212] for gaseous and 4.6 eV[213] for liquid acetone. This energy matches a resonant five-photon transition from the molecular ground

[2]The seventh harmonic with a wavelength of 185 nm does not propagate through air and the detection optics and, thus, could not be recorded by the spectrometer.

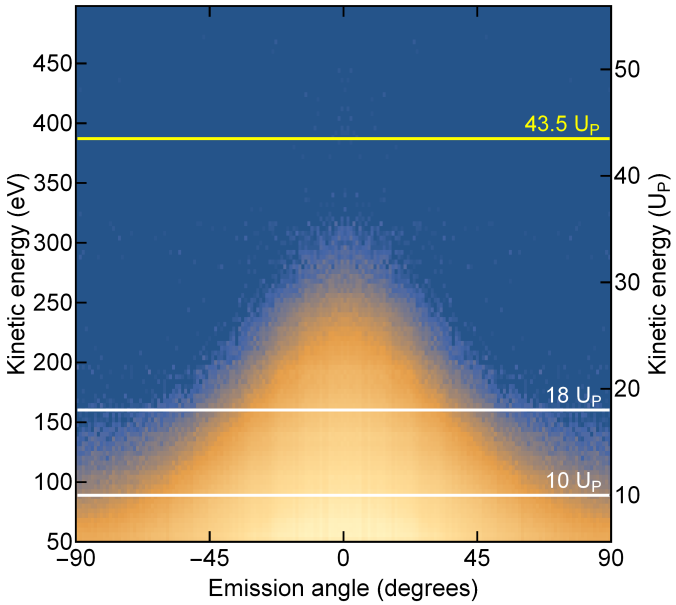

Figure 6.3.: Emission spectrum of liquid acetone in the liquid stabilization region as defined above. An increase of final kinetic energies above the HATI cutoff of $10\,U_P$ and iHATI$^{(1)}$ cutoff of $18\,U_P$ (indicated by solid white lines) is observable. As discussed below the emission following the iHATI$^{(2)}$ ionization path can extend the high-energy cutoff up to $43.5\,U_P$ (solid yellow line) and, thus, yields qualitative agreement with the observed spectrum.

state by employing near-infrared pulses of 0.95 eV photon energy. The slight blue shift and additional broadening of the absorption band in the liquid phase favors the resonant transition and, thus, explains the strong increase of the photon yield upon overlapping the jet and the laser focus. The life time appears to be slightly quenched from 2.6 ns to 2.1 ns due to the interaction of the acetone molecules in the liquid phase. However, the other multi-exponential decay components remain unknown and they appear to strongly correlate with the target density. Accordingly, these fluorescence transition can be attributed to electron-ion recombinations in the laser-generated plasma. As the plasma formation is stronger pronounced at higher target densities, this delayed photon yield increases as well with the increasing overlap of the laser beam and the microjet.

The photon generation in water was found to be much stronger, so that the electron spectrum was strongly affected when probing the liquid phase. Therefore, only results on acetone will be discussed below.

6.2.3. Sequential incoherent scattering

As follows from the results of Sec. 6.2.2, the emission from the liquid phase can not be explained in terms of the iHATI emission described in Sec. 5. The observed kinetic energies above the iHATI cutoff, however, might be an indication for a second subsequent

scattering event of an electron within the ultrashort laser pulse. In the following discussion, the single- and double-scatter event of the iHATI process will be referred to as iHATI$^{(1)}$ and iHATI$^{(2)}$, respectively. In the double-scatter event, the electron is emitted from a parent molecule, oscillates in the laser field until it scatters off a second molecules, and finally moves within the laser field to a third molecule. The initial and the third interacting molecules can also be the same particle. However, the probability that three different molecules are involved in the iHATI$^{(2)}$ process is expected to be high since the EAL in liquids is in the order of a few nm and largely exceeds the intermolecular distance (e.g. $\approx 4\,\mathrm{nm}$ in the case of water). Whereas the density study performed as in Sec. 5.4 facilitated to decompose and characterize the iHATI$^{(1)}$ ionization channel such a procedure is fundamentally impossible in the case of the liquid phase since the medium density can not be varied.

Fig. 6.3 shows the angle-resolved emission spectrum of liquid acetone in the region where the signal is steady (see Sec. 6.2.2). A significant increase of electron yield with final kinetic energy above the iHATI$^{(1)}$ threshold is observable while the overall shape of the spectrum is similar to the iHATI$^{(1)}$ spectrum. In particular, the most intense emission appears along the laser polarization axis and the high-energy cutoff acquires a parabolically decreasing shaped edge at small emission angles. The iHATI$^{(1)}$ cutoff of $18\,U_P$ is violated for emission angles up to 45°, and emission perpendicular to the laser polarization axis is observable up to approximately $15\,U_P$. The iHATI$^{(1)}$ plateau structure is not observable in the spectrum yielding the conclusion that the iHATI$^{(1)}$ ionization path is significantly suppressed or washed out due to electron collisions.

Following the simulation procedure presented in Sec. 5.5, trajectory calculations were performed to estimate the final emission spectrum after the second scattering event while ignoring the return conditions (as discussed in Sec. 2.3.3.2.1).[3] if the potential lanscape of the target sample is structured inclusion of such return conditions is straightforward and can lead to coherence giving rise to interference patterns in the final emission spectrum. Structured periodic samples as crystals should produce strong coherent superpositions of ATI, HATI and iHATI electron trajectories. In such cases, however, quantum-mechanical calculations should be considered to include the phase information of trajectories to reproduce the interference patterns. To retrieve the final emission after the iHATI$^{(2)}$, event one has to apply Eq. (5.9) sequentially. The final emission is, thus, a function of the cosine values of the initial, intermediate and final azimuthal angle, the laser phase during the first and second scatter event and the initial energy of ATI electrons. As in the

[3] Return conditions can play an important role for the iHATI$^{(2)}$ process in the liquid phase. First, the liquid phase is more structured than the randomly ordered gas phase due to the hydrogen bond network. Additionally, revisiting of the parent or the neighboring molecule in the first or final scattering event can yield coherent return conditions as in the case of HATI. For iHATI$^{(1)}$, the only coherent return condition is already included in the HATI description and separated from the incoherent part due to their respective density dependence. As such a study is not possible for the liquid phase, all coherent and incoherent conditions of the iHATI$^{(1)}$ and iHATI$^{(2)}$ process are recorded but only incoherent iHATI$^{(2)}$ trajectories simulated.

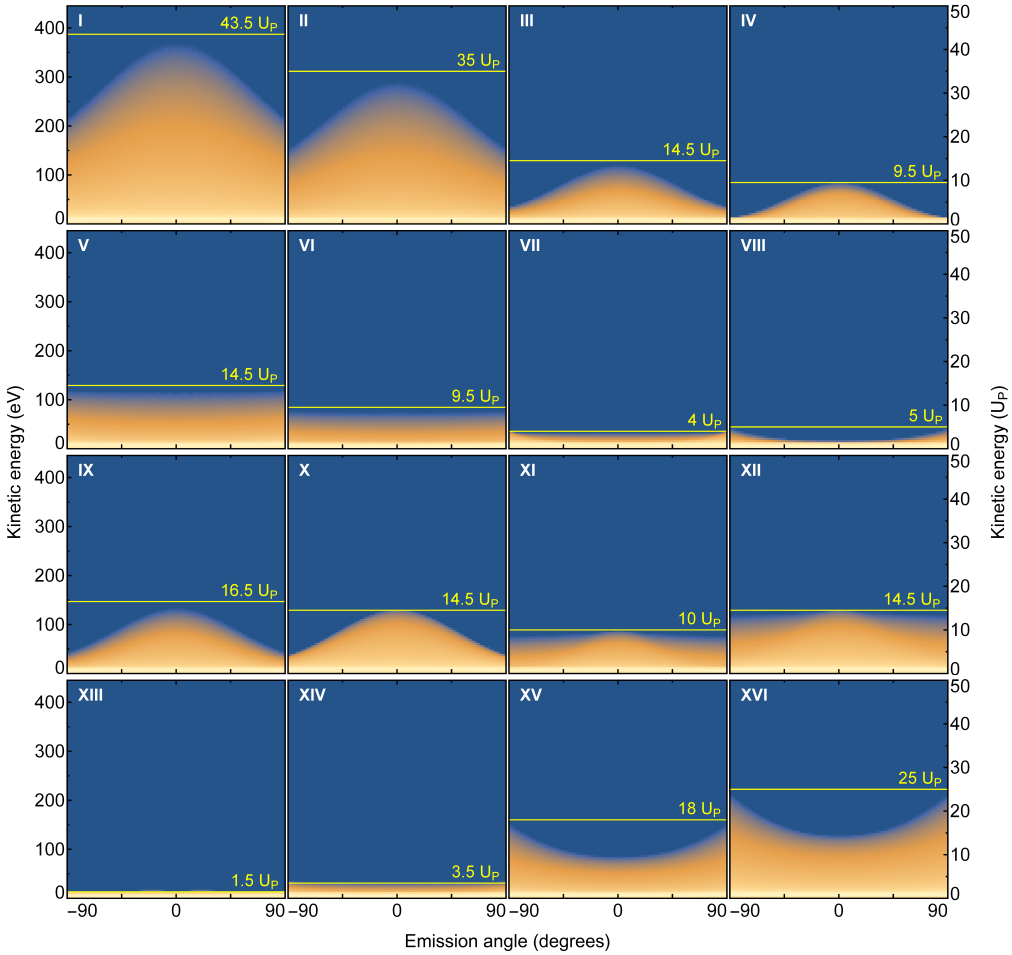

Figure 6.4.: Branches of the iHATI$^{(2)}$ emission. The combination of signs of the cosine values of initial, intermediate and final azimuthal angle as well as of the laser phase at the first and second scattering events produce 16 unique emission spectra with the characteristic plateau structure and high-energy cutoff. The cutoff energies are $43.5\,U_P$, $35\,U_P$, $25\,U_P$, $18\,U_P$, $16.5\,U_P$, $14.5\,U_P$, $10\,U_P$, $9.5\,U_P$, $5\,U_P$, $4\,U_P$, $3.5\,U_P$ and $1.5\,U_P$ in descending order. As in the case of iHATI$^{(1)}$, the emission perpendicular to the laser polarization is at maximum for a few branches.

case of iHATI$^{(1)}$, the different combinations of signs of the cosine values lead to different ionization branches, each producing a plateau-like structure with a specific high-energy cutoff. All branches are twice degenerate, excluding additional degeneracies due to the sign in front of the square root in Eq. (5.4). The respective high-energy cutoff values are $43.5\,U_P$, $35\,U_P$, $25\,U_P$, $18\,U_P$, $16.5\,U_P$, $14.5\,U_P$, $10\,U_P$, $9.5\,U_P$, $5\,U_P$, $4\,U_P$, $3.5\,U_P$ and $1.5\,U_P$ (presented in descending order). These cutoff values do not represent the strict semiclassical high-energy limits of the iHATI$^{(2)}$ plateaus, but the signal amplitude at the semiclassical cutoffs is by more than eight orders of magnitude weaker and lies beyond the signal range shown in Fig. 6.4. One has to point out that several branches exhibit a

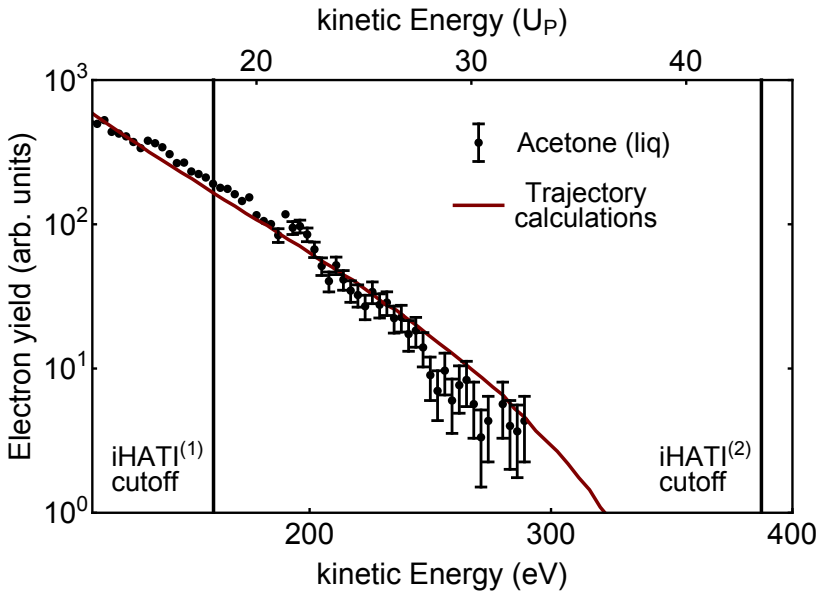

Figure 6.5.: Comparison of experimental data and trajectory calculations. The electron yield is integrated over the emission angles below 10°. The experimental spectrum is well reproduced, though only branch (I) of Fig. 6.4 gives rise to a significant contribution. The multi-plateau structure from other branches is not apparent. As the emission from branch (I) yields a decrease of the ionization yield with increasing kinetic energy of small steepness, the semiclassical cutoff of 43.5 U_P is not observable in the experimental spectrum.

cutoff energy of approximately 15 U_P and 10 U_P. While the latter represents as well the HATI energy cutoff the former is specific for the iHATI$^{(2)}$ case and is neither observable in the HATI nor the iHATI$^{(1)}$ emission. Additionally, strong emission perpendicular to the laser polarization arises up to kinetic energies of 18 U_P or 25 U_P, which are as well characteristic values for the iHATI$^{(2)}$ process as compared to lower-order scattering processes.

Comparison of the simulated and experimental results are shown in Fig. 6.5 which presents the energy dependency of the electron yield integrated over small ($\theta_f < 10°$) emission angles. Overall, the recorded high-energy structure is reproduced by the theory. However, only branch (I) of Fig. 6.3 is found to give significant contribution to the total emission. Thus, the features of the iHATI$^{(1)}$ emission such as a local maximum in electron emission perpendicular to the laser polarization axis and a well-pronounced second plateau are not observable in the iHATI$^{(2)}$ spectrum. This contrast is evident from Fig. 5.10 showing that at least two channels of iHATI$^{(1)}$ were observable and from Fig. 5.5 and Fig. 5.9 that demonstrates the iHATI$^{(1)}$ emission maximum at the final azimuthal angle of 90°. The missing possibility of the density-dependent study and the lack of distinct iHATI$^{(2)}$ emission features except for the extension of the high-energy cutoff, thus, prevents to make a comprehensive characterization of iHATI$^{(2)}$ emission

from the liquid phase.

6.3. Plasma creation by strong laser fields in liquids

The observed plasma fluorescence in Sec. 6.2.2 and the uncertainty outlined above in the characterization of the electron emission from the liquid phase motivate to develop a different approach, which explores the influence of plasma formation on the extreme ultraviolett (XUV) ionization process. To investigate this effect, a pump-probe scheme was employed to study how the interaction with a near-infrared strong pulse modifies the orbital structure of the liquid and gas phase samples probed by means of XUV photoemission spectroscopy.

6.3.1. Experimental conditions

In this study experimental setup experimental setup 1 (E1) was used in combination with spectrometer spectrometer 1 (S1) (see Fig. 5.1(a)).

Linearly polarized near-infrared laser pulses of 40 fs pulse duration and central wavelength of 1400 nm were focused by a spherical lens into the experimental chamber into a focal spot of approximately 25 µm. The pulse energy was attenuated to 8 µJ yielding a laser peak intensity of approximately $3 \times 10^{13}\,\mathrm{W\,cm^{-2}}$ and giving rise to the ponderomotive energy of 6 eV. The beam polarization axis was controlled by the use of a waveplate allowing angle-resolved measurements.

The target represents the liquid phase of a 20 µm ethanol microjet. A small concentration (20 mM) of NaI was added to the purified ethanol to avoid streaming potentials[164].

6.3.2. Plasma formation and partial dissipation

Upon interaction with the strong infrared laser pulse, the accumulation of quasi-free charges can lead to the formation of a plasma in the laser focus. The generation of such plasmas appears on the time scale of a few fs up to ns and, thus, is accessible by pump-probe schemes. The electronic state of the target sample is monitored by the XUV light of 32.6 eV (see Sec. 3.3.3), mapping the valence band structure of neutral ethanol in the liquid and gas phase into the continuum electron spectrum via single-photon ionization. Ionization from higher-charge states are not accessible due to the insufficient photon energy[214, 215]. The time evolution of charge accumulation and dissipation is monitored by recording the XUV photoelectron spectrum as a function of the delay between the strong-laser-pump and the XUV probe pulses.

The dependency of spectra generated by the two-color interaction on the time delay is shown in the upper panel of Fig. 6.6. Here the vertical axis represents the kinetic energy of photoelectrons. For negative time delays (probe pulse arrives first to the interaction region), the emission spectrum appears similar to the single-color XUV

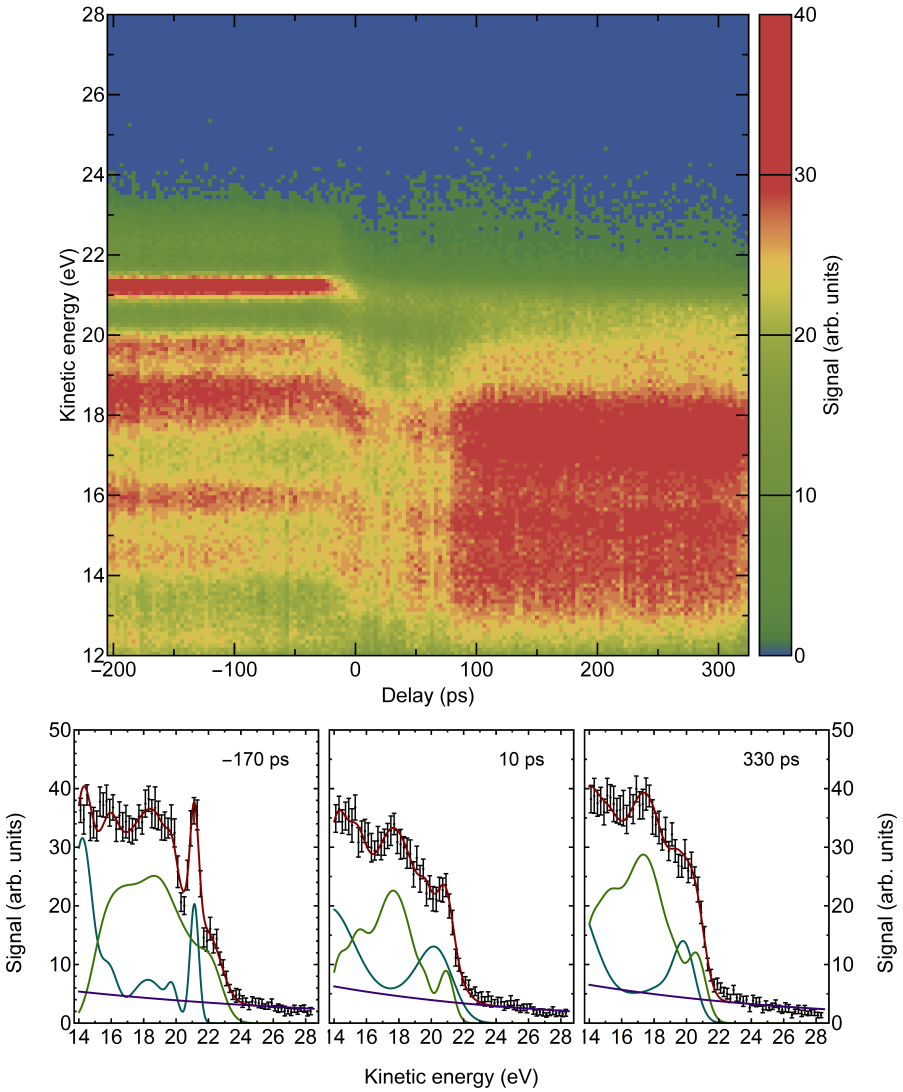

Figure 6.6.: Upper panel: Transient photoemission map of ethanol excited by strong infrared pulses and probed by XUV light. Negative delays denote that the photoexcitation happens after the probe light maps the orbital structure into continuum states. Upon overlapping both pulses in time a strong variation of the electronic structure of ethanol is observable. After ≈80 ps the photoemission stabilizes in a meta-stable configuration. After excitation the orbital structure is significantly distorted in the recorded delay interval up to 300 ps. Lower panels: Spectral emission and corresponding fit by a superposition of Gaussian functions (XUV emission of gaseous and liquid ethanol) and exponential function (ATI emission) at three characteristic delay positions.

spectrum (not shown) and, thus, mostly represents a superposition of the liquid- and gas-phase XUV emission of ethanol. Two remarkable features are the sharp emission peak of gaseous ethanol between 21 eV and 22 eV and the highest-lying emission band of liquid ethanol between 22 eV and 24 eV. The negative time delay spectra were fitted by

to a superposition of a number of Gaussian profiles representing emission bands from the liquid- and gas-phase orbitals. The relative amplitudes and widths of these bands are in agreement with a previous photoemission study at a similar photon energy[158]. The fit analysis revealed that the spectrum obtained at negative time delays and the single-color XUV spectrum differ only by a linear onset originating from the strong-field ATI spectrum, which was also included into the fit routine. In the considered kinetic range, the ATI spectrum was found to exhibit an exponential decay with the increase of the kinetic energy. The decomposition of ATI and XUV emission spectra will be considered in more detail below.

At shorter time delays between the pump and probe beams the photoelectron spectrum is affected by the SCE[208]. The "negative SCE" (following the notation in the mentioned reference) due to electron-electron interaction appears to be negligible for the given pump wavelength and intensity and only the "positive SCE" is observable, shifting the emission spectrum towards lower kinetic energies due to the ion-electron attraction. However, the SCE is not the major effect in the present study. Upon overlapping the pump and probe pulses in time the emission spectrum is strongly affected by another non-linear response to the two-color interaction. For positive delays larger than 85 ps (pump pulse arrives first), the XUV emission appears to be stabilized within the shown time delay range. But this stabilized spectrum is not the same as before the interaction with the pump beam, evidencing changes induces in the sample by the strong laser field. To further investigate this influence, the above-mentioned fitting procedure was applied to derive the spectral broadening and narrowing, the signal enhancement and decrease, and the emission band shifts as a function of the time delay. The decomposition of the ATI, gas- and liquid-phase signal obtained from the fit, is shown in the lower panel of Fig. 6.6 for three representative delays: at a negative delay of −170 ps where the XUV spectrum is nearly unperturbed, at a short delay of 10 ps where the perturbation by strong-field ionization is maximal, and at a longer time delay of 330 ps where the XUV spectrum is stabilized.

Performing this decomposition for all recorded delays allows to trace the evolution of the charge accumulation in the interaction region. The results of this fitting routine are summarized in Fig. 6.7. As mentioned before, the nonlinear response can be separated according to three characteristic delay intervals. For negative delays, the SCE gives rise to a slight broadening of 0.1 eV of the emission band of liquid and gaseous ethanol and to a shift of the spectrum by 0.2 eV and 0.8 eV for the gas and the liquid phase, respectively. It also leads to a strong signal decrease for the gas emission and to a signal increase from the liquid phase, which is rather counter-intuitive for such time-scales and probably has a different origin than the SCE. However, the weaker signal-to-noise ratio prevents to make a clear interpretation of the electron yield increase from the liquid phase. All spectral changes due to the SCE appear on the same time scale of approximately −50 ps to 0 ps and, thus, show a strong correlation. Although the positive SCE is present

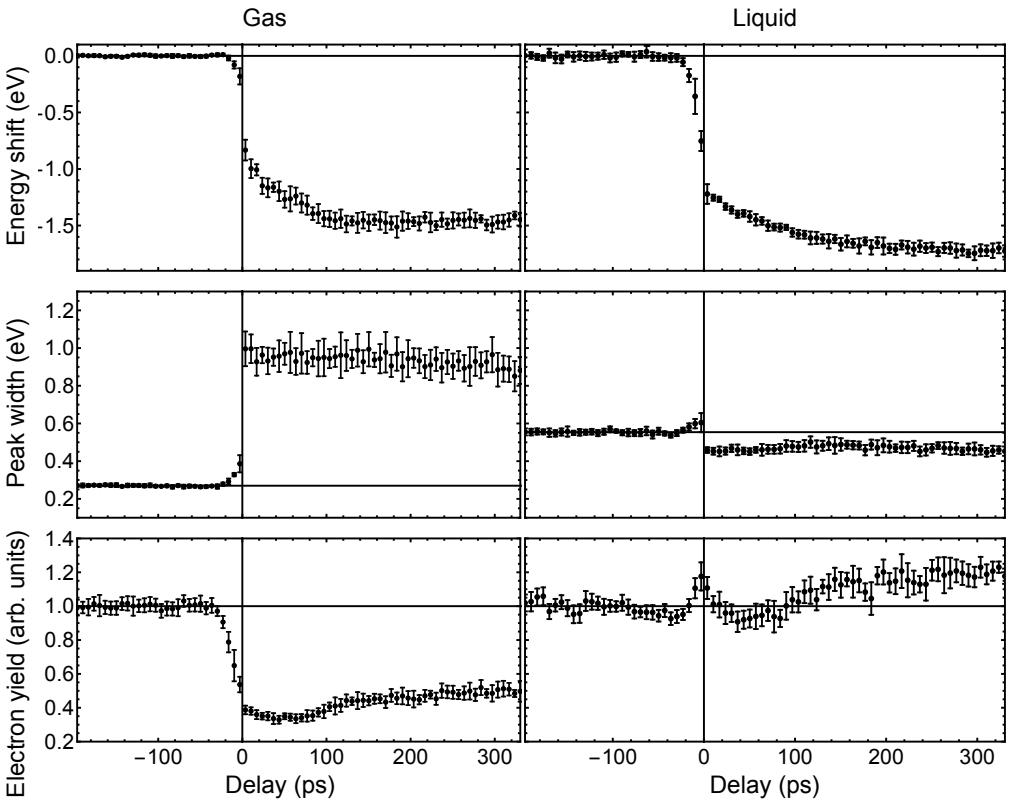

Figure 6.7.: Energy shift, emission width, and electron yield plotted as a function of the delay for liquid and gas-phase emission. A significant change of the emission is observable upon illuminating the ethanol microjet with the strong infrared laser. Different phases of sample excitation are observable. At low (negative) delays the emission spectrum appears unaffected, upon reducing the delay between pump and proble beams the SCE shifts and broadens the spectrum. For positive delays the emission appears not to stabilize within the first 80 ps.

for positive delays as well, other effects appear to to be important in this delay range. Up to approximately 120 ps, the spectrum undergoes a tremendous change manifesting in a strong and continuously increasing shift of the gas- and liquid-phase spectra by approximately 1.5 eV. According to earlier reports of the SCE [208, 207], the largest shift should be observable for smaller delays in the order of a few ps and, thus, these contradicting findings suggest an additional indirect laser-driven charge increase. As the spectral bandwidths in the emission spectrum from the gas-phase spectrum appear constant and only changes in the bandwidth of the liquid phase is observable, the origin of the charge increase has to lie in laser-induced but retarded autoionization[216] processes in the liquid phase. Such a behavior was already observed and interpreted in terms of hot electron production and secondary ionization[46] and by acoustic waves[217, 47]. During this early-time period, the emission from the liquid phase first slightly decreases but later recovers back, suggesting a rearrangement of the intra-molecular structure. After rearrangement of the macroscopic structure, the liquid phase stabilizes for hundreds of

ps and, thus, fluorescence becomes the main relaxation channel observable in the photon emission study (see Fig. 6.2.2). The most probable explanation for such a behavior is the formation (at early delay up to a few tens of ps) and dissipation (at large delays up to a few ns) of a plasma in the initially liquid phase. As the high-charged states of ethanol or its dissociated ion products could not be detected with the used photon energy[215], the plasma generation remains an open subject for further investigations.

6.3.3. Plasma oscillations

As previously reported[52, 53], laser-driven plasma generation can affect the photoelectron spectrum by periodic broadening of individual emission bands. The frequency of such oscillations has to match the Langmuir[218] frequency, ω_{P}:

$$\omega_{\mathrm{P}} = \sqrt{\frac{e^2 n_e}{\epsilon_0 m_{\mathrm{e}}}} \quad , \tag{6.1}$$

where e and m_{e} represent the electron charge and mass, respectively, n_e is the electron number density and ϵ_0 is the vacuum permittivity. Thus, observation of oscillations can yield essential information on the formation and dissipation of plasma generated by intense laser pulses. For experimental conditions given in Sec. 6.3.2, such an oscillatory behavior was not distinguishable. However, upon increasing the laser intensity by a factor of 2 and switching the operation mode of the spectrometer from the 'drift mode' to the 'wide-angle mode', several emission features altered by oscillations were recorded. Under these conditions the full valence band structure of ethanol could not be recorded, so that a comparison with the results from Sec. 6.3.2 is not possible. Also, the experimental conditions were less stable, making the reproducibility of observed results harder.

A typical train of oscillations in the partial electron yield is presented in Fig. 6.8 which shows the integrated electron yield just above the highest lying emission band of liquid ethanol. There are two remarkable changes due to the interaction with the strong infrared laser field. First, the ionization yield of the high-energy tail of the liquid ethanol spectrum is significantly decreased, which is in agreement with results presented in Sec. 6.3.2, and can be explained by the SCE and/or the rearrangement of molecules close to the plasma region. Second, a periodic increase of the signal with a period of approximately 40 ps is observable. This signal increase can be explained by the plasmonic electron motion and the resulting broadening of the photoemission bands of interacting liquid and gaseous molecules. As mentioned before, direct observation of highly-charged positive ions in the plasma is not possible due to the insufficient XUV photon energy[215]. The observed frequency of 38 ps is significantly larger than the previously reported value of 1.5 ps[52, 53] obtained at similar experimental conditions. From Eq. (6.1), the found frequency corresponds to an electron density of $8 \times 10^{12}\,\mathrm{cm}^{-3}$. Additionally, a dephasing of the electron motion, which would result in a decrease of the oscillatory signal and a

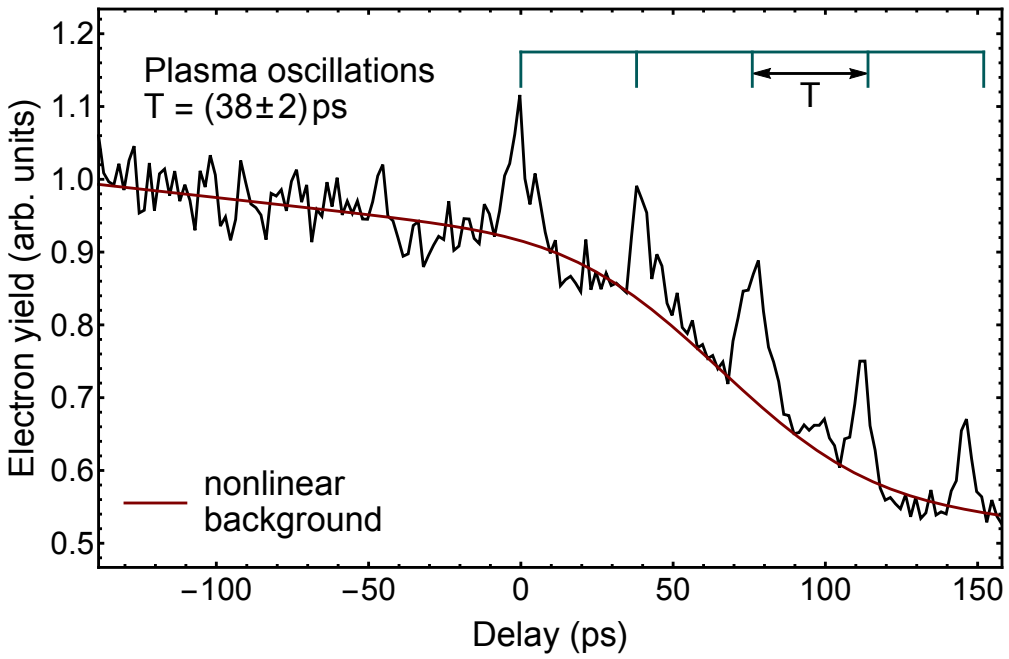

Figure 6.8.: Plasma oscillations in the photoemission yield just above the highest lying ionization pathway as a function of the delay between photoexcitation by the strong-field laser and ionization by the XUV pulses. The SCE introduces a large change in the total emission. However, in addition discrete periodic emission enhancements are observable. These peaks in the emission yield can appear if plasma oscillations affect the emission spectrum of the sample (e.g. broadening of emission bands).

broadening of the ionization yield peaks in the delay domain, was not observable. These findings lead to the conclusion that the observed plasma has a lower charge state and appears more stable than previously reported. The origin of this behavior, however, remains an open question for further studies.

Summarizing this section, the application of transient XUV photoemission spectroscopy represents a powerful tool to study the laser plasma dynamics created in the liquid phase by means of ionization in a strong laser field. The potential of this method is demonstrated in the first experiment in this work, and it opens a wide range of future applications.

7. Side project: Development of Numerical Methods of Data Evaluation for Transient Photoelectron Spectroscopy

The numerical methods develped in this work enabled the analysis of experimental data obtained by means of transient photoelectron spectroscopy. Their application gave a significant contribution to the published articles:

Kothe *et al.* Phys. Chem. Chem. Phys., **17**, 1918-1924 (2015), doi:10.1039/C4CP02482F (Ref. [171]),
Kothe *et al.* Phys. Chem. Chem. Phys., **17**, 18195-18196 (2015), doi:10.1039/C5CP01804H (Ref. [219]),
Borgwardt *et al.* J. Phys. Chem. C, **119**, 9099-9107 (2015), doi:10.1021/acs.jpcc.5b01216 (Ref. [220]),
Borgwardt *et al.* Proceedings EUPVSEC (2015), doi:10.4229/EUPVSEC20152015-1AO.1.2 (Ref. [221]),
Borgwardt *et al.* Sci. Rep., **6**, 24422 (2016), doi:10.1038/srep24422 (Ref. [222]),
Borgwardt *et al.* Phys. Chem. Chem. Phys., **18**, 28893-28900 (2016), doi:10.1039/C6CP05655E (Ref. [223]),
Moguilevski *et al.* ChemPhysChem, **18** 465-469 (2017), doi:10.1002/cphc.201601396 (Ref. [224])

7.1. Introduction

Two-color transient photoelectron spectroscopy represents one of the fundamental methods to study electronic structure and dynamics of molecules and compounds. In this studies, the pump photons initiate photoexcitation of the regarded system and the probe photons of sufficiently high energy map the electronic population distribution among the ground and excited states into the detectable free-electron (continuum) states in the process of photoionization. By varying the delay between the pump and probe photons, the dynamic evolution of the system can be revealed. To enable the characterization of these dynamics with a high time resolution, the duration of the pump and probe light pulses should be significantly smaller than the dynamics time scale. Due to the Heisenberg's uncertainty principle investigation of ultra-fast processes (below 100 fs) are, however,

not possible without a loss of information on the energy scale, related to a reduced energy resolution of the electronic structure. For example, generation of optical pump pulses as short as 3 fs requires a spectral bandwidth of 500 nm at a central wavelength of 650 nm[225]. Although such pulses carry well-defined information on the timescale, the broad spectrum on the energyscale typically does not allow to study specific excitation mechanisms but leads to excitations of all channels within the pump spectrum.

However, it is possible to describe photoexcitation and relaxation mechanisms of a quantum system even when the finite duration of the pump and probe pulses is of the order of the characteristic time of deexcitation dynamics. Such a description is based in the development of kinetic models. Following this approach the analytical description of the deexcitation mechanism is less straightforward and possibly only numerically solvable, but the dynamics time scale and the electronic structure can be reconstructed.

7.2. Time-evolution of photoexcited weakly-coupled multi-state systems

A system of n weakly-coupled energetically ordered states, $|\boldsymbol{n}\rangle = \{n_0, n_1, \ldots, n_{n-1}\}$ (where n_0 denotes the highest excited state and n_{n-1} is the ground state), with the time-dependent population of states $|\boldsymbol{p}(t)\rangle = \{p_0(t), p_1(t), \ldots, p_{n-1}(t)\}$ can be described by the Pauli Master Equation (PME). This equation follows directly out of the time-dependent Schrödinger equation (TDSE) by applying the perturbation theory[226]:

$$\frac{\mathrm{d}|\boldsymbol{p}(t)\rangle}{\mathrm{d}t} = \mathcal{W}\,|\boldsymbol{p}(t)\rangle \quad , \tag{7.1}$$

where the evolution matrix $\mathcal{W}$ consists of three terms:

$$\mathcal{W} = \mathcal{P} + \mathcal{L} - \mathcal{D} \tag{7.2}$$

with

$$(\mathcal{P})_{i,j} = k_{i,j}(1 - \delta_{i,j}) \qquad \text{(population)} \tag{7.3}$$

$$(\mathcal{L})_{i,j} = A_{i,j}(t)(1 - \delta_{i,j}) \qquad \text{(photoexcitation)} \tag{7.4}$$

$$(\mathcal{D})_{i,j} = \sum_{m=0}^{n-1} k_{i,m}\delta_{i,j} \qquad \text{(decay.)} \tag{7.5}$$

Here $k_{i,j}$ denotes the transition amplitude from state n_i to state n_j and $A_{i,j}(t) = -A_{j,i}(t)$ is the (time-dependent) photoexcitation amplitude. Typically for photexcitation dynamics induced by visible or UV light in molecular systems, photoexcitation is considered to take place only from the ground state n_{n-1} to the highest excited state n_0 ($A_{i,j}(t) = A(t)(\delta_{i,0}\delta_{j,n-1} - \delta_{i,n-1}\delta_{j,n-1})$) and the transitions between excited states have a relaxation character, meaning that $k_{i,j} \gg k_{j,i}$ for a state n_i lying at a higher energy level than n_j ($j > i$). Hence, neglecting insignificant terms the representation of the

above-mentioned matrices reads:

$$\mathcal{P} = \begin{pmatrix} 0 & 0 & \cdots & 0 & 0 & 0 \\ k_{0,1} & 0 & \cdots & 0 & 0 & 0 \\ k_{0,2} & k_{1,2} & \cdots & 0 & 0 & 0 \\ \vdots & \vdots & \ddots & \vdots & \vdots & \vdots \\ k_{0,n-2} & k_{1,n-2} & \cdots & k_{n-3,n-2} & 0 & 0 \\ k_{0,n-1} & k_{1,n-1} & \cdots & k_{n-3,n-1} & k_{n-2,n-1} & 0 \end{pmatrix} \tag{7.6}$$

$$\mathcal{L} = \begin{pmatrix} 0 & 0 & \cdots & 0 & A(t) \\ 0 & 0 & \cdots & 0 & 0 \\ \vdots & \vdots & \ddots & \vdots & \vdots \\ 0 & 0 & \cdots & 0 & 0 \\ 0 & 0 & \cdots & 0 & -A(t) \end{pmatrix} \tag{7.7}$$

$$\mathcal{D} = \begin{pmatrix} 1/\tau_0 & 0 & \cdots & 0 & 0 \\ 0 & 1/\tau_1 & \cdots & 0 & 0 \\ \vdots & \vdots & \ddots & \vdots & \vdots \\ 0 & 0 & \cdots & 1/\tau_{n-1} & 0 \\ 0 & 0 & \cdots & 0 & 0 \end{pmatrix} \tag{7.8}$$

where $\tau_i = \left(\sum_{m=i+1}^{n-1} k_{i,m}\right)^{-1}$ denotes the lifetime of the state n_i.

The resulting system of differential equations can be solved numerically by employing the explicit Runge-Kutta algorithm (backward finite differences), although a simple Euler approach (single-stage Runge-Kutta) is typically sufficient and reduces the computation time per evaluation significantly without compromising the accuracy. The time evolution, then, is described by the recursive formula:

$$|\boldsymbol{p}(t+h)\rangle = |\boldsymbol{p}(t)\rangle + h\mathcal{W}\,|\boldsymbol{p}(t)\rangle \tag{7.9}$$

$$= (\mathbf{I} + h\mathcal{W})\,|\boldsymbol{p}(t)\rangle \tag{7.10}$$

where $\mathbf{I}$ is the identity matrix and h represents the time evolution step which has to be much shorter than the characteristic time of any involved transition ($h \ll 1/k_{i,j}$). Typically, the initial condition is represented as $p_i(t \to -\infty) = \delta_{i,n-1}$, implying that the system is initially in the ground state.

7.3. Inclusion of the photoionization process

Photoionization by the probe pulse promotes electrons from the transiently populated bound states $|\boldsymbol{n}\rangle$ into the continuum free states $|\boldsymbol{n'}\rangle$ and is represented by another term,

$\mathfrak{X}$, in the PME. The photoionization matrix $\mathfrak{X}$, thus, has only non-diagonal entries connecting the corresponding bound and free states:

$$|\boldsymbol{nn'}\rangle = |\boldsymbol{n}\rangle \otimes |\boldsymbol{n'}\rangle = \{n_0, n_1, \ldots, n_{n-1}, n'_0, n'_1, \ldots, n'_{n-1}\} \tag{7.11}$$

$$|\boldsymbol{pp'}(t)\rangle = |\boldsymbol{p}(t)\rangle \otimes |\boldsymbol{p'}(t)\rangle = \{p_0(t), p_1(t), \ldots, p_{n-1}(t), p'_0(t), p'_1(t), \ldots, p'_{n-1}(t)\} \tag{7.12}$$

$$(\mathfrak{X})_{i,j} = B_{\min\{i,j\}}(t, \Delta t)(\delta_{i,j+n} - \delta_{i+n,j}) \tag{7.13}$$

$$\mathfrak{X} = \begin{pmatrix} 0 & 0 & \cdots & 0 & 0 & -B_0(t) & 0 & \cdots & 0 & 0 \\ 0 & 0 & \cdots & 0 & 0 & 0 & -B_1(t) & \cdots & 0 & 0 \\ \vdots & \vdots & & \vdots & \vdots & \vdots & \vdots & & \vdots & \vdots \\ 0 & 0 & \cdots & 0 & 0 & 0 & 0 & \cdots & -B_{n-2}(t) & 0 \\ 0 & 0 & \cdots & 0 & 0 & 0 & 0 & \cdots & 0 & -B_{n-1}(t) \\ B_0(t) & 0 & \cdots & 0 & 0 & 0 & 0 & \cdots & 0 & 0 \\ 0 & B_1(t) & \cdots & 0 & 0 & 0 & 0 & \cdots & 0 & 0 \\ \vdots & \vdots & & \vdots & \vdots & \vdots & \vdots & & \vdots & \vdots \\ 0 & 0 & \cdots & B_{n-2}(t) & 0 & 0 & 0 & \cdots & 0 & 0 \\ 0 & 0 & \cdots & 0 & B_{n-1}(t) & 0 & 0 & \cdots & 0 & 0 \end{pmatrix} , \tag{7.14}$$

where $B_i(t, \Delta t)$ represents the ionization rate of the ith state as a function of the delay Δt between the photoexcitation and photoionization process. The evolution matrix has the form:

$$\mathcal{W}' = \mathcal{W} + \mathfrak{X} \quad , \tag{7.15}$$

where $\mathcal{W}$ is the evolution matrix without interaction with the probe pulse (see Eq. (7.2)). The population dynamics are described by the recursive formula:

$$|\boldsymbol{pp'}(t+h)\rangle = |\boldsymbol{p}(t)\rangle + h\mathcal{W}' |\boldsymbol{pp'}(t)\rangle \tag{7.16}$$

$$= (\mathbf{I} + h\mathcal{W}') |\boldsymbol{pp'}(t)\rangle \quad , \tag{7.17}$$

where $|\boldsymbol{n}\rangle'$ and $|\boldsymbol{p}(t)\rangle'$ describe the set of bound and ionized states and their respective populations. The ionized electron population $|\boldsymbol{p'}(t)\rangle$ is initially set to zero and the observable of the experiment (electron signal) represents the population of the ionized states in the limit $t \to \infty$. The additional elements of the matrices $\mathcal{P}$, $\mathcal{L}$, and $\mathcal{D}$ due to the inclusion of the ionized states remain zero as there are no further interactions of ionized and bound states.

7.4. Global fit routine of a multi-state system

Each state n_i yields its own emission spectrum after photoionization. This emission spectrum can be either modeled by a number of Gaussian components or can be derived from the transient emission map by employing the least squares algorithm.

The acquired transient photoelectron yield of a photoexcited system as a function

of kinetic energy and time yields a data matrix, $\mathcal{Y}$, of dimensionality $(t \times e)$, where t denotes the number of sampled time delays and e is the number of sampled energies. Under the assumption that the shape of the emission spectrum of each particular state is time-independent and the time-evolution of a given state is energy (band) independent, the data matrix can be decomposed into the spectrum matrix, $\mathcal{E}(n \times e)$, and the time matrix, $\mathcal{T}(n \times t)$ such that:

$$\mathcal{Y} = \mathcal{T}^{\mathrm{T}}\mathcal{E} \tag{7.18}$$

where $(\cdot)^{\mathrm{T}}$ denotes the matrix transposition.

7.4.1. Spectral decomposition by the least squares algorithm

When the time matrix is evaluated by sampling, represented by Eq. (7.17) at the recorded delay positions, the spectrum matrix can be reconstructed by:

$$\mathcal{E} = \left(\mathcal{T}\mathcal{T}^{\mathrm{T}}\right)^{-1}\mathcal{T}\mathcal{Y} \tag{7.19}$$

This equation is obtained via multiplying Eq. (7.18) with $\left(\mathcal{T}\mathcal{T}^{\mathrm{T}}\right)^{-1}\mathcal{T}$ on the left side, where $(\cdot)^{-1}$ denotes the matrix inversion.

However, the experimental data matrix, $\mathcal{Y}'$, is typically superimposed with the noise represented by the noise matrix, $\mathcal{N}$, and the reconstruction of the emission spectrum has to follow the least squares algorithm, e.g. by multiplying with the Moore-Penrose pseudoinverse denoted as $(\cdot)^{+}$:

$$\mathcal{Y}' = \mathcal{Y} + \mathcal{N} \tag{7.20}$$

$$\mathcal{E}' = \mathcal{T}^{+}\mathcal{Y}' \tag{7.21}$$

The reconstruction of the experimental energy matrix $\mathcal{E}'$ yields better agreement (the least squares algorithm yields less residuals) if the time matrix $\mathcal{T}$ is chosen properly. Thus, the fit quality is given by:

$$\chi^2 = \left\| \frac{\mathcal{T}^{+}\mathcal{Y}' - \mathcal{Y}'}{\mathcal{S}} \right\|_{\mathrm{F}}^2 \tag{7.22}$$

where $\|\cdot\|_{\mathrm{F}}$ denotes the Frobenius-Norm and $\mathcal{S}$ represents the uncertainty (error) in the measurement of $\mathcal{Y}'$.

This approach requires only those fitting parameters which are necessary to describe and to solve the PME (i.e. all $k_{i,j}$ and $A(t)$). However, it yields an unphysical (noisy) emission spectrum $\mathcal{E}'$.

7.4.2. Spectral decomposition by the Gaussian fits

A more restricted but physically more meaningful approach consists in the simultaneous fit of $\mathcal{T}$ and $\mathcal{E}$ by employing the PME and by considering superposition of a number of Gaussian (Lorentzian) emission lines, respectively. In this approach, the matrix $\mathcal{E}$ represents the sampled description of the emission of each state. The fit quality, which is minimized by the fitting routine, reads:

$$\chi^2 = \left\| \frac{\mathcal{E}\mathcal{T} - \mathcal{Y}'}{\mathcal{S}} \right\|_{\mathrm{F}}^2 \tag{7.23}$$

where $\mathcal{S}$ represents the uncertainty (error) in the measurement of $\mathcal{Y}'$.

This approach requires more fitting parameters than the above-mentioned least-squares routine. Additionally to those parameters which are required to describe and solve the PME (i.e. all $k_{i,j}$ and $A(t)$), all parameters describing $\mathcal{E}$ need to be fitted. Nevertheless, the fitted emission spectrum $\mathcal{E}$ yields more physical meaning than the least-squares method.

7.5. Stepwise regression employing F-test validation

In order to obtain the simplest model which is sufficient to explain the recorded data, a stepwise regression can be employed. Here the goodness of fit of a restricted (χ_1^2) and an unrestricted (χ_2^2) model is compared. If the improvement of the goodness of fit is significant with respect to the amount of additional fit parameters (p_1 compared to p_2) involved in the unrestricted model, the restricted model needs to be discarded and the unrestricted model accepted. By decreasing (increasing) the restriction (fit parameter), the stepwise regression method yields the model with the best agreement while discarding unnecessary fit parameters. The improvement of the unrestricted model can be tested by calculating the F-test value:

$$F = \frac{\chi_1^2 - \chi_2^2}{p_2 - p_1} \frac{n - p_2}{\chi_2^2} \tag{7.24}$$

and comparing it to the critical value of the F-distribution for a given significance level (typically of the order of 95 %). Here n represents the number of samples acquired in the experimental data.

7.6. Application to the description of ultrafast electron dynamics following molecular photoexcitation

In the description of the photo-excitation and -ionization processes, one often uses the assumption that either photoionization or (more often) photoexcitation takes place

instantaneously. This assumption simplifies the inclusion of the experimental time resolution by a simple convolution. Another simplification follows from the assumption of instant population of all regarded states in parallel while disregarding all deexcitation channels except for those connecting each state with the ground state. Typical examples of such approximations can be found in recent publications[227, 228, 229]. However, a complete description of the deexcitation channels together with photo-excitation and -ionization processes yields essential information, especially when the duration of pump and probe pulses is comparable to the characteristic time scale of the electron dynamics of the photoexcited molecular system [230]. The numerical method presented in this chapter was employed as a tool to understand the deexcitation mechanism in photoexcited molecules. Some examples will be briefly presented below. A comprehensive discussion of the results can be found in the respective publications.

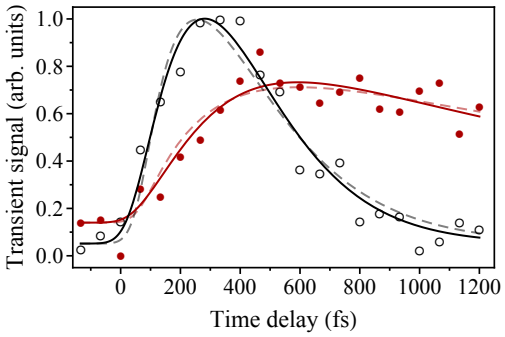

Figure 7.1.: Delayed population of two charge-transfer-to-solvent states.[219] Experimental data (dots) of the photoionization yield of both states as a function of the delay were compared to two models including (solid) and excluding (dashed) an intermediate state. Statistical analysis of the fitting routine proves the existence of the intermediate state.

In [Kothe *et al.* 2015 *Phys. Chem. Chem. Phys.* **17** 1918] (Ref. [171]) and [Kothe *et al.* 2015 *Phys. Chem. Chem. Phys.* **17** 18195] (Ref. [219]), the numerical method revealed the existence of an intermediate state with a small photoionization rate, whereas this state was shown to delay the population dynamics of the detected transient charge-transfer-to-solvent states (see Fig. 7.1). Not only the presence of another state was shown, but its life time was also characterized.

In [Borgwardt *et al.* 2015 *J. Phys. Chem. C* **17** 119] (Ref. [220]), the charge transfer from a dye to the surface of a semiconductor was studied. The ultrafast injection pathway into the semiconductor conduction band (CB) was shown to only exist in the case of the TiO_2 semiconductor-interface, giving rise to an overall higher efficiency of the corresponding photocell (see Fig. 7.2) . The application of the numerical solution of the PME allowed the estimation of lifetimes (< 30 fs) smaller than the system response (≈ 100 fs).

In [Moguilevski *et al.* 2017 *ChemPhysChem* **18** 465] (Ref. [224]) the deexcitation

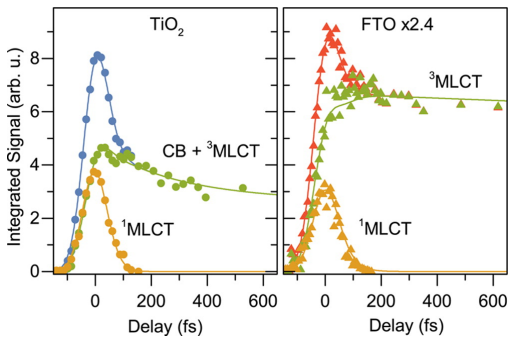

Figure 7.2.: Charge-transfer dynamics of excited states (^{1}MLCT, ^{3}MLCT, and CB) at the semiconductor-dye interfaces of TiO_2 and FTO.[220] The ultrafast injection mechanism (into the CB state), yielding a higher efficiency of the photovoltaic system, is only observable in the TiO_2 interface. Injection on the FTO surface only occurs via the ^{3}MLCT state which yields overall a slower injection dynamic.

mechanism of a photoexcited molecule of iron tris-bipyridine was studied, where earlier publications reported two contradicting deexcitation channels. Application of the above-mentioned numerical methods including the description a parallel deexcitation proved the coexistence of both previously reported models (see Fig. 7.3). Additionally to the corresponding life times, the branching ratio of the two deexcitation channels was obtained. By employing the least-square decomposition (see Sec. 7.4.1) and a comprehensive F-statistics analysis, a number of different deexcitation models were fitted and the parallel deexcitation was shown to be favorable. Spectral decomposition by Gaussian lines (see Sec. 7.4.2) yielded the emission spectrum of each observed state, which electronic structure was, accordingly, assigned with the aid of theoretical calculations.

In [Borgwardt *et al.* 2016 *Phys. Chem. Chem. Phys.* **18** 2016] (Ref. [223]) it was unambiguously shown that a spin-transition and subsequent vibrational cooling in a dye molecule solved in ionic liquids after photoexcitation are apparent (see Fig. 7.4). Again, life times below the temporal resolution of the experimental apparatus were obtained and were shown to be in agreement with literature values.

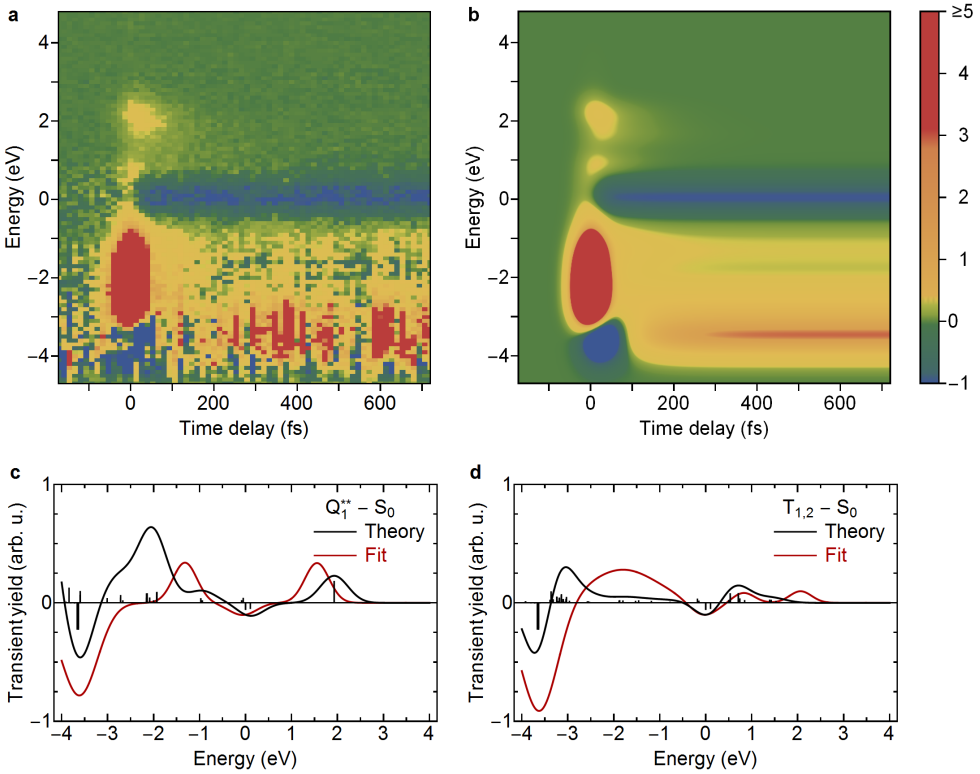

Figure 7.3.: Transient photoionization yield recorded in the experiment (a) and the global fit result (b) as a function of kinetic energy and delay.[224] (c) and (d) represent the emission spectra for two of the regarded states obtained by the global fit routine including spectral decomposition by Gaussian fits (see Sec. 7.4.2). Comparison with theoretical calculations reveal the electronic structure of the observed excited states (Q_1^{**} and $T_{1,2}$) indicating the parallel deexcitation.

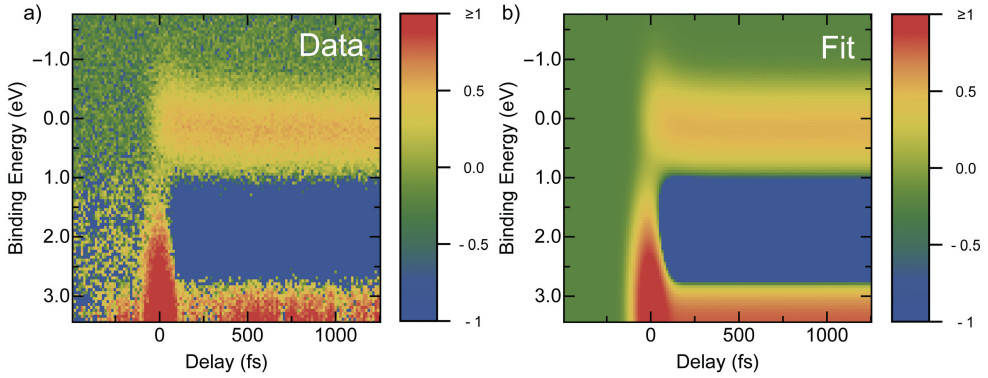

Figure 7.4.: Transient photoionization yield recorded in the experiment (a) and the global fit result (b) as a function of kinetic energy and delay.[223] The global fit routine including spectral decomposition by a superposition of Gaussian emission lines (see Sec. 7.4.2) allowed to identify the deexcitation pathway.

8. Summary

In this work the collective effects occurring during strong-field–matter interaction in dense media was studied by means of single-color and transient photoionization spectroscopy and supported by fluorescence spectroscopy. The experimental results were analyzed in terms of a step-wise process involving the ionization and laser-assisted scattering events, and a generalized semiclassical theory was developed and applied to predict the contribution of collective ionization to the total ionization yield.

To enable this experimental study, a setup facilitating to conduct angle-resolved photoelectron spectroscopy experiments at near-ambient pressure conditions was designed, constructed, and characterized. The outstanding features of the new setup as compared to other existing apparatuses, allowed to increase the long-term stability of the experimental parameters, reduce the data acquisition time, and apply target pressures over a larger range by positioning the interaction region in the vicinity of a liquid microjet containing different samples (such as water, ethanol, and acetone). To evaluate the data with high precision while avoiding preprocessing of information, a modular event-based acquisition program employing high sample rate measurements for a wide range of applications was developed. Both, experimental setup and acquisition program, are in operation and will be used in future experiments on strong-field ionization.

Due to the improvements in data acquisition, a comprehensive analysis of collective ionization in dense water and acetone gas by strong laser fields was accomplished. The results obtained at low gas densities, where ionization of isolated molecules constitutes the emission yield and no collective effects are expected, demonstrate a good agreement with the known properties of above threshold ionization (ATI) and high-order ATI (HATI). Upon increasing the target density, the emission was changed significantly and in a non-linear way, revealing the role of collective effects in ionization of dense gas samples. The collective emission was then extracted by exploiting the characteristic density dependence of single-particle and many-particle ionization. This decomposition yielded the first experimental spectrum of the so-called incoherent HATI (iHATI) effect. The experimental results are found to be in a good agreement with fully quantum-mechanical theoretical descriptions[42]. However, application of semiclassical trajectory calculations led to a more general and simplified model enabling to predict emission by the iHATI effect and results by this model were shown to be in accordance with the decomposed experimental data. The good agreement of experimental data of acetone and water with the semiclassical calculations demonstrates that quantum-mechanical properties of the

sample do not play an important role under the applied experimental conditions. The application of the Kroll-Watson approximation (KWA) to describe the laser-assisted scattering step is found to be a promising approach to quantitatively describe partial scattering cross sections, and it appears as a reasonable extension of the semiclassical trajectories analysis.

After validating the emission effects of iHATI in the vicinity of the jet, photoemission from the liquid phase was studied by steady and transient photoelectron spectroscopy. First, the emission channels involving more than one scattering event during the laser pulse appeared as a valid description of the enhanced ionization and this description was shown to be in agreement with the previously developed semiclassical calculations of the iHATI$^{(2)}$ emission. Additionally, fingerprints of the plasma formation such as fluorescence, charge accumulation, delayed auto-ionization, and plasma oscillations were observed. However, these results were shown to be partially in disagreement with existing publications and because of the complexity in the description of the strong-field ionization of liquid targets no further conclusions were made. The laser plasma formation in the liquid phase remains an interesting topic for further investigations.

In conclusion, a first step towards a macroscopic description of collective ionization by extension of microscopic ionization models was performed in this work.

In the side-project devoted to the development of methods of data evaluation for ultrafast transient photoelectron spectroscopy, an analysis package was developed that allows to reveal the early-time dynamics of different molecular systems on the basis of transient photoemission spectra obtained with a laser pulse durations of similar or even longer time scale than the observed processes itself.

A. Acronyms

TDSE	time-dependent Schrödinger equation
cw	continuous wave
ATI	above threshold ionization
ATD	above threshold detachment
KA	Keldysh ansatz
SFA	strong-field approximation
TCSFA	trajectory-based Coulomb-corrected strong-field approximation
XUV	extreme ultraviolett
HATI	high-order above threshold ionization (ATI)
iHATI	incoherent high-order ATI (HATI)
LAES	laser-assisted electron scattering
ITM	imaginary-time method
SMM	simple-man model
CVA	Coulomb-Volkov approximation
HHG	high harmonic generation
FHG	fifth harmonic generation
KWA	Kroll-Watson approximation
Ti:Sa	Titanium-Sapphire
CPA	chirped-pulse amplification
NIR	near-infrared light
OPA	optical parametric amplifier
DFG	difference frequency generation
BBO	beta barium borate
WLG	white light generation
EAL	electron attenuation length
S1	spectrometer 1

S2	spectrometer 2 ... 44
E1	experimental setup 1 ... 95
E2	experimental setup 2 ... 76
SCE	space-charge effect ... 89
KFR	Keldysh-Faisal-Reiss theory ... 2
SAE	single-active-electron ... 30
PME	Pauli Master Equation ... 102
MCP	microchannel plate ... 89
GUI	graphical user interface ... 58
IPC	inter-process communication ... 59
FIFO	first-in-first-out ... 61
GUID	globally unique identifier ... 62
CSV	comma-separated values ... 63
TSV	tab-separated values ... 63
HDF5	hierarchical data format 5 ... 63
XML	extensible markup language ... 63
TOF	time-of-flight ... 43

Bibliography

[1] L V Keldysh. Ionization in the field of a strong electromagnetic wave. *JETP*, 20 (5):1307, May 1965. URL http://www.jetp.ac.ru/cgi-bin/e/index/e/20/5/p1307?a=list.

[2] G. F. Gribakin and M. Yu. Kuchiev. Multiphoton detachment of electrons from negative ions. *Phys. Rev. A*, 55:3760–3771, May 1997. doi: 10.1103/PhysRevA.55.3760. URL http://link.aps.org/doi/10.1103/PhysRevA.55.3760.

[3] F H M Faisal. Multiphoton transitions. iv. bound-free transition integrals in compact forms. *Journal of Physics B: Atomic and Molecular Physics*, 6(3):553, 1973. URL http://stacks.iop.org/0022-3700/6/i=3/a=023.

[4] Howard R. Reiss. Gauges for intense-field electrodynamics. *Phys. Rev. A*, 22:770–772, Aug 1980. doi: 10.1103/PhysRevA.22.770. URL http://link.aps.org/doi/10.1103/PhysRevA.22.770.

[5] Howard R. Reiss. Effect of an intense electromagnetic field on a weakly bound system. *Phys. Rev. A*, 22:1786–1813, Nov 1980. doi: 10.1103/PhysRevA.22.1786. URL http://link.aps.org/doi/10.1103/PhysRevA.22.1786.

[6] Boris Bergues, Yongfeng Ni, Hanspeter Helm, and Igor Yu. Kiyan. Experimental study of photodetachment in a strong laser field of circular polarization. *Phys. Rev. Lett.*, 95:263002, Dec 2005. doi: 10.1103/PhysRevLett.95.263002. URL http://link.aps.org/doi/10.1103/PhysRevLett.95.263002.

[7] Boris Bergues, Zunaira Ansari, Dag Hanstorp, and Igor Yu. Kiyan. Photodetachment in a strong laser field: An experimental test of keldysh-like theories. *Phys. Rev. A*, 75:063415, Jun 2007. doi: 10.1103/PhysRevA.75.063415. URL http://link.aps.org/doi/10.1103/PhysRevA.75.063415.

[8] Boris Bergues and Igor Yu. Kiyan. Two-electron photodetachment of negative ions in a strong laser field. *Phys. Rev. Lett.*, 100:143004, Apr 2008. doi: 10.1103/PhysRevLett.100.143004. URL http://link.aps.org/doi/10.1103/PhysRevLett.100.143004.

[9] A. Gazibegović-Busuladžić, D.B. Milošević, W. Becker, B. Bergues, H Hultgren, and I. Yu. Kiyan. Electron rescattering in above-threshold photodetachment of negative

ions. *Phys. Rev. Lett.*, 104:103004, Mar 2010. doi: 10.1103/PhysRevLett.104.103004. URL http://link.aps.org/doi/10.1103/PhysRevLett.104.103004.

[10] Hannes Hultgren and Igor Yu. Kiyan. Photodetachment dynamics of f_2^- in a strong laser field. *Phys. Rev. A*, 84:015401, Jul 2011. doi: 10.1103/PhysRevA.84.015401. URL http://link.aps.org/doi/10.1103/PhysRevA.84.015401.

[11] D. Bauer, D. B. Milošević, and W. Becker. Strong-field approximation for intense-laser-atom processes: The choice of gauge. *Phys. Rev. A*, 72:023415, Aug 2005. doi: 10.1103/PhysRevA.72.023415. URL http://link.aps.org/doi/10.1103/PhysRevA.72.023415.

[12] W. Becker, F. Grasbon, R. Kopold, D.B. Milošević, G.G. Paulus, and H. Walther. Above-threshold ionization: From classical features to quantum effects. *Advances In Atomic, Molecular, and Optical Physics*, 48:35 – 98, 2002. ISSN 1049-250X. doi: http://dx.doi.org/10.1016/S1049-250X(02)80006-4. URL http://www.sciencedirect.com/science/article/pii/S1049250X02800064.

[13] Nikolai B Delone and Vladimir Krainov. *Multiphoton Processes in Atoms*, volume 13 of *Springer Series on Atomic, Optical, and Plasma Physics*. Springer-Verlag Berlin Heidelberg, 2 edition, 2000. doi: 10.1007/978-3-642-57208-1.

[14] D. B. Milošević, G. G. Paulus, D. Bauer, and W. Becker. Above-threshold ionization by few-cycle pulses. *Journal of Physics B: Atomic, Molecular and Optical Physics*, 39(14):R203, 2006. URL http://stacks.iop.org/0953-4075/39/i=14/a=R01.

[15] Diego G. Arbó, Jorge E. Miraglia, María Silvia Gravielle, Klaus Schiessl, Emil Persson, and Joachim Burgdörfer. Coulomb-volkov approximation for near-threshold ionization by short laser pulses. *Phys. Rev. A*, 77:013401, Jan 2008. doi: 10.1103/PhysRevA.77.013401. URL http://link.aps.org/doi/10.1103/PhysRevA.77.013401.

[16] Tian-Min Yan, S. V. Popruzhenko, M. J. J. Vrakking, and D. Bauer. Low-energy structures in strong field ionization revealed by quantum orbits. *Phys. Rev. Lett.*, 105:253002, Dec 2010. doi: 10.1103/PhysRevLett.105.253002. URL http://link.aps.org/doi/10.1103/PhysRevLett.105.253002.

[17] P. B. Corkum, N. H. Burnett, and F. Brunel. Above-threshold ionization in the long-wavelength limit. *Phys. Rev. Lett.*, 62:1259–1262, Mar 1989. doi: 10.1103/PhysRevLett.62.1259. URL http://link.aps.org/doi/10.1103/PhysRevLett.62.1259.

[18] G. G. Paulus, W. Becker, W. Nicklich, and H. Walther. Rescattering effects in above-threshold ionization: a classical model. *Journal of Physics B: Atomic,*

Molecular and Optical Physics, 27(21):L703, 1994. URL http://stacks.iop.org/0953-4075/27/i=21/a=003.

[19] A.M. Perelomov, V.S. Popov, and M.V. Terent'ev. Ionization of atoms in an alternating electric field. *JETP*, 23(5):924, November 1966. (Russian original - ZhETF, Vol. 50, No. 5, p. 1393, November 1966).

[20] V.S. Popov, V.P. Kuznetsov, and A.M. Perelomov. Quasiclassical approximation for nonstationary problems. *JETP*, 26(1):222, January 1968. URL http://www.jetp.ac.ru/cgi-bin/e/index/e/26/1/p222?a=list. (Russian original - ZhETF, Vol. 53, No. 1, p. 331, January 1968).

[21] K. C. Kulander, K. J. Schafer, and J. L. Krause. *Dynamics of Short-Pulse Excitation, Ionization and Harmonic Conversion*, pages 95–110. Springer US, Boston, MA, 1993. ISBN 978-1-4615-7963-2. doi: 10.1007/978-1-4615-7963-2_10. URL http://dx.doi.org/10.1007/978-1-4615-7963-2_10.

[22] P. B. Corkum. Plasma perspective on strong field multiphoton ionization. *Phys. Rev. Lett.*, 71:1994–1997, Sep 1993. doi: 10.1103/PhysRevLett.71.1994. URL http://link.aps.org/doi/10.1103/PhysRevLett.71.1994.

[23] Jan Metje, Mario Borgwardt, Alexandre Moguilevski, Alexander Kothe, Nicholas Engel, Martin Wilke, Ruba Al-Obaidi, Daniel Tolksdorf, Alexander Firsov, Maria Brzhezinskaya, Alexei Erko, Igor Yu. Kiyan, and Emad F. Aziz. Monochromatization of femtosecond xuv light pulses with the use of reflection zone plates. *Opt. Express*, 22(9):10747–10760, May 2014. doi: 10.1364/OE.22.010747. URL http://www.opticsexpress.org/abstract.cfm?URI=oe-22-9-10747.

[24] P. M. Kraus, B. Mignolet, D. Baykusheva, A. Rupenyan, L. Horný, E. F. Penka, G. Grassi, O. I. Tolstikhin, J. Schneider, F. Jensen, L. B. Madsen, A. D. Bandrauk, F. Remacle, and H. J. Wörner. Measurement and laser control of attosecond charge migration in ionized iodoacetylene. *Science*, 350(6262):790–795, 2015. ISSN 0036-8075. doi: 10.1126/science.aab2160. URL http://science.sciencemag.org/content/350/6262/790.

[25] F. Grasbon, G. G. Paulus, S. L. Chin, H. Walther, J. Muth-Böhm, A. Becker, and F. H. M. Faisal. Signatures of symmetry-induced quantum-interference effects observed in above-threshold-ionization spectra of molecules. *Phys. Rev. A*, 63:041402, Mar 2001. doi: 10.1103/PhysRevA.63.041402. URL http://link.aps.org/doi/10.1103/PhysRevA.63.041402.

[26] C. C. Chirilă and M. Lein. High-order above-threshold ionization in stretched molecules. *Phys. Rev. A*, 74:051401, Nov 2006. doi: 10.1103/PhysRevA.74.051401. URL http://link.aps.org/doi/10.1103/PhysRevA.74.051401.

[27] M. Okunishi, R. Itaya, K. Shimada, G. Prümper, K. Ueda, M. Busuladžić, A. Gazibegović-Busuladžić, D. B. Milošević, and W. Becker. Two-source double-slit interference in angle-resolved high-energy above-threshold ionization spectra of diatoms. *Phys. Rev. Lett.*, 103:043001, Jul 2009. doi: 10.1103/PhysRevLett.103.043001. URL http://link.aps.org/doi/10.1103/PhysRevLett.103.043001.

[28] M. Busuladžić, A. Gazibegović-Busuladžić, E. Hasović, D.B. Milošević, and W. Becker. Atoms and molecules in a strong laser field. *Acta Phys. Pol. A*, 116(4):516–518, oct 2009. doi: 10.12693/aphyspola.116.516. URL http://dx.doi.org/10.12693/APhysPolA.116.516.

[29] Z Ansari, M Böttcher, B Manschwetus, H Rottke, W Sandner, A Verhoef, M Lezius, G G Paulus, A Saenz, and D B Milošević. Interference in strong-field ionization of a two-centre atomic system. *New Journal of Physics*, 10(9):093027, 2008. URL http://stacks.iop.org/1367-2630/10/i=9/a=093027.

[30] C. Rose-Petruck, K. J. Schafer, K. R. Wilson, and C. P. J. Barty. Ultrafast electron dynamics and inner-shell ionization in laser driven clusters. *Phys. Rev. A*, 55:1182–1190, Feb 1997. doi: 10.1103/PhysRevA.55.1182. URL http://link.aps.org/doi/10.1103/PhysRevA.55.1182.

[31] E. M. Snyder, S. A. Buzza, and A. W. Castleman, Jr. Intense field-matter interactions: Multiple ionization of clusters. *Phys. Rev. Lett.*, 77:3347–3350, Oct 1996. doi: 10.1103/PhysRevLett.77.3347. URL http://link.aps.org/doi/10.1103/PhysRevLett.77.3347.

[32] T. Ditmire, T. Donnelly, A. M. Rubenchik, R. W. Falcone, and M. D. Perry. Interaction of intense laser pulses with atomic clusters. *Phys. Rev. A*, 53:3379–3402, May 1996. doi: 10.1103/PhysRevA.53.3379. URL http://link.aps.org/doi/10.1103/PhysRevA.53.3379.

[33] T. Ditmire. Atomic clusters in ultrahigh intensity light fields. *Contemporary Physics*, 38(5):315–328, 1997. doi: 10.1080/001075197182298. URL http://dx.doi.org/10.1080/001075197182298.

[34] T. Ditmire, E. Springate, J. W. G. Tisch, Y. L. Shao, M. B. Mason, N. Hay, J. P. Marangos, and M. H. R. Hutchinson. Explosion of atomic clusters heated by high-intensity femtosecond laser pulses. *Phys. Rev. A*, 57:369 – 382, Jan 1998. doi: 10.1103/PhysRevA.57.369. URL http://link.aps.org/doi/10.1103/PhysRevA.57.369.

[35] V.P. Krainov and M.B. Smirnov. Cluster beams in the super-intense femtosecond laser pulse. *Physics Reports*, 370(3):237 – 331, 2002. ISSN 0370-1573. doi: http:

//dx.doi.org/10.1016/S0370-1573(02)00272-7. URL http://www.sciencedirect.com/science/article/pii/S0370157302002727.

[36] Vladimir P Krainov and Mikhail B Smirnov. The evolution of large clusters under the action of ultrashort superintense laser pulses. *Physics-Uspekhi*, 43(9):901, 2000. URL http://stacks.iop.org/1063-7869/43/i=9/a=R02.

[37] Y. L. Shao, T. Ditmire, J. W. G. Tisch, E. Springate, J. P. Marangos, and M. H. R. Hutchinson. Multi-kev electron generation in the interaction of intense laser pulses with xe clusters. *Phys. Rev. Lett.*, 77:3343–3346, Oct 1996. doi: 10.1103/PhysRevLett.77.3343. URL http://link.aps.org/doi/10.1103/PhysRevLett.77.3343.

[38] B. Schütte, P. Ye, S. Patchkovskii, D. R. Austin, C. Brahms, C. Strüber, T. Witting, M. Y. Ivanov, J. W. G. Tisch, and J. P. Marangos. Mid-infrared strong-field ionization of clusters using two-cycle pulses. *ArXiv e-prints*, page arXiv:1603.05493, March 2016. URL http://adsabs.harvard.edu/abs/2016arXiv160305493S.

[39] D. Mathur and F. A. Rajgara. Dynamics of atomic clusters in intense optical fields of ultrashort duration. *Journal of Chemical Sciences*, 124(1):75–81, 2012. ISSN 0973-7103. doi: 10.1007/s12039-011-0188-y. URL http://dx.doi.org/10.1007/s12039-011-0188-y.

[40] F. Brunel. Not-so-resonant, resonant absorption. *Phys. Rev. Lett.*, 59:52–55, Jul 1987. doi: 10.1103/PhysRevLett.59.52. URL http://link.aps.org/doi/10.1103/PhysRevLett.59.52.

[41] H. A. Sumeruk, S. Kneip, D. R. Symes, I. V. Churina, A. V. Belolipetski, T. D. Donnelly, and T. Ditmire. Control of strong-laser-field coupling to electrons in solid targets with wavelength-scale spheres. *Phys. Rev. Lett.*, 98:045001, Jan 2007. doi: 10.1103/PhysRevLett.98.045001. URL http://link.aps.org/doi/10.1103/PhysRevLett.98.045001.

[42] A. Čerkić and D. B. Milošević. The contribution of incoherent photoelectron scattering off neighbouring atoms to the above-threshold ionization and detachment spectra. *Journal of Physics B: Atomic, Molecular and Optical Physics*, 39(21):4419, 2006. URL http://stacks.iop.org/0953-4075/39/i=21/a=007.

[43] A. Čerkić and D. B. Milošević. The role of incoherent scattering in laser-induced and laser-assisted processes. *Laser Physics*, 19(4):783–790, 2009. ISSN 1555-6611. doi: 10.1134/S1054660X09040367. URL http://dx.doi.org/10.1134/S1054660X09040367.

[44] A. Čerkić and D. B. Milošević. Few-cycle laser-pulse-assisted electron-atom potential scattering. *Phys. Rev. A*, 87:033417, Mar 2013. doi: 10.1103/PhysRevA.87.033417. URL http://link.aps.org/doi/10.1103/PhysRevA.87.033417.

[45] M. Pettersson, R. Zadoyan, J. Eloranta, N. Schwentner, and V. A. Apkarian. Strong-field excitation of liquid and solid xe using intense femtosecond pulses. *The Journal of Physical Chemistry A*, 106(36):8308–8316, 2002. doi: 10.1021/jp0146317. URL http://dx.doi.org/10.1021/jp0146317.

[46] Michael S. Brown, Thomas Erickson, Kyle Frische, and William M. Roquemore. Hot electron dominated rapid transverse ionization growth in liquid water. *Opt. Express*, 19(13):12241 – 12247, Jun 2011. doi: 10.1364/OE.19.012241. URL http://www.opticsexpress.org/abstract.cfm?URI=oe-19-13-12241.

[47] Y. T. Li, J. Zhang, Z. M. Sheng, H. Teng, T. J. Liang, X. Y. Peng, X. Lu, Y. J. Li, and X. W. Tang. Spatial distribution of high-energy electron emission from water plasmas produced by femtosecond laser pulses. *Phys. Rev. Lett.*, 90:165002, Apr 2003. doi: 10.1103/PhysRevLett.90.165002. URL http://link.aps.org/doi/10.1103/PhysRevLett.90.165002.

[48] J. Zhang, Y. T. Li, Z. M. Sheng, Z. Y. Wei, Q. L. Dong, and X. Lu. Generation and propagation of hot electrons in laser-plasmas. *Applied Physics B*, 80(8):957–971, 2005. ISSN 1432-0649. doi: 10.1007/s00340-005-1862-x. URL http://dx.doi.org/10.1007/s00340-005-1862-x.

[49] Reika Kanya, Yuya Morimoto, and Kaoru Yamanouchi. Observation of laser-assisted electron-atom scattering in femtosecond intense laser fields. *Phys. Rev. Lett.*, 105:123202, Sep 2010. doi: 10.1103/PhysRevLett.105.123202. URL http://link.aps.org/doi/10.1103/PhysRevLett.105.123202.

[50] S. Ter-Avetisyan, B. Ramakrishna, M. Borghesi, D. Doria, M. Zepf, G. Sarri, L. Ehrentraut, A. Andreev, P. V. Nickles, S. Steinke, W. Sandner, M. Schnürer, and V. Tikhonchuk. Mev negative ion generation from ultra-intense laser interaction with a water spray. *Applied Physics Letters*, 99(5):051501, 2011. doi: 10.1063/1.3622664. URL http://link.aip.org/link/?APL/99/051501/1.

[51] S. Ter-Avetisyan, B. Ramakrishna, D. Doria, R. Prasad, M. Borghesi, A. A. Andreev, S. Steinke, M. Schnürer, P. V. Nickles, and V. Tikhonchuk. Mev negative ion source from ultra-intense laser-matter interaction. *Review of Scientific Instruments*, 83(2):02A710, 2012. doi: 10.1063/1.3670741. URL http://link.aip.org/link/?RSI/83/02A710/1.

[52] O. Link, E. Lugovoy, K. Siefermann, Y. Liu, M. Faubel, and B. Abel. Ultrafast electronic spectroscopy for chemical analysis near liquid water interfaces: concepts and

applications. *Applied Physics A*, 96(1):117–135, 2009. ISSN 1432-0630. doi: 10.1007/s00339-009-5179-1. URL http://dx.doi.org/10.1007/s00339-009-5179-1.

[53] M. Faubel, K. R. Siefermann, Y. Liu, and B. Abel. Ultrafast soft x-ray photoelectron spectroscopy at liquid water microjets. *Accounts of Chemical Research*, 45(1): 120–130, 2012. doi: 10.1021/ar200154w. URL http://dx.doi.org/10.1021/ar200154w. PMID: 22075058.

[54] A. Flettner, T. Pfeifer, D. Walter, C. Winterfeldt, C. Spielmann, and G. Gerber. High-harmonic generation and plasma radiation from water microdroplets. *Applied Physics B*, 77(8):747–751, 2003. ISSN 1432-0649. doi: 10.1007/s00340-003-1329-x. URL http://dx.doi.org/10.1007/s00340-003-1329-x.

[55] Heiko G. Kurz, Daniel S. Steingrube, Detlev Ristau, Manfred Lein, Uwe Morgner, and Milutin Kovačev. High-order-harmonic generation from dense water microdroplets. *Phys. Rev. A*, 87:063811, Jun 2013. doi: 10.1103/PhysRevA.87.063811. URL http://link.aps.org/doi/10.1103/PhysRevA.87.063811.

[56] P. Agostini, F. Fabre, G. Mainfray, G. Petite, and N. K. Rahman. Free-free transitions following six-photon ionization of xenon atoms. *Phys. Rev. Lett.*, 42: 1127–1130, Apr 1979. doi: 10.1103/PhysRevLett.42.1127. URL http://link.aps.org/doi/10.1103/PhysRevLett.42.1127.

[57] P Agostini, M Clement, F Fabre, and G Petite. Multiphoton ionisation involving multiphoton continuum-continuum transitions. *Journal of Physics B: Atomic and Molecular Physics*, 14(15):L491, 1981. URL http://stacks.iop.org/0022-3700/14/i=15/a=004.

[58] S. F. C. Shearer, M. C. Smyth, and G. F. Gribakin. Electron detachment from negative ions in a short laser pulse. *Phys. Rev. A*, 84:033409, Sep 2011. doi: 10.1103/PhysRevA.84.033409. URL http://link.aps.org/doi/10.1103/PhysRevA.84.033409.

[59] D. M. Wolkow. Über eine klasse von lösungen der diracschen gleichung. *Zeitschrift für Physik*, 94(3):250–260, March 1935. ISSN 0044-3328. doi: 10.1007/BF01331022. URL http://dx.doi.org/10.1007/BF01331022.

[60] S V Popruzhenko. Keldysh theory of strong field ionization: history, applications, difficulties and perspectives. *Journal of Physics B: Atomic, Molecular and Optical Physics*, 47(20):204001, 2014. URL http://stacks.iop.org/0953-4075/47/i=20/a=204001.

[61] M. V. Frolov, N. L. Manakov, E. A. Pronin, and Anthony F. Starace. Model-independent quantum approach for intense laser detachment of a weakly bound

electron. *Phys. Rev. Lett.*, 91:053003, Aug 2003. doi: 10.1103/PhysRevLett.91.053003. URL http://link.aps.org/doi/10.1103/PhysRevLett.91.053003.

[62] H. R. Reiss. Velocity-gauge theory for the treatment of strong-field photodetachment. *Phys. Rev. A*, 76:033404, Sep 2007. doi: 10.1103/PhysRevA.76.033404. URL http://link.aps.org/doi/10.1103/PhysRevA.76.033404.

[63] R. Landauer and Th. Martin. Barrier interaction time in tunneling. *Rev. Mod. Phys.*, 66:217–228, Jan 1994. doi: 10.1103/RevModPhys.66.217. URL http://link.aps.org/doi/10.1103/RevModPhys.66.217.

[64] Yue Ban, E. Ya. Sherman, J. G. Muga, and M. Büttiker. Time scales of tunneling decay of a localized state. *Phys. Rev. A*, 82:062121, Dec 2010. doi: 10.1103/PhysRevA.82.062121. URL http://link.aps.org/doi/10.1103/PhysRevA.82.062121.

[65] C. R. McDonald, G. Orlando, G. Vampa, and T. Brabec. Tunnel ionization dynamics of bound systems in laser fields: How long does it take for a bound electron to tunnel? *Phys. Rev. Lett.*, 111:090405, Aug 2013. doi: 10.1103/PhysRevLett.111.090405. URL http://link.aps.org/doi/10.1103/PhysRevLett.111.090405.

[66] P. Eckle, A. N. Pfeiffer, C. Cirelli, A. Staudte, R. Dörner, H. G. Muller, M. Büttiker, and U. Keller. Attosecond ionization and tunneling delay time measurements in helium. *Science*, 322(5907):1525–1529, 2008. ISSN 0036-8075. doi: 10.1126/science.1163439. URL http://science.sciencemag.org/content/322/5907/1525.

[67] Alexandra S. Landsman, Matthias Weger, Jochen Maurer, Robert Boge, André Ludwig, Sebastian Heuser, Claudio Cirelli, Lukas Gallmann, and Ursula Keller. Ultrafast resolution of tunneling delay time. *Optica*, 1(5):343–349, Nov 2014. doi: 10.1364/OPTICA.1.000343. URL http://www.osapublishing.org/optica/abstract.cfm?URI=optica-1-5-343.

[68] R. Boge, C. Cirelli, A. S. Landsman, S. Heuser, A. Ludwig, J. Maurer, M. Weger, L. Gallmann, and U. Keller. Probing nonadiabatic effects in strong-field tunnel ionization. *Phys. Rev. Lett.*, 111:103003, Sep 2013. doi: 10.1103/PhysRevLett.111.103003. URL http://link.aps.org/doi/10.1103/PhysRevLett.111.103003.

[69] A. Gazibegović-Busuladžić, D.B. Milošević, and W. Becker. Gauge dependence of the strong-field approximation: Theory vs. experiment for photodetachment of f-. *Optics Communications*, 275(1):116 – 122, 2007. ISSN 0030-4018. doi: http://dx.doi.org/10.1016/j.optcom.2007.03.009. URL http://www.sciencedirect.com/science/article/pii/S0030401807002611.

[70] S. F. C. Shearer and C. R. J. Addis. Strong-field photodetachment of h^- by few-cycle laser pulses. *Phys. Rev. A*, 85:063409, Jun 2012. doi: 10.1103/PhysRevA.85.063409. URL http://link.aps.org/doi/10.1103/PhysRevA.85.063409.

[71] L. D. Landau and E. M. Lifshitz. *Quantum Mechanics-Nonrelativistic Theory (Course of Theoretical Physics)*, volume 3 of *Course of Theoretical Physics*. Pergamon Pr, 3 edition, 1981. ISBN 0080209408. URL http://www.sciencedirect.com/science/book/9780080209401.

[72] X. Y. Lai, W. Quan, and X. Liu. Tunneling-induced shift of the cutoff law for high-order above-threshold ionization. *Phys. Rev. A*, 84:025401, Aug 2011. doi: 10.1103/PhysRevA.84.025401. URL http://link.aps.org/doi/10.1103/PhysRevA.84.025401.

[73] D. B. Milošević, G. G. Paulus, and W. Becker. Ionization by few-cycle pulses: Tracing the electron orbits. *Phys. Rev. A*, 71:061404, Jun 2005. doi: 10.1103/PhysRevA.71.061404. URL http://link.aps.org/doi/10.1103/PhysRevA.71.061404.

[74] V. S. Popov. Multiphoton ionization of atoms by an ultrashort laser pulse. *Journal of Experimental and Theoretical Physics Letters*, 73(1):1 – 5, 2001. ISSN 1090-6487. doi: 10.1134/1.1355394. URL http://dx.doi.org/10.1134/1.1355394.

[75] D. R. Hartree. The wave mechanics of an atom with a non-coulomb central field. part i. theory and methods. *Mathematical Proceedings of the Cambridge Philosophical Society*, 24:89–110, 1 1928. ISSN 1469-8064. doi: 10.1017/S0305004100011919. URL http://journals.cambridge.org/article_S0305004100011919.

[76] Vladimir S Popov. Tunnel and multiphoton ionization of atoms and ions in a strong laser field (keldysh theory). *Physics-Uspekhi*, 47(9):855, 2004. URL http://stacks.iop.org/1063-7869/47/i=9/a=R01.

[77] R Kopold, W Becker, M Kleber, and G G Paulus. Channel-closing effects in high-order above-threshold ionization and high-order harmonic generation. *Journal of Physics B: Atomic, Molecular and Optical Physics*, 35(2):217, 2002. URL http://stacks.iop.org/0953-4075/35/i=2/a=302.

[78] T. W. B. Kibble. Mutual refraction of electrons and photons. *Phys. Rev.*, 150: 1060–1069, Oct 1966. doi: 10.1103/PhysRev.150.1060. URL http://link.aps.org/doi/10.1103/PhysRev.150.1060.

[79] A.V. Gaponov and M.A. Miller. Potential wells for charged particles in a high-frequency electromagnetic field. *Zh. Eksp. Teor. Fiz.*, 34(1):242, July 1958. URL http://www.jetp.ac.ru/cgi-bin/e/index/e/7/1/p168?a=list. JETP, Vol. 7, No. 1, p. 168 (July 1958) (English translation).

[80] R. R. Freeman, P. H. Bucksbaum, H. Milchberg, S. Darack, D. Schumacher, and M. E. Geusic. Above-threshold ionization with subpicosecond laser pulses. *Phys. Rev. Lett.*, 59:1092–1095, Sep 1987. doi: 10.1103/PhysRevLett.59.1092. URL http://link.aps.org/doi/10.1103/PhysRevLett.59.1092.

[81] Mikhail V Fedorov. *Atomic and free electrons in a strong light field*. World Scientific, Singapore, 1997. URL https://cds.cern.ch/record/330956.

[82] Pierre Agostini, Joseph Kupersztych, Louis A. Lompré, Guillaume Petite, and François Yergeau. Direct evidence of ponderomotive effects via laser pulse duration in above-threshold ionization. *Phys. Rev. A*, 36:4111–4114, Oct 1987. doi: 10.1103/PhysRevA.36.4111. URL http://link.aps.org/doi/10.1103/PhysRevA.36.4111.

[83] Min Li, Yunquan Liu, Hong Liu, Yudong Yang, Jialei Yuan, Xianrong Liu, Yongkai Deng, Chengyin Wu, and Qihuang Gong. Photoelectron angular distributions of low-order above-threshold ionization of xe in the multiphoton regime. *Phys. Rev. A*, 85:013414, Jan 2012. doi: 10.1103/PhysRevA.85.013414. URL http://link.aps.org/doi/10.1103/PhysRevA.85.013414.

[84] C M Maharjan, A S Alnaser, I Litvinyuk, P Ranitovic, and C L Cocke. Wavelength dependence of momentum-space images of low-energy electrons generated by short intense laser pulses at high intensities. *Journal of Physics B: Atomic, Molecular and Optical Physics*, 39(8):1955, 2006. URL http://stacks.iop.org/0953-4075/39/i=8/a=013.

[85] William D. M. Lunden, Péter Sándor, Thomas C. Weinacht, and Tamás Rozgonyi. Model for describing resonance-enhanced strong-field ionization with shaped ultrafast laser pulses. *Phys. Rev. A*, 89:053403, May 2014. doi: 10.1103/PhysRevA.89.053403. URL http://link.aps.org/doi/10.1103/PhysRevA.89.053403.

[86] Ph. A. Korneev, S. V. Popruzhenko, S. P. Goreslavski, W. Becker, G. G. Paulus, B. Fetić, and D. B. Milošević. Interference structure of above-threshold ionization versus above-threshold detachment. *New Journal of Physics*, 14(5):055019, 2012. URL http://stacks.iop.org/1367-2630/14/i=5/a=055019.

[87] M. D. Perry, O. L. Landen, A. Szöke, and E. M. Campbell. Multiphoton ionization of the noble gases by an intense 10^{14}-w/cm^2 dye laser. *Phys. Rev. A*, 37:747–760, Feb 1988. doi: 10.1103/PhysRevA.37.747. URL http://link.aps.org/doi/10.1103/PhysRevA.37.747.

[88] M. D. Perry, A. Szoke, O. L. Landen, and E. M. Campbell. Nonresonant multiphoton ionization of noble gases: Theory and experiment. *Phys. Rev. Lett.*, 60:1270–1273,

Mar 1988. doi: 10.1103/PhysRevLett.60.1270. URL http://link.aps.org/doi/10.1103/PhysRevLett.60.1270.

[89] S. V. Popruzhenko, V. D. Mur, V. S. Popov, and D. Bauer. Strong field ionization rate for arbitrary laser frequencies. *Phys. Rev. Lett.*, 101:193003, Nov 2008. doi: 10.1103/PhysRevLett.101.193003. URL http://link.aps.org/doi/10.1103/PhysRevLett.101.193003.

[90] S. B. Popruzhenko, V. D. Mur, V. S. Popov, and D. Bauer. Multiphoton ionization of atoms and ions by high-intensity x-ray lasers. *Journal of Experimental and Theoretical Physics*, 108(6):947–962, 2009. ISSN 1090-6509. doi: 10.1134/S1063776109060053. URL http://dx.doi.org/10.1134/S1063776109060053.

[91] M. D. Perry, O. L. Landen, A. Szöke, and E. M. Campbell. Multiphoton ionization of the noble gases by an intense 10^{14}-w/cm^2 dye laser. *Phys. Rev. A*, 37:747–760, Feb 1988. doi: 10.1103/PhysRevA.37.747. URL http://link.aps.org/doi/10.1103/PhysRevA.37.747.

[92] S. L. Chin, Claude Rolland, P. B. Corkum, and Paul Kelly. Multiphoton ionization of xe and kr with intense 0.62-μm femtosecond pulses. *Phys. Rev. Lett.*, 61:153–156, Jul 1988. doi: 10.1103/PhysRevLett.61.153. URL http://link.aps.org/doi/10.1103/PhysRevLett.61.153.

[93] Manoj Jain and Narkis Tzoar. Compton scattering in the presence of coherent electromagnetic radiation. *Phys. Rev. A*, 18:538–545, Aug 1978. doi: 10.1103/PhysRevA.18.538. URL http://link.aps.org/doi/10.1103/PhysRevA.18.538.

[94] G. Duchateau, E. Cormier, H. Bachau, and R. Gayet. Coulomb-volkov approach of atom ionization by intense and ultrashort laser pulses. *Phys. Rev. A*, 63:053411, Apr 2001. doi: 10.1103/PhysRevA.63.053411. URL http://link.aps.org/doi/10.1103/PhysRevA.63.053411.

[95] S. Basile, F. Trombetta, and G. Ferrante. Twofold symmetric angular distributions in multiphoton ionization with elliptically polarized light. *Phys. Rev. Lett.*, 61:2435–2437, Nov 1988. doi: 10.1103/PhysRevLett.61.2435. URL http://link.aps.org/doi/10.1103/PhysRevLett.61.2435.

[96] A. Jaroń, J.Z. Kamiński, and F. Ehlotzky. Asymmetries in the angular distributions of above threshold ionization in an elliptically polarized laser field. *Optics Communications*, 163(1 – 3):115 – 121, 1999. ISSN 0030-4018. doi: http://dx.doi.org/10.1016/S0030-4018(99)00122-4. URL http://www.sciencedirect.com/science/article/pii/S0030401899001224.

[97] M. Bashkansky, P. H. Bucksbaum, and D. W. Schumacher. Asymmetries in above-threshold ionization. *Phys. Rev. Lett.*, 60:2458–2461, Jun 1988. doi: 10.1103/PhysRevLett.60.2458. URL http://link.aps.org/doi/10.1103/PhysRevLett.60.2458.

[98] M Spanner, S Gräfe, S Chelkowski, D Pavičić, M Meckel, D Zeidler, A B Bardon, B Ulrich, A D Bandrauk, D M Villeneuve, R Dörner, P B Corkum, and A Staudte. Coulomb asymmetry and sub-cycle electron dynamics in multiphoton multiple ionization of h 2. *Journal of Physics B: Atomic, Molecular and Optical Physics*, 45(19): 194011, 2012. URL http://stacks.iop.org/0953-4075/45/i=19/a=194011.

[99] J. Wu, M. Meckel, S. Voss, H. Sann, M. Kunitski, L. Ph. H. Schmidt, A. Czasch, H. Kim, T. Jahnke, and R. Dörner. Coulomb asymmetry in strong field multielectron ionization of diatomic molecules. *Phys. Rev. Lett.*, 108:043002, Jan 2012. doi: 10.1103/PhysRevLett.108.043002. URL http://link.aps.org/doi/10.1103/PhysRevLett.108.043002.

[100] S.V. Popruzhenko and D. Bauer. Strong field approximation for systems with coulomb interaction. *Journal of Modern Optics*, 55(16):2573–2589, 2008. doi: 10.1080/09500340802161881. URL http://dx.doi.org/10.1080/09500340802161881.

[101] Tian-Min Yan and D. Bauer. Sub-barrier coulomb effects on the interference pattern in tunneling-ionization photoelectron spectra. *Phys. Rev. A*, 86:053403, Nov 2012. doi: 10.1103/PhysRevA.86.053403. URL http://link.aps.org/doi/10.1103/PhysRevA.86.053403.

[102] Tian-Min Yan. *Trajectory-Based Coulomb-Corrected Strong Field Approximation*. Dissertation, Universität Rostock, November 2012. URL http://rosdok.uni-rostock.de/resolve/id/rosdok_disshab_0000000934. urn:nbn:de:gbv:28-diss2013-0026-6.

[103] G. G. Paulus, W. Nicklich, Huale Xu, P. Lambropoulos, and H. Walther. Plateau in above threshold ionization spectra. *Phys. Rev. Lett.*, 72:2851–2854, May 1994. doi: 10.1103/PhysRevLett.72.2851. URL http://link.aps.org/doi/10.1103/PhysRevLett.72.2851.

[104] M Yu Kuchiev. Atomic antenna. *JETP Letters*, 45(7):404, April 1987. URL http://www.jetpletters.ac.ru/ps/1241/article_18763.shtml.

[105] Dejan B. Milošević and Fritz Ehlotzky. Scattering and reaction processes in powerful laser fields. *Advances In Atomic, Molecular, and Optical Physics*, 49:373 – 532, 2003. ISSN 1049-250X. doi: http://dx.doi.org/10.1016/S1049-250X(03)80007-1. URL http://www.sciencedirect.com/science/article/pii/S1049250X03800071.

[106] L. A. Lompré and G. Mainfray. *Multiply Charged Ions Produced in Multiphoton Ionization of Rare Gas Atoms*, pages 23–30. Springer Berlin Heidelberg, Berlin, Heidelberg, 1984. ISBN 978-3-642-70200-6. doi: 10.1007/978-3-642-70200-6_4. URL http://dx.doi.org/10.1007/978-3-642-70200-6_4. Editor: Lambropoulos, Peter and Smith, Stephen J.

[107] E. Hasović, A. Kramo, and B. D. Milošević. Energy- and angle-resolved photoelectron spectra of above-threshold ionization and detachment. *The European Physical Journal Special Topics*, 160(1):205–216, 2008. ISSN 1951-6401. doi: 10.1140/epjst/e2008-00724-9. URL http://dx.doi.org/10.1140/epjst/e2008-00724-9.

[108] F.V. Bunkin and M.V. Fedorov. Bremsstrahlung in a strong radiation field. *JETP*, 22(4):844, April 1966.

[109] Norman M. Kroll and Kenneth M. Watson. Charged-particle scattering in the presence of a strong electromagnetic wave. *Phys. Rev. A*, 8:804–809, Aug 1973. doi: 10.1103/PhysRevA.8.804. URL http://link.aps.org/doi/10.1103/PhysRevA.8.804.

[110] G Laplanche, A Durrieu, Y Flank, M Jaouen, and A Rachman. The infinite summations of perturbation theory in atomic multiphoton ionization. *Journal of Physics B: Atomic and Molecular Physics*, 9(8):1263, 1976. URL http://stacks.iop.org/0022-3700/9/i=8/a=012.

[111] A. Čerkić and D. B. Milošević. Plateau structures in potential scattering in a strong laser field. *Phys. Rev. A*, 70:053402, Nov 2004. doi: 10.1103/PhysRevA.70.053402. URL http://link.aps.org/doi/10.1103/PhysRevA.70.053402.

[112] F. Ehlotzky. Scattering phenomena in strong radiation fields ii. *Canadian Journal of Physics*, 63(7):907–932, 1985. doi: 10.1139/p85-149. URL http://dx.doi.org/10.1139/p85-149.

[113] I. Yu. Kostyukov and J.-M. Rax. Ultrahigh-intensity inverse-bremsstrahlung absorption. *Phys. Rev. Lett.*, 83:2206 – 2209, Sep 1999. doi: 10.1103/PhysRevLett.83.2206. URL http://link.aps.org/doi/10.1103/PhysRevLett.83.2206.

[114] V.P. Krainov. Absorption of electromagnetic energy by slow electrons under scattering from coulomb centers. *Journal of Experimental and Theoretical Physics*, 92(6):960–968, 2001. ISSN 1063-7761. doi: 10.1134/1.1385635. URL http://dx.doi.org/10.1134/1.1385635.

[115] A. Čerkić and D. B. Milošević. Potential scattering in a bichromatic laser field: Plateau structures. *Laser Physics*, 15(2):268 – 274, February 2005. URL https://www.researchgate.net/profile/D_Milosevic/

publication/261174481_Potential_scattering_in_a_bichromatic_laser_field_plateau_structures/links/0a85e5336d46237372000000.pdf.

[116] A. Čerkić and D. B. Milošević. Interferences of real trajectories and the emergence of quantum features in electron-atom scattering in a strong laser field. *Phys. Rev. A*, 73:033413, Mar 2006. doi: 10.1103/PhysRevA.73.033413. URL http://link.aps.org/doi/10.1103/PhysRevA.73.033413.

[117] A. Čerkić and D. B. Milošević. Focal averaging and incoherent scattering in laser-assisted radiative recombination and scattering processes. *Phys. Rev. A*, 75:013412, Jan 2007. doi: 10.1103/PhysRevA.75.013412. URL http://link.aps.org/doi/10.1103/PhysRevA.75.013412.

[118] COHERENT INC. Vitara, August 2016. URL https://www.coherent.com/downloads/COHR_Vitara_DS_0416revC_3.pdf. https://www.coherent.com/downloads/COHR_Vitara_DS_0416revC_3.pdf.

[119] Claude Rullière, editor. *Femtosecond Laser Pulses*. Advanced Texts in Physics. Springer-Verlag New York, Springer-Verlag New York, 2 edition, 2005. doi: 10.1007/b137908.

[120] COHERENT INC. Evolution, August 2016. URL https://www.coherent.com/downloads/Evolution_DS_0612RevD_2.pdf. https://www.coherent.com/downloads/Evolution_DS_0612RevD_2.pdf.

[121] COHERENT INC. Libra, August 2016. URL https://www.coherent.com/downloads/LibraSeries_CoherentDataSheet_revC_May2013_4.pdf. https://www.coherent.com/downloads/LibraSeries_CoherentDataSheet_revC_May2013_4.pdf.

[122] David F. Hotz. Gain narrowing in a laser amplifier. *Appl. Opt.*, 4(5):527–530, May 1965. doi: 10.1364/AO.4.000527. URL http://ao.osa.org/abstract.cfm?URI=ao-4-5-527.

[123] COHERENT INC. Operasolo, August 2016. URL https://www.coherent.com/downloads/OPerASolo_DSrevA_0512_1.pdf. https://www.coherent.com/downloads/OPerASolo_DSrevA_0512_1.pdf.

[124] Sebastian Uhlig. *Self-Organized Surface Structures with Ultrafast White-Light*. Springer Science + Business Media, 2015. doi: 10.1007/978-3-658-09894-0. URL http://dx.doi.org/10.1007/978-3-658-09894-0.

[125] Guozhen Yang and Y. R. Shen. Spectral broadening of ultrashort pulses in a nonlinear medium. *Opt. Lett.*, 9(11):510–512, Nov 1984. doi: 10.1364/OL.9.000510. URL http://ol.osa.org/abstract.cfm?URI=ol-9-11-510.

[126] M. Lewenstein, Ph. Balcou, M. Yu. Ivanov, Anne L'Huillier, and P. B. Corkum. Theory of high-harmonic generation by low-frequency laser fields. *Phys. Rev. A*, 49: 2117–2132, Mar 1994. doi: 10.1103/PhysRevA.49.2117. URL `http://link.aps.org/doi/10.1103/PhysRevA.49.2117`.

[127] S. Hüfner. *Photoelectron Spectroscopy: Principles and Applications*. Springer-Verlag (Heidelberg), 2003. URL `http://link.springer.com/book/10.1007%2F978-3-662-03209-1`.

[128] U. Becker and D.A. Shirley. *Vuv and Soft X-Ray Photoionization*. Interdisciplinary Contributions to Archaeology. Springer, 1996. ISBN 9780306450389. URL `http://books.google.de/books?id=m9chfY8jtxYC`.

[129] Y. Huismans, A. Rouzée, A. Gijsbertsen, J. H. Jungmann, A. S. Smolkowska, P. S. W. M. Logman, F. Lépine, C. Cauchy, S. Zamith, T. Marchenko, J. M. Bakker, G. Berden, B. Redlich, A. F. G. van der Meer, H. G. Muller, W. Vermin, K. J. Schafer, M. Spanner, M. Yu. Ivanov, O. Smirnova, D. Bauer, S. V. Popruzhenko, and M. J. J. Vrakking. Time-resolved holography with photoelectrons. *Science*, 331(6013):61–64, 2011. ISSN 0036-8075. doi: 10.1126/science.1198450. URL `http://science.sciencemag.org/content/331/6013/61`.

[130] E. Wells, C. E. Rallis, M. Zohrabi, R. Siemering, Bethany Jochim, P. R. Andrews, U. Ablikim, B. Gaire, S. De, K. D. Carnes, B. Bergues, R. de Vivie-Riedle, M. F. Kling, and I. Ben-Itzhak. Adaptive strong-field control of chemical dynamics guided by three-dimensional momentum imaging. *Nat Commun*, 4(2895):1–5, Dec 2013. URL `http://dx.doi.org/10.1038/ncomms3895`. Article.

[131] M E Corrales, J González-Vázquez, G Balerdi, R SoláI, R de Nalda, and L Bañares. Control of ultrafast molecular photodissociation by laser-field-induced potentials. *Nat Chem*, 6(9):785–790, Sep 2014. ISSN 1755-4330. URL `http://dx.doi.org/10.1038/nchem.2006`. Article.

[132] C. Bordas, F. Paulig, H. Helm, and D. L. Huestis. Photoelectron imaging spectrometry: Principle and inversion method. *Review of Scientific Instruments*, 67(6): 2257 – 2268, June 1996. URL `http://dx.doi.org/10.1063/1.1147044`.

[133] A T J B Eppink and D H Parker. Velocity map imaging of ions and electrons using electrostatic lenses: Application in photoelectron and photofragment ion imaging of molecular oxygen. *Review of Scientific Instruments*, 68(9):3477 – 3484, September 1997. URL `http://dx.doi.org/10.1063/1.1148310`.

[134] Alexander Kothe, Jan Metje, Martin Wilke, Alexandre Moguilevski, Nicholas Engel, Ruba Al-Obaidi, Clemens Richter, Ronny Golnak, Igor Yu. Kiyan, and Emad F.

Aziz. Time-of-flight electron spectrometer for a broad range of kinetic energies. *Review of Scientific Instruments*, 84(2):023106, 2013. doi: 10.1063/1.4791792. URL http://aip.scitation.org/doi/10.1063/1.4791792.

[135] J.J. Yeh and I. Lindau. Atomic subshell photoionization cross sections and asymmetry parameters. *Atomic Data and Nuclear Data Tables*, 32(1):1 – 155, 1985. ISSN 0092-640X. doi: 10.1016/0092-640X(85)90016-6. URL http://www.sciencedirect.com/science/article/pii/0092640X85900166.

[136] S Hara and M Nakamura. Determination of the photoionisation asymmetry parameter. *Journal of Physics B: Atomic and Molecular Physics*, 19(12):L467, 1986. URL http://stacks.iop.org/0022-3700/19/i=12/a=004.

[137] John C. Tully, R. Stephen Berry, and Bryan J. Dalton. Angular distribution of molecular photoelectrons. *Phys. Rev.*, 176:95–105, Dec 1968. doi: 10.1103/PhysRev.176.95. URL http://link.aps.org/doi/10.1103/PhysRev.176.95.

[138] P Kruit and F H Read. Magnetic field paralleliser for 2π electron-spectrometer and electron-image magnifier. *Journal of Physics E: Scientific Instruments*, 16(4):313, 1983. URL http://stacks.iop.org/0022-3735/16/i=4/a=016.

[139] Toshio Tsuboi, Emily Y. Xu, Young K. Bae, and Keith T. Gillen. Magnetic bottle electron spectrometer using permanent magnets. *Review of Scientific Instruments*, 59(8):1357–1362, 1988. doi: 10.1063/1.1139722. URL http://link.aip.org/link/?RSI/59/1357/1.

[140] M. Mucke, M. Förstel, T. Lischke, T. Arion, A. M. Bradshaw, and U. Hergenhahn. Performance of a short "magnetic bottle" electron spectrometer. *Review of Scientific Instruments*, 83(6):063106, 2012. doi: 10.1063/1.4729256. URL http://link.aip.org/link/?RSI/83/063106/1.

[141] M. H. Berntsen, O. Götberg, and O. Tjernberg. An experimental setup for high resolution 10.5 ev laser-based angle-resolved photoelectron spectroscopy using a time-of-flight electron analyzer. *Review of Scientific Instruments*, 82(9):095113, September 2011. doi: http://dx.doi.org/10.1063/1.3637464. URL http://scitation.aip.org/content/aip/journal/rsi/82/9/10.1063/1.3637464.

[142] Thomas Kunze. *Impulsabhängige, ultraschnelle Elektronendynamik an gestuften Oberflächen und topologischen Isolatoren untersucht mit winkelauflösender Flugzeitspektroskopie*. Dissertation, Freie Universität Berlin, 2014. URL http://www.dr.hut-verlag.de/978-3-8439-1885-5.html. http://www.dr.hut-verlag.de/978-3-8439-1885-5.html.

[143] SPECS GmbH. Themis 600, August 2016. URL http://www.specs.de/cms/front_content.php?idart=391. http://www.specs.de/cms/front_content.php?idart=391.

[144] G. C. Baldwin and S. I. Friedman. Time-of-flight electron velocity spectrometer. *Review of Scientific Instruments*, 38(4):519–531, 1967. doi: http://dx.doi.org/10.1063/1.1720752. URL http://scitation.aip.org/content/aip/journal/rsi/38/4/10.1063/1.1720752.

[145] A. M. Hudor. Fast electronics for time-of-flight measurements. *Review of Scientific Instruments*, 52(6):819–824, 1981. doi: http://dx.doi.org/10.1063/1.1136702. URL http://scitation.aip.org/content/aip/journal/rsi/52/6/10.1063/1.1136702.

[146] Surface Concept GmbH . Delay line detector, August 2016. URL http://www.surface-concept.com/downloads/info/Infoblatt%20Small%20DLDs.pdf. http://www.surface-concept.com/downloads/info/Infoblatt%20Small%20DLDs.pdf.

[147] HP Agilent. 8447f, August 2016. URL http://www.keysight.com/de/pd-1000001908%3Aepsg%3Apro-pn-8447F/preamplifier-and-power-amplifier?cc=DE&lc=ger&lsrch=true&searchT=8477F. http://www.keysight.com/de/pd-1000001908%3Aepsg%3Apro-pn-8447F/preamplifier-and-power-amplifier?cc=DE&lc=ger&lsrch=true&searchT=8477F.

[148] RoentDek Handels GmbH. fadc4, August 2016. URL http://www.roentdek.com/products/electronics_description/fADC4%20%20description.pdf. http://www.roentdek.com/products/electronics_description/fADC4%20%20description.pdf.

[149] Surface Concept GmbH. Sc-tdc-1000/02 d, August 2016. URL http://www.surface-concept.com/downloads/info/Datasheet_TDC.pdf. http://www.surface-concept.com/downloads/info/Datasheet_TDC.pdf.

[150] G. Da Costa, F. Vurpillot, A. Bostel, M. Bouet, and B. Deconihout. Design of a delay-line position-sensitive detector with improved performance. *Review of Scientific Instruments*, 76(1):013304, December 2005. doi: http://dx.doi.org/10.1063/1.1829975. URL http://scitation.aip.org/content/aip/journal/rsi/76/1/10.1063/1.1829975.

[151] Franziska Buchner, Andrea Lübcke, Nadja Heine, and Thomas Schultz. Time-resolved photoelectron spectroscopy of liquids. *Review of Scientific Instruments*,

81(11):113107, 2010. doi: 10.1063/1.3499240. URL http://link.aip.org/link/?RSI/81/113107/1.

[152] Yoshi-Ichi Suzuki, Kiyoshi Nishizawa, Naoya Kurahashi, and Toshinori Suzuki. Effective attenuation length of an electron in liquid water between 10 and 600 ev. *Phys. Rev. E*, 90:010302, Jul 2014. doi: 10.1103/PhysRevE.90.010302. URL http://link.aps.org/doi/10.1103/PhysRevE.90.010302.

[153] Stephan Thürmer, Robert Seidel, Manfred Faubel, Wolfgang Eberhardt, John C. Hemminger, Stephen E. Bradforth, and Bernd Winter. Photoelectron angular distributions from liquid water: Effects of electron scattering. *Phys. Rev. Lett.*, 111:173005, Oct 2013. doi: 10.1103/PhysRevLett.111.173005. URL http://link.aps.org/doi/10.1103/PhysRevLett.111.173005.

[154] S M Pimblott, J A LaVerne, and A Mozumder. Monte carlo simulation of range and energy deposition by electrons in gaseous and liquid water. *The Journal of Physical Chemistry*, 100(20):8595–8606, 1996. doi: 10.1021/jp9536559. URL http://dx.doi.org/10.1021/jp9536559.

[155] H. Tomita, M. Kai, T. Kusama, and A. Ito. Monte carlo simulation of physicochemical processes of liquid water radiolysis. *Radiation and Environmental Biophysics*, 36(2):105–116, 1997. ISSN 1432-2099. doi: 10.1007/s004110050061. URL http://dx.doi.org/10.1007/s004110050061.

[156] D. Emfietzoglou and M. Moscovitch. Inelastic collision characteristics of electrons in liquid water. *Nuclear Instruments and Methods in Physics Research Section B: Beam Interactions with Materials and Atoms*, 193(1–4):71 – 78, 2002. ISSN 0168-583X. doi: http://dx.doi.org/10.1016/S0168-583X(02)00729-2. URL http://www.sciencedirect.com/science/article/pii/S0168583X02007292.

[157] V. A. Semenenko, J. E. Turner, and T. B. Borak. Norec, a monte carlo code for simulating electron tracks in liquid water. *Radiation and Environmental Biophysics*, 42(3):213–217, 2003. ISSN 1432-2099. doi: 10.1007/s00411-003-0201-z. URL http://dx.doi.org/10.1007/s00411-003-0201-z.

[158] Manfred Faubel, Björn Steiner, and J. Peter Toennies. Photoelectron spectroscopy of liquid water, some alcohols, and pure nonane in free micro jets. *Journal of Chemical Physics*, 106:9013 – 9031, June 1997. URL http://dx.doi.org/10.1063/1.474034.

[159] B Winter, R Weber, W Widdra, M Dittmar, M Faubel, , and Hertel I V. Full valence band photoemission from liquid water using euv synchrotron radiation. *The Journal of Physical Chemistry A*, 108(14):2625–2632, 2004. doi: 10.1021/jp030263q. URL http://dx.doi.org/10.1021/jp030263q.

[160] Kiyoshi Nishizawa, Naoya Kurahashi, Kentarou Sekiguchi, Tomoya Mizuno, Yoshihiro Ogi, Takuya Horio, Masaki Oura, Nobuhiro Kosugi, and Toshinori Suzuki. High-resolution soft x-ray photoelectron spectroscopy of liquid water. *Phys. Chem. Chem. Phys.*, 13:413–417, 2011. doi: 10.1039/C0CP01636E. URL `http://dx.doi.org/10.1039/C0CP01636E`.

[161] Aster Kammrath, Jan R. R. Verlet, Graham B. Griffin, and Daniel M. Neumark. Photoelectron spectroscopy of large (water)n-(n=50–200) clusters at 4.7ev. *The Journal of Chemical Physics*, 125(7):076101, August 2006. doi: http://dx.doi.org/10.1063/1.2217745. URL `http://scitation.aip.org/content/aip/journal/jcp/125/7/10.1063/1.2217745`. 2006.

[162] Lei Ma, Kiran Majer, Fabien Chirot, and Bernd von Issendorff. Low temperature photoelectron spectra of water cluster anions. *The Journal of Chemical Physics*, 131(14):144303, 2009. doi: http://dx.doi.org/10.1063/1.3245859. URL `http://scitation.aip.org/content/aip/journal/jcp/131/14/10.1063/1.3245859`.

[163] D. W. Turner C. R. Brundle. High resolution molecular photoelectron spectroscopy. ii. water and deuterium oxide. *Proceedings of the Royal Society of London. Series A, Mathematical and Physical Sciences*, 307(1488):27–36, 1968. ISSN 00804630. URL `http://www.jstor.org/stable/2416184`.

[164] Naoya Kurahashi, Shutaro Karashima, Ying Tang, Takuya Horio, Bumaliya Abulimiti, Yoshi-Ichi Suzuki, Yoshihiro Ogi, Masaki Oura, and Toshinori Suzuki. Photoelectron spectroscopy of aqueous solutions: Streaming potentials of nax (x = cl, br, and i) solutions and electron binding energies of liquid water and x^-. *The Journal of Chemical Physics*, 140(17):174506, 2014. doi: http://dx.doi.org/10.1063/1.4871877. URL `http://scitation.aip.org/content/aip/journal/jcp/140/17/10.1063/1.4871877`.

[165] John R. Farrell and Peter McTigue. Precise compensating potential difference measurements with a voltaic cell. *Journal of Electroanalytical Chemistry and Interfacial Electrochemistry*, 139(1):37 – 56, 1982. ISSN 0022-0728. doi: http://dx.doi.org/10.1016/0022-0728(82)85102-4. URL `http://www.sciencedirect.com/science/article/pii/0022072882851024`.

[166] Q. Du, R. Superfine, E. Freysz, and Y. R. Shen. Vibrational spectroscopy of water at the vapor/water interface. *Phys. Rev. Lett.*, 70:2313–2316, Apr 1993. doi: 10.1103/PhysRevLett.70.2313. URL `http://link.aps.org/doi/10.1103/PhysRevLett.70.2313`.

[167] Masanari Nagasaka, Takaki Hatsui, Toshio Horigome, Yutaka Hamamura, and Nobuhiro Kosugi. Development of a liquid flow cell to measure soft x-ray absorption

in transmission mode: A test for liquid water. *Journal of Electron Spectroscopy and Related Phenomena*, 177(2–3):130 – 134, 2010. ISSN 0368-2048. doi: http://dx.doi.org/10.1016/j.elspec.2009.11.001. URL http://www.sciencedirect.com/science/article/pii/S0368204809002540. Water and Hydrogen Bonds.

[168] S Myneni, Y Luo, L Å Näslund, M Cavalleri, L Ojamäe, H Ogasawara, A Pelmenschikov, Ph Wernet, P Väterlein, C Heske, Z Hussain, L G M Pettersson, and A Nilsson. Spectroscopic probing of local hydrogen-bonding structures in liquid water. *Journal of Physics: Condensed Matter*, 14(8):L213, 2002. URL http://stacks.iop.org/0953-8984/14/i=8/a=106.

[169] Robert S. Weatherup, Baran Eren, Yibo Hao, Hendrik Bluhm, and Miquel B. Salmeron. Graphene membranes for atmospheric pressure photoelectron spectroscopy. *The Journal of Physical Chemistry Letters*, 7(9):1622–1627, 2016. doi: 10.1021/acs.jpclett.6b00640. URL http://dx.doi.org/10.1021/acs.jpclett.6b00640. PMID: 27082434.

[170] Kathrin M. Lange, Alexander Kothe, and Emad F. Aziz. Chemistry in solution: recent techniques and applications using soft x-ray spectroscopy. *Phys. Chem. Chem. Phys.*, 14:5331–5338, 2012. doi: 10.1039/C2CP24028A. URL http://dx.doi.org/10.1039/C2CP24028A.

[171] Alexander Kothe, Martin Wilke, Alexandre Moguilevski, Nicholas Engel, Bernd Winter, Igor Yu. Kiyan, and Emad F. Aziz. Charge transfer to solvent dynamics in iodide aqueous solution studied at ionization threshold. *Phys. Chem. Chem. Phys.*, 17:1918–1924, 2015. doi: 10.1039/C4CP02482F. URL http://dx.doi.org/10.1039/C4CP02482F.

[172] Kiyoshi Nishizawa, Keijiro Ohshimo, and Toshinori Suzuki. Vacuum ultraviolet and soft x-ray photoelectron spectroscopy of liquid beams using a hemispherical photoelectron spectrometer with a multistage differential pumping system. *Journal of the Chinese Chemical Society*, 60(12):1403–1410, 2013. ISSN 2192-6549. doi: 10.1002/jccs.201300513. URL http://dx.doi.org/10.1002/jccs.201300513.

[173] M. Faubel and Th Kisters. Non-equilibrium molecular evaporation of carboxylic acid dimers. *Nature*, 339(6225):527–529, Jun 1989. doi: 10.1038/339527a0. URL http://dx.doi.org/10.1038/339527a0.

[174] M. Faubel, S. Schlemmer, and J. P. Toennies. A molecular beam study of the evaporation of water from a liquid jet. *Zeitschrift für Physik D Atoms, Molecules and Clusters*, 10(2):269–277, 1988. ISSN 1431-5866. doi: 10.1007/BF01384861. URL http://dx.doi.org/10.1007/BF01384861.

[175] Kevin R. Wilson, Bruce S. Rude, Jared Smith, Chris Cappa, D. T. Co, R. D. Schaller, M. Larsson, T. Catalano, and R. J. Saykally. Investigation of volatile liquid surfaces by synchrotron x-ray spectroscopy of liquid microjets. *Review of Scientific Instruments*, 75(3):725–736, 2004. doi: http://dx.doi.org/10.1063/1.1645656. URL `http://scitation.aip.org/content/aip/journal/rsi/75/3/10.1063/1.1645656`.

[176] Jared D. Smith, Christopher D. Cappa, Kevin R. Wilson, Ronald C. Cohen, Phillip L. Geissler, and Richard J. Saykally. Unified description of temperature-dependent hydrogen-bond rearrangements in liquid water. *Proceedings of the National Academy of Sciences of the United States of America*, 102(40):14171–14174, 2005. doi: 10.1073/pnas.0506899102. URL `http://www.pnas.org/content/102/40/14171.abstract`.

[177] Kevin R. Wilson, Bruce S. Rude, Tony Catalano, Richard D. Schaller, James G. Tobin, Dick T. Co, and R. J. Saykally. X-ray spectroscopy of liquid water microjets. *The Journal of Physical Chemistry B*, 105(17):3346–3349, 2001. doi: 10.1021/jp010132u. URL `http://dx.doi.org/10.1021/jp010132u`.

[178] Teledyne Isco. 500d syringe pump, October 2016. URL `http://www.isco.com/products/products3.asp?PL=1051020`. `http://www.isco.com/products/products3.asp?PL=1051020`.

[179] Thorlabs. Polaris^{TM} line, October 2016. URL `https://www.thorlabs.com/navigation.cfm?guide_ID=2368`. `https://www.thorlabs.com/navigation.cfm?guide_ID=2368`.

[180] Alexander Kothe. *Charge Transfer to Solvent Dynamics in Iodide Aqueous Solution Studied at Ionization Threshold*. PhD thesis, Freie Universität Berlin, 2015.

[181] M Wilke, R Al-Obaidi, A Moguilevski, A Kothe, N Engel, J Metje, I Yu Kiyan, and E F Aziz. Laser-assisted electron scattering in strong-field ionization of dense water vapor by ultrashort laser pulses. *New J. Phys.*, 16(8):083032, 2014. doi: 10.1088/1367-2630/16/8/083032. URL `http://stacks.iop.org/1367-2630/16/i=8/a=083032`.

[182] M. Wilke, R. Al-Obaidi, I. Yu. Kiyan, and E. F. Aziz. Multiplateau structure in photoemission spectra of strong-field ionization of dense media. *Phys. Rev. A*, 94:033423, Sep 2016. doi: 10.1103/PhysRevA.94.033423. URL `http://link.aps.org/doi/10.1103/PhysRevA.94.033423`.

[183] S. Düsterer, H. Schwoerer, W. Ziegler, C. Ziener, and R. Sauerbrey. Optimization of euv radiation yield from laser-produced plasma. *Applied Physics B*, 73(7):693–698,

2001. ISSN 1432-0649. doi: 10.1007/s003400100730. URL http://dx.doi.org/10.1007/s003400100730.

[184] S. J. McNaught, J. Fan, E. Parra, and H. M. Milchberg. A pump–probe investigation of laser-droplet plasma dynamics. *Applied Physics Letters*, 79(25):4100–4102, 2001. doi: http://dx.doi.org/10.1063/1.1426266. URL http://scitation.aip.org/content/aip/journal/apl/79/25/10.1063/1.1426266.

[185] Shuai Yuan, Tiejun Wang, Yoshiaki Teranishi, Aravindan Sridharan, Sheng Hsien Lin, Heping Zeng, and See Leang Chin. Lasing action in water vapor induced by ultrashort laser filamentation. *Applied Physics Letters*, 102(22):224102, 2013. doi: http://dx.doi.org/10.1063/1.4809585. URL http://scitation.aip.org/content/aip/journal/apl/102/22/10.1063/1.4809585.

[186] D. Mathur, F. A. Rajgara, A. K. Dharmadhikari, and J. A. Dharmadhikari. Strong-field ionization of water by intense few-cycle laser pulses. *Phys. Rev. A*, 78:023414, Aug 2008. doi: 10.1103/PhysRevA.78.023414. URL http://link.aps.org/doi/10.1103/PhysRevA.78.023414.

[187] S. Petretti, A. Saenz, A. Castro, and P. Decleva. Water Molecules in Ultrashort Intense Laser Fields. *ArXiv e-prints*, page arXiv:1112.2618, December 2011.

[188] Simon Petretti, Alejandro Saenz, Alberto Castro, and Piero Decleva. Water molecules in ultrashort intense laser fields. *Chemical Physics*, 414:45 – 52, 2013. ISSN 0301-0104. doi: http://dx.doi.org/10.1016/j.chemphys.2012.01.011. URL http://www.sciencedirect.com/science/article/pii/S0301010412000237. Attosecond spectroscopy.

[189] Ruba Al-Obaidi. *Space-Charge effect in strong field ionization processes in dense media*. PhD thesis, Freie Universität Berlin, 2016.

[190] U. Eichmann, M. Dörr, H. Maeda, W. Becker, and W. Sandner. Collective multi-electron tunneling ionization in strong fields. *Phys. Rev. Lett.*, 84:3550–3553, Apr 2000. doi: 10.1103/PhysRevLett.84.3550. URL http://link.aps.org/doi/10.1103/PhysRevLett.84.3550.

[191] Natalie Preissler, Franziska Buchner, Thomas Schultz, and Andrea Lübcke. Electrokinetic charging and evidence for charge evaporation in liquid microjets of aqueous salt solution. *The Journal of Physical Chemistry B*, 117(8):2422–2428, 2013. doi: 10.1021/jp304773n. URL http://dx.doi.org/10.1021/jp304773n. PMID: 23330711.

[192] Daniel N. Kelly, Royce K. Lam, Andrew M. Duffin, and Richard J. Saykally. Exploring solid/aqueous interfaces with ultradilute electrokinetic analysis of liquid

microjets. *The Journal of Physical Chemistry C*, 117(24):12702–12706, 2013. doi: 10.1021/jp403583r. URL http://dx.doi.org/10.1021/jp403583r.

[193] K.H. Tan, C.E. Brion, Ph.E. Van der Leeuw, and M.J. van der Wiel. Absolute oscillator strengths (10–60 ev) for the photoabsorption, photoionisation and fragmentation of h20s. *Chemical Physics*, 29(3):299 – 309, 1978. ISSN 0301-0104. doi: http://dx.doi.org/10.1016/0301-0104(78)85080-0. URL http://www.sciencedirect.com/science/article/pii/0301010478850800.

[194] Stephane Klein, Elise Kochanski, Alain Strich, and Andrzej J. Sadlej. Electric properties of the water molecule in 1a1, 1b1, and 3b1 electronic states: Refined casscf and caspt2 calculations. *Theoretica chimica acta*, 94(2):75–91, 1996. ISSN 1432-2234. doi: 10.1007/BF00194933. URL http://dx.doi.org/10.1007/BF00194933.

[195] Atsunori Danjo and Hiroyuki Nishimura. Elastic scattering of electrons from h2o molecule. *Journal of the Physical Society of Japan*, 54(4):1224–1227, 1985. doi: 10.1143/JPSJ.54.1224. URL http://dx.doi.org/10.1143/JPSJ.54.1224.

[196] H Cho, Y S Park, H Tanaka, and S J Buckman. Measurements of elastic electron scattering by water vapour extended to backward angles. *Journal of Physics B: Atomic, Molecular and Optical Physics*, 37(3):625, 2004. URL http://stacks.iop.org/0953-4075/37/i=3/a=008.

[197] B. Abel, U. Buck, A. L. Sobolewski, and W. Domcke. On the nature and signatures of the solvated electron in water. *Phys. Chem. Chem. Phys.*, 14:22–34, 2012. doi: 10.1039/C1CP21803D. URL http://dx.doi.org/10.1039/C1CP21803D.

[198] James V. Coe, Alan D. Earhart, Michael H. Cohen, Gerald J. Hoffman, Harry W. Sarkas, and Kit H. Bowen. Using cluster studies to approach the electronic structure of bulk water: Reassessing the vacuum level, conduction band edge, and band gap of water. *The Journal of Chemical Physics*, 107(16):6023–6031, 1997. doi: http://dx.doi.org/10.1063/1.474271. URL http://scitation.aip.org/content/aip/journal/jcp/107/16/10.1063/1.474271.

[199] U Saalmann, Ch Siedschlag, and J M Rost. Mechanisms of cluster ionization in strong laser pulses. *Journal of Physics B: Atomic, Molecular and Optical Physics*, 39(4):R39, 2006. URL http://stacks.iop.org/0953-4075/39/i=4/a=R01.

[200] M. B. Smirnov and V. P. Krainov. Ionization of cluster atoms in a strong laser field. *Phys. Rev. A*, 69:043201, Apr 2004. doi: 10.1103/PhysRevA.69.043201. URL http://link.aps.org/doi/10.1103/PhysRevA.69.043201.

[201] Shuang Men, Kevin R. J. Lovelock, and Peter Licence. Directly probing the effect of the solvent on a catalyst electronic environment using x-ray photoelectron

spectroscopy. *RSC Adv.*, 5:35958–35965, 2015. doi: 10.1039/C5RA04662A. URL http://dx.doi.org/10.1039/C5RA04662A.

[202] R Weber, B Winter, P M Schmidt, W Widdra, I V Hertel, M Dittmar, , and M Faubel. Photoemission from aqueous alkali-metal-iodide salt solutions using euv synchrotron radiation. *The Journal of Physical Chemistry B*, 108(15):4729–4736, 2004. doi: 10.1021/jp030776x. URL http://dx.doi.org/10.1021/jp030776x.

[203] R. A. Crowell, , and D. M. Bartels. Multiphoton ionization of liquid water with 3.0-5.0 ev photons. *The Journal of Physical Chemistry*, 100(45):17940–17949, 1996. doi: 10.1021/jp9610978. URL http://dx.doi.org/10.1021/jp9610978.

[204] C. Pépin, D. Houde, H. Remita, T. Goulet, and J.-P. Jay-Gerin. Evidence for resonance-enhanced multiphoton ionization of liquid water using 2 ev laser light: Variation of hydrated electron absorbance with femtosecond pulse intensity. *Phys. Rev. Lett.*, 69:3389–3392, Dec 1992. doi: 10.1103/PhysRevLett.69.3389. URL http://link.aps.org/doi/10.1103/PhysRevLett.69.3389.

[205] Joseph Callaway. Electron-hydrogen scattering just above the ionization threshold. *Physics Letters A*, 100(8):415 – 418, 1984. ISSN 0375-9601. doi: http://dx.doi.org/10.1016/0375-9601(84)90633-9. URL http://www.sciencedirect.com/science/article/pii/0375960184906339.

[206] J. L. Chaloupka, R. Lafon, L. F. DiMauro, P. Agostini, and K. C. Kulander. Strong-field double ionization of rare gases. *Opt. Express*, 8(7):352–357, Mar 2001. doi: 10.1364/OE.8.000352. URL http://www.opticsexpress.org/abstract.cfm?URI=oe-8-7-352.

[207] L-P Oloff, M Oura, K Rossnagel, A Chainani, M Matsunami, R Eguchi, T Kiss, Y Nakatani, T Yamaguchi, J Miyawaki, M Taguchi, K Yamagami, T Togashi, T Katayama, K Ogawa, M Yabashi, and T Ishikawa. Time-resolved haxpes at sacla: probe and pump pulse-induced space-charge effects. *New Journal of Physics*, 16(12):123045, 2014. URL http://stacks.iop.org/1367-2630/16/i=12/a=123045.

[208] R Al-Obaidi, M Wilke, M Borgwardt, J Metje, A Moguilevski, N Engel, D Tolksdorf, A Raheem, T Kampen, S Mähl, I Yu Kiyan, and E F Aziz. Ultrafast photoelectron spectroscopy of solutions: space-charge effect. *New Journal of Physics*, 17(9):093016, 2015. doi: 10.1088/1367-2630/17/9/093016. URL http://stacks.iop.org/1367-2630/17/i=9/a=093016.

[209] L.-P. Oloff, K. Hanff, A. Stange, G. Rohde, F. Diekmann, M. Bauer, and K. Rossnagel. Pump laser-induced space-charge effects in hhg-driven time- and angle-resolved photoelectron spectroscopy. *Journal of Applied Physics*, 119(22):225106,

2016. doi: http://dx.doi.org/10.1063/1.4953643. URL http://scitation.aip.org/content/aip/journal/jap/119/22/10.1063/1.4953643.

[210] Ocean Optics, Inc. Usb2000+, October 2016. URL http://oceanoptics.com/product/usb2000-custom/. http://oceanoptics.com/product/usb2000-custom/.

[211] F. Ossler and M. Aldén. Measurements of picosecond laser induced fluorescence from gas phase 3-pentanone and acetone: Implications to combustion diagnostics. *Applied Physics B*, 64(4):493–502, 1997. ISSN 1432-0649. doi: 10.1007/s003400050205. URL http://dx.doi.org/10.1007/s003400050205.

[212] Noel S. Bayliss and Eion G. McRae. Solvent effects in the spectra of acetone, crotonaldehyde, nitromethane and nitrobenzene. *The Journal of Physical Chemistry*, 58(11):1006–1011, 1954. doi: 10.1021/j150521a018. URL http://dx.doi.org/10.1021/j150521a018.

[213] M. Nobre, A. Fernandes, F. Ferreira da Silva, R. Antunes, D. Almeida, V. Kokhan, S. V. Hoffmann, N. J. Mason, S. Eden, and P. Limao-Vieira. The vuv electronic spectroscopy of acetone studied by synchrotron radiation. *Phys. Chem. Chem. Phys.*, 10:550–560, 2008. doi: 10.1039/B708580J. URL http://dx.doi.org/10.1039/B708580J.

[214] Imke B. Müller and Lorenz S. Cederbaum. Ionization and double ionization of small water clusters. *The Journal of Chemical Physics*, 125(20):204305, 2006. doi: http://dx.doi.org/10.1063/1.2357921. URL http://scitation.aip.org/content/aip/journal/jcp/125/20/10.1063/1.2357921.

[215] P. Linusson, M. Stenrup, Å. Larson, E. Andersson, F. Heijkenskjöld, P. Andersson, J. H. D. Eland, L. Karlsson, J.-E. Rubensson, and R. Feifel. Double photoionization of alcohol molecules. *Phys. Rev. A*, 80:032516, Sep 2009. doi: 10.1103/PhysRevA.80.032516. URL http://link.aps.org/doi/10.1103/PhysRevA.80.032516.

[216] Ralph Schlipper, Robert Kusche, Bernd von Issendorff, and Hellmut Haberland. Multiple excitation and lifetime of the sodium cluster plasmon resonance. *Phys. Rev. Lett.*, 80:1194 – 1197, Feb 1998. doi: 10.1103/PhysRevLett.80.1194. URL http://link.aps.org/doi/10.1103/PhysRevLett.80.1194.

[217] E. S. Efimenko, Yu. A. Malkov, A. A. Murzanev, and A. N. Stepanov. Femtosecond laser pulse-induced breakdown of a single water microdroplet. *J. Opt. Soc. Am. B*, 31(3):534–541, Mar 2014. doi: 10.1364/JOSAB.31.000534. URL http://josab.osa.org/abstract.cfm?URI=josab-31-3-534.

[218] Lewi Tonks and Irving Langmuir. Oscillations in ionized gases. *Phys. Rev.*, 33: 195–210, Feb 1929. doi: 10.1103/PhysRev.33.195. URL `http://link.aps.org/doi/10.1103/PhysRev.33.195`.

[219] Alexander Kothe, Martin Wilke, Alexandre Moguilevski, Nicholas Engel, Bernd Winter, Igor Yu. Kiyan, and Emad F. Aziz. Reply to the 'comment on "charge transfer to solvent dynamics in iodide aqueous solution studied at ionization threshold"' by a. lubcke and h.-h. ritze, phys. chem. chem. phys., 2015, 17, doi: 10.1039/c5cp00346f. *Phys. Chem. Chem. Phys.*, 17:18195–18196, 2015. doi: 10.1039/C5CP01804H. URL `http://dx.doi.org/10.1039/C5CP01804H`.

[220] Mario Borgwardt, Martin Wilke, Thorsten Kampen, Sven Mähl, Wanchun Xiang, Leone Spiccia, Kathrin M. Lange, Igor Yu. Kiyan, and Emad F. Aziz. Injection kinetics and electronic structure at the n719/tio2 interface studied by means of ultrafast xuv photoemission spectroscopy. *J. Phys. Chem. C*, 119(17):9099–9107, 2015. doi: 10.1021/acs.jpcc.5b01216. URL `http://dx.doi.org/10.1021/acs.jpcc.5b01216`.

[221] M. Borgwardt, M. Wilke, T. Kampen, S. Mähl, W. Xiang, L. Spiccia, K.M. Lange, I.Y. Kiyan, and E.F. Aziz. Capturing charge transfer dynamics with ultrafast time-resolved xuv photoelectron spectroscopy at dye-semiconductor interfaces. *EU PVSEC Proceedings*, 2015, 2015. doi: 10.4229/EUPVSEC20152015-1AO.1.2. URL `https://doi.org/10.4229/EUPVSEC20152015-1AO.1.2`.

[222] Mario Borgwardt, Martin Wilke, Thorsten Kampen, Sven Mähl, Manda Xiao, Leone Spiccia, Kathrin M. Lange, Igor Yu Kiyan, and Emad F. Aziz. Charge transfer dynamics at dye-sensitized zno and tio2 interfaces studied by ultrafast xuv photoelectron spectroscopy. *Scientific Reports*, 6:24422 EP –, Apr 2016. doi: 10.1038/srep24422. URL `http://dx.doi.org/10.1038/srep24422`. Article.

[223] Mario Borgwardt, Martin Wilke, Igor Yu. Kiyan, and Emad F. Aziz. Ultrafast excited states dynamics of [ru(bpy)3]2+ dissolved in ionic liquids. *Phys. Chem. Chem. Phys.*, 18:28893–28900, 2016. doi: 10.1039/C6CP05655E. URL `http://dx.doi.org/10.1039/C6CP05655E`.

[224] Alexandre Moguilevski, Martin Wilke, Gilbert Grell, Sergey I. Bokarev, Saadullah G. Aziz, Nicholas Engel, Azhr A. Raheem, Oliver Kühn, Igor Yu. Kiyan, and Emad F. Aziz. Ultrafast spin crossover in [feii(bpy)3]2+: Revealing two competing mechanisms by extreme ultraviolet photoemission spectroscopy. *ChemPhysChem*, 18(5):465–469, 2017. ISSN 1439-7641. doi: 10.1002/cphc.201601396. URL `http://dx.doi.org/10.1002/cphc.201601396`.

[225] Keisaku Yamane, Zhigang Zhang, Kazuhiko Oka, Ryuji Morita, Mikio Yamashita, and Akira Suguro. Optical pulse compression to 3.4fs in the monocycle region by

feedback phase compensation. *Opt. Lett.*, 28(22):2258–2260, Nov 2003. doi: 10.1364/OL.28.002258. URL http://ol.osa.org/abstract.cfm?URI=ol-28-22-2258.

[226] A. Y. Klimenko. Symmetric and antisymmetric forms of the pauli master equation. *Scientific Reports*, 6:29942, jul 2016. doi: 10.1038/srep29942. URL http://dx.doi.org/10.1038/srep29942.

[227] Andrea Lubcke, Franziska Buchner, Nadja Heine, Ingolf V. Hertel, and Thomas Schultz. Time-resolved photoelectron spectroscopy of solvated electrons in aqueous nai solution. *Phys. Chem. Chem. Phys.*, 12:14629–14634, 2010. doi: 10.1039/C0CP00847H. URL http://dx.doi.org/10.1039/C0CP00847H.

[228] Ph Wernet, K. Kunnus, I. Josefsson, I. Rajkovic, W. Quevedo, M. Beye, S. Schreck, S. Grubel, M. Scholz, D. Nordlund, W. Zhang, R. W. Hartsock, W. F. Schlotter, J. J. Turner, B. Kennedy, F. Hennies, F. M. F. de Groot, K. J. Gaffney, S. Techert, M. Odelius, and A. Fohlisch. Orbital-specific mapping of the ligand exchange dynamics of fe(co)5 in solution. *Nature*, 520(7545):78–81, Apr 2015. ISSN 0028-0836. URL http://dx.doi.org/10.1038/nature14296. Letter.

[229] Ute B. Cappel, Stefan Plogmaker, Joachim A. Terschlusen, Torsten Leitner, Erik M. J. Johansson, Tomas Edvinsson, Anders Sandell, Olof Karis, Hans Siegbahn, Svante Svensson, Nils Martensson, Hakan Rensmo, and Johan Soderstrom. Electronic structure dynamics in a low bandgap polymer studied by time-resolved photoelectron spectroscopy. *Phys. Chem. Chem. Phys.*, 18:21921–21929, 2016. doi: 10.1039/C6CP04136A. URL http://dx.doi.org/10.1039/C6CP04136A.

[230] T. Hertel, E. Knoesel, M. Wolf, and G. Ertl. Ultrafast electron dynamics at cu(111): Response of an electron gas to optical excitation. *Phys. Rev. Lett.*, 76:535–538, Jan 1996. doi: 10.1103/PhysRevLett.76.535. URL http://link.aps.org/doi/10.1103/PhysRevLett.76.535.

Abstract

The collective strong-field photoionization effects in dilute and dense gases and liquids illuminated by short infrared laser pulses of high intensity are investigated by means of photoemission spectroscopy. By employing the liquid microjet technique enabling liquid-phase spectroscopy in the vacuum, the vicinity of liquid water, acetone, and ethanol and a large variety of respective gas target densities were examined and the influence of the molecular structure on the final emission studied.

This unique combination of experimental methods allows to study how the emission undergoes a tremendous change upon increasing the target density of the illuminated gas sample. These changes were addressed by models describing collective multi-particle ionization effects. In particular, the contribution of electrons ionized from the parent atom scattering on the potential of neighboring particles in the presence of the driving laser field and as a consequence absorbing or emitting a large number of photons via inelastic laser-assisted scattering was determined. This scattering process dramatically changes the emission characteristics of strong-field ionized electrons with respect to the non-collective effects as above-threshold ionization and high-order above-threshold ionization giving rise to the superimposed multi-plateau structure including corresponding semiclassical electron energy cut-offs. The proposed semiclassical models and calculations lead to a simple and comprehensible description of such non-linear processes and represent a significant breakthrough in the description of strong-field ionization of dense target systems by extending single-particle ionization models towards collective interactions within short laser pulses.

Additionally, the strong-field emission from the liquid phase was studied and shown to be in agreement with results obtained from the dense gas limit by including more than one scattering event of photoionized electrons enabled by the orders of magnitude higher density in the condensed phase. Beyond collective electron effects, excitation of the liquid phase by strong laser fields was studied by means of time-resolved XUV photoelectron spectroscopy. Here, fingerprints of a strong nuclear response as plasma formation induced by the efficient ionization process in high-intensity fields were observed.

Finally, numerical methods of data evaluation for transient photoelectron spectroscopy were developed enabling to study effects occurring on time-scales smaller than the system response which are inherently inaccessible by evaluation techniques employed in recent publications.

Kurzzusammenfassung

Kollektive Photoionisationseffekte in dünnen und dichten Gasen sowie in Flüssigkeiten, induziert durch kurze infrarote Laserpulse großer Intensität, wurden mittels Photoemissionspektroskopie untersucht. Der Einsatz der *microjet*-Technik ermöglichte Flüssigkeitsspektroskopie im Vakuum, wodurch die Umgebung von flüssigem Wasser, Aceton und Ethanol und somit der Einfluss, der entsprechenden Gasdichten und Molekularstrukturen auf die Elektronenemission, untersucht werden konnte.

Diese einzigartige Kombination experimenteller Methoden ermöglicht zu untersuchen, warum und wie sich die Elektronenemission, hervorgerufen durch Beleuchtung mit starken Laserpulsen, drastisch mit der Gasdichte ändert. Diese Änderungen wurden mithilfe kollektiver Ionisationsmodelle interpretiert. Im Besonderen der Einfluss von Elektronen, die nach der Ionisation in der Anwesenheit des Laserpulses an Nachbarpotentialen streuen und dadurch in der Lage sind, viele Photonen durch laserunterstützte Streuung zu absorbieren oder zu emittieren, wurde bestimmt. Diese Streuprozesse verändern drastisch die Elektronenemission im Vergleich zu nicht-kollektiven Ionisationsprozessen, wie z.B. *above-threshold ionization* und *high-order above-threshold ionization*, und überlagern deren Emission mit einer Multiplateaustruktur inklusive entsprechender Elektronenenergielimits. Die hier vorgeschlagenen semiklassischen Modelle und Berechnungen erlauben eine einfache und verständliche Beschreibung dieser nichtlinearen Prozesse und stellen somit einen Durchbruch in der Erweiterung der Einzelionisationsbeschreibung hin zu kollektiven Wechselwirkungen in kurzen Laserpulsen dar.

Zusätzlich wurde die Hochfeldionisation in Flüssigkeiten untersucht und gezeigt, dass diese mit den Ergebnissen aus der vorherigen Studie in dichten Gasen im Einklang steht, insofern mehr als ein Streuereignis, ermöglicht durch die erheblich höhere Dichte der Flüssigkeit, berücksichtigt wird. Unabhängig von den kollektiven Elektroneneffekten wurde die Anregung der Flüssigkeit durch starke Laserpulse, gemessen mittels zeitaufgelöster Photoelektronenspektroskopie, untersucht. Dabei wurden Hinweise auf eine starke Reaktion des Nukleus, ausgelöst durch die hocheffiziente Hochfeldionisation, gefunden.

Abschließend wurden numerische Methoden zur Datenauswertung von zeitaufgelöster Photoelektronenspektroskopie entwickelt, die ermöglichen, Effekte zu studieren, die innerhalb kürzerer Zeitskalen auftreten als die Zeitauflösung des Systems eigentlich zulässt. Die Untersuchung dieser Effekte ist nicht durch herkömmliche und in aktuellen Publikationen verwendete Methoden möglich.

Publications

1. M. Wilke, R. Al-Obaidi, I. Yu. Kiyan, and E. F. Aziz
   Multiplateau structure in photoemission spectra of strong-field ionization of dense media
   Phys. Rev. A **94**, 033423 (2016), doi:10.1103/PhysRevA.94.033423

2. M. Wilke, R. Al-Obaidi, A. Moguilevski, A. Kothe, N. Engel, J. Metje, I. Yu. Kiyan, and E. F. Aziz
   Laser-assisted electron scattering in strong-field ionization of dense water vapor by ultrashort laser pulses
   New J. Phys., **16**, 083032 (2014), doi:10.1088/1367-2630/16/8/083032

3. A. Moguilevski, M. Wilke, G. Grell, S. I. Bokarev, S. G. Aziz, N. Engel, A. Raheem, O. Kühn, I. Yu. Kiyan, and E. F. Aziz
   Ultrafast Spin Crossover in $[Fe^{II}(bpy)_3]^{2+}$: Revealing Two Competing Mechanisms by Extreme Ultraviolet Photoemission Spectroscopy
   ChemPhysChem, **18** 465-469 (2017), doi:10.1002/cphc.201601396

4. M. Borgwardt, M. Wilke, I. Yu. Kiyan and E. F. Aziz
   Ultrafast excited states dynamics of [Ru(bpy)3]2+ dissolved in ionic liquids
   Phys. Chem. Chem. Phys., **18**, 28893-28900 (2016), doi:10.1039/C6CP05655E

5. M. Borgwardt, M. Wilke, T. Kampen, S. Mähl, M. Xiao, L. Spiccia, K. M. Lange, I. Yu. Kiyan, and E F. Aziz
   Charge Transfer Dynamics at Dye-Sensitized ZnO and TiO2 Interfaces Studied by Ultrafast XUV Photoelectron Spectroscopy
   Sci. Rep., **6**, 24422 (2016), doi:10.1038/srep24422

6. M. Borgwardt, M. Wilke, T. Kampen, S. Mähl, M. Xiao, L. Spiccia, K. M. Lange, I. Yu. Kiyan, and E F. Aziz
   Capturing Charge Transfer Dynamics with Ultrafast Time-Resolved XUV Photoelectron Spectroscopy at Dye - Semiconductor Interfaces
   Proceedings EUPVSEC (2015), doi:10.4229/EUPVSEC20152015-1AO.1.2

7. R. Al-Obaidi, M. Wilke, M. Borgwardt, J. Metje, A. Moguilevski, N. Engel, D. Tolksdorf, A. Raheem, T. Kampen, S. Mähl, I. Yu. Kiyan, and E. F. Aziz

Ultrafast photoelectron spectroscopy of solutions: space-charge effect
New J. Phys., **17**, 093016 (2015), doi:10.1088/1367-2630/17/9/093016

8. M. Borgwardt, M. Wilke, T. Kampen, S. Mähl, M. Xiao, L. Spiccia, K. M. Lange, I. Yu. Kiyan, and E F. Aziz
Injection Kinetics and Electronic Structure at the N719/TiO2 Interface Studied by Means of Ultrafast XUV Photoemission Spectroscopy
J. Phys. Chem. C, **119**, 9099-9107 (2015), doi:10.1021/acs.jpcc.5b01216

9. A. Kothe, M. Wilke, A. Moguilevski, N. Engel, B. Winter, I. Yu. Kiyan, and E. F. Aziz
Reply to the "Comment on 'Charge Transfer to Solvent Dynamics in Iodide Aqueous Solution Studied at Ionization Threshold'" by A. Lübcke and H.-H. Ritze, Phys. Chem. Chem. Phys., 2015, 17, DOI: 10.1039/C5CP00346F
Phys. Chem. Chem. Phys., **17**, 18195-18196 (2015), doi:10.1039/C5CP01804H

10. A. Kothe, M. Wilke, A. Moguilevski, N. Engel, B. Winter, I. Yu. Kiyan, and E. F. Aziz
Charge transfer to solvent dynamics in iodide aqueous solution studied at ionization threshold
Phys. Chem. Chem. Phys., **17**, 1918-1924 (2015), doi:10.1039/C4CP02482F

11. J. Metje, M. Borgwardt, A. Moguilevski, A. Kothe, N. Engel, M. Wilke, R. Al-Obaidi, D. Tolksdorf, A. Firsov, M. Brzhezinskaya, A. Erko, I. Kiyan and E. F. Aziz
Monochromatization of femtosecond XUV light pulses with the use of reflection zone plates
Opt. Express, **22**, 10747–60, (2014), doi:10.1364/OE.22.010747

12. A. Kothe, J. Metje, M. Wilke, A. Moguilevski, N. Engel, R. Al-Obaidi, C. Richter, R. Golnak, I. Yu. Kiyan, and E. F. Aziz
Time-of-flight electron spectrometer for a broad range of kinetic energies
Rev. Sci. Instrum., **84**, 023106 (2013), doi:10.1063/1.4791792

Author contributions

- Articles 1, 2: M. W. designed and carried out the experiment, analyzed the data, prepared figures, and wrote the manuscript.

- Article 3: M. W. carried out the experiment, analyzed the data, and prepared figures. Furthermore M. W. took part in the interpretation of the data and discussion and revision of the article.

- Articles 4, 5, 6, 7, 8, 9, 10, 11, 12: M. W. took part in the experiment and the data analysis. Furthermore M. W. took part in the interpretation of the data and discussion and revision of the article.

Acknowledgments

Being able to work as a physicist in a modern field of fundamental as well as applied sciences resulting in the completion of a PhD thesis does not only require working in an highly stimulating professional environment but as well working as part of a team to succeed. After 21 years of consecutive education there are more people to acknowledge than can be written here. Of my co-workers I especially would like to thank ...

... Prof. Dr. Emad Aziz, for giving me the opportunity to join his team, being unconditionally supportive for new ideas and development in a scientific, professional, and human context.

... Prof. Dr. Ludger Wöste, for the co-supervision of this thesis, for being my mentor in the first year at the university, and for the shared time and interesting experiments with lasers during my time in the AG Vorlesung.

... Dr. Igor Kiyan, for teaching me the basis of scientific work and supporting me in all my projects. Due to his help, experience, and knowledge a huge progress was achieved.

... Mario Borgwardt for joining me in experiments, data evaluation, and scientific discussions. Pushing each others limits, I gained a huge amount of knowledge and experience to solve all kinds of problems. Working with him led to the most efficient, productive, and joyful time during my PhD.

... Ruba Al-Obaidi for tackling all technical and scientific problems in our everyday life. Working as a team allowed us to obtain new knowledge in the field of strong-field interaction. Talking about the problems of the world from different points of view made us more open in general.

... Alexander Kothe for introducing me into the group and taking me metaphorically by the hand when I was still a novice. His knowledge about technical issues and their solutions significantly reduced the amount of avoidable errors in our life.

... Alexandre Moguilevski for being always available and supportive to all group members including me. His knowledge about laser physics and technical realizations was always the basis of experimental success. Tackling together one of the largest projects ever done in the group was an interesting experience that pushed me to new limits.

... Jan Metje, Nicholas Engel, Dr. Christoph Merschjann, Azhr Raheem, and Daniel Tolksdorf for fruitful discussions and many pleasant moments during long beam times as well as after work meetings.

... the BESSY team and the remaining members of AG Aziz, especially Tim Brandenburg, Kaan Atak, Ronny Golnak, Bernd Winter, Robert Seidel, and all others for support during the work and socializing after-work.

... the former and current members of AG Vorlesung, especially the heads Dr. Dirk Schwarzhans, Klaus Molkenthin, and Thomas Roos and the students, Finn, Nils, Christian, Olof, Larissa, Mark, Philip, and all others for introducing me to the fascination of physics.

Furthermore I'd like to thank my (German) family and friends:

Ohne eure Unterstützung wäre ich niemals dazu gekommen, diesen Weg zu beschreiten. Ihr habt mir immer Rückhalt gegeben, und auch nach Wochen harter Arbeit dafür gesorgt, dass mir niemals die Lust verging, jeden Tag aufs neue mit besonderem Vergnügen und Vorfreude zu erleben. Danken möchte ich hier vor allem...

...meiner Mutter, für den unerschöpflichen Rückhalt, für die vielen gemeinsam erlebten Stunden, für die Energie die sie jederzeit auf andere Menschen um sich herum überträgst.

...meinem Vater, der, auch in schwierigen Zeiten immer ein Rettungsanker in größter Not ist und der mich in jeder Form der Selbstverwirklichung unterstützt hat.

...meiner Schwester, die der quirlige Ursprung nahezu jeder Form von Abwechslung in meinem täglichen Leben darstellt und zudem eine der besten - gerade weil stabilsten - Freunde in meinem Leben ist. Sie treibt mich immer wieder durch unglaublich präzise Einschätzungen und wertvolle Kritik ins Gleichgewicht zurück.

...Dirk Böhmer, der mich durch seinen eigenen Enthusiasmus an die Welt der Computer und Problemlösungen herangeführt hat, und so den Grundstein für meine aktuellen Fähigkeiten in der Programmierung und Datenanalyse gesetzt hat.

...meinen Großeltern für die vielen schönen gemeinsamen Stunden, in Berlin und Kallinchen, in kleiner Runde oder mit der ganzen Familie versammelt.

...allen anderen Mitgliedern meiner erstaunlich großen Familie, mit denen ich viele freudige Momente geteilt habe.

...Mario Borgwardt und Tina Günther. Es ist ein Segen, mit jemandem zusammenzuarbeiten, der einen täglich zu Höchstleistungen antreibt. Ich habe das Glück, mit diesem Kollegen auch noch befreundet zu sein. Zusammen mit Tina haben wir schon viel Spaß gehabt und planen noch viele weitere Abenteuer.

...meiner Sport- und Skat-Truppe Lukas Zimmermann, Lorenz Zimmermann, Eric Thum, Söhnke Stöckmann und Julius Seltenheim für die viel zu seltenen Zusammenkünfte fernab jeder Verpflichtung und Verantwortung in vollkommener Gelassenheit.

...Anna Chanbekowa, für die gemeinsam durchgestandenen harten Stunden, Tage und Wochen und für die vielen Erfahrungen und Errungenschaften, die sie meinem Leben hinzugefügt hat. Die mitunter sehr ermüdende Arbeit wurde durch die gemeinsame Zeit regelmäßig aufs Neue entschädigt.

...meiner Tochter, Sophia, dafür, dass du mich innerhalb kürzester Zeit entwaffnen, verblüffen, erheitern, beeindrucken und erzürnen kann. Jeder gemeinsam erlebte Moment mit dir ist ein sehr glücklicher, an den ich mich gerne erinnere.

Selbstständigkeitserklärung

Der Verfasser erklärt, dass er die vorliegende Arbeit selbständig, ohne fremde Hilfe und ohne Benutzung anderer als der angegebenen Hilfsmittel angefertigt hat. Die aus fremden Quellen (einschliesslich elektronischer Quellen) direkt oder indirekt übernommenen Gedanken sind ausnahmslos als solche kenntlich gemacht. Die Arbeit ist in gleicher oder ähnlicher Form oder auszugsweise im Rahmen einer anderen Prüfung noch nicht vorgelegt worden.

Berlin, April 20, 2017